UNIVERSITÀ DEGLI STUDI DI PADOVA

UNIVERSITÀ DEGLI STUDI DI PADOVA

Dipartimento di Scienze Chimiche

Scuola di dottorato di ricerca in Scienze Molecolari,

indirizzo Scienze Chimiche

XVII CICLO

A PULSE EPR INVESTIGATION ON THE STRUCTURE OF PROTEINS AND BIOMIMETIC MODEL COMPOUNDS INVOLVED IN ENERGY CONVERSION

Direttore della Scuola: Ch.mo Prof. Antonino Polimeno

Coordinatore d'indirizzo: Ch.mo Prof. Antonino Polimeno

Supervisore: Dr. Marilena di Valentin

Dottorando: Marco Albertini

Table of Contents

ABSTRACT

In the last decades Electron Paramagnetic Resonance spectroscopy has significantly developed as a versatile tool for the investigation of complex paramagnetic centers. Since then several microwave pulse sequences have been designed in order to disentangle the magnetic interactions between the unpaired electrons and the magnetically active surrounding. Despite their reactivity, paramagnetic centers are quite diffuse in biological systems, where they are usually involved in the key roles of the entire enzymatic activity of proteins. Many enzymes rely on paramagnetic transition metal centers for their catalytic role while different organic and metallic paramagnetic centers are essential in the whole photosynthetic process. In this thesis work advanced Electron Paramagnetic Resonance spectroscopy is exploited to deeply investigate the structure and the surrounding of three different classes of paramagnetic centers, which are present in proteins and artificial biomimetic systems and all being involved, directly or indirectly, in the sunlight energy conversion process that brings energy from the Sun to the Earth. The peptide environment of the active site of a protein is known to play a peculiar role in the fine tuning of the whole activity of the protein, for this reason the investigation of the surrounding of the paramagnetic center turn to be crucial for a correct and comprehensive description of the energy conversion pathway.

The first system here investigated is the reduced iron-sulfur cluster of the HydF protein, an enzyme involved in the correct maturation of the [Fe-Fe]-hydrogenase. Up to date the entire maturation pathway is still unclear, so that a multi-layered description at molecular level of the role of the HydF protein is of fundamental meaning. Then the investigation moves to the triplet state of the carotenoid involved in the photoprotection mechanism inside the Peridinin - Chlorophyll *a* – Protein. In this case a water molecule has been identified as an active and conserved player in the energy transfer process between the pigments. Finally, we have explored the feasibility of employing the photoexcited triplet state of tetraphenylporphyrin as a spin probe for the Double-Electron-Electron-Resonance technique on several artificial biomimetic compounds. The introduction of this novel spin probe approach will considerably improve the structural-investigation potential of this technique since porphyrins are widespread pigments, constituting the molecular core of chlorophylls, bacteriochlorophylls and heme groups. The application to a biological system, the Peridinin - Chlorophyll *a* – Protein antenna complex, has also been tested with very good and promising results.

For all these systems, Electron Paramagnetic Resonance spectroscopy proved to be a valuable and effective tool for investigating the systems hereafter reported, giving new insight into energy conversion and transfer mechanisms in biological systems from a structural point of view, highlighting how the fine tuning of the surrounding of the paramagnetic center at atomic level is crucial for the future design of biomimetic compounds

able to efficiently convert solar energy into practical fuels. In addition the triplet state has been demonstrated to be a valuable spin probe for distance and orientation measurement in both biological and biomimetic systems, opening the possibility to exploit the triplet state as a probe for gaining structural data at molecular level.

THESIS ABSTRACT (ITALIAN)

Nel corso degli ultimi decenni la spettroscopia di risonanza di spin elettronico ha subito un enorme sviluppo come tecnica per lo studio di sistemi paramagnetici complessi. Da allora sono state progettate una serie di differenti sequenze di impulsi di microonde con l'obiettivo di isolare le singole interazioni magnetiche tra l'elettrone spaiato sede del centro paramagnetico e l'intorno magneticamente attivo. Nonostante la loro reattività, i centri paramagnetici ricorrono frequentemente all'interno dei sistemi biologici, dove generalmente svolgono ruoli di primaria importanza nell'attività enzimatica delle proteine. Una gran quantità di enzimi fa affidamento su centri paramagnetici costituiti da ioni di metalli di transizione per il corretto svolgimento dell'attività catalitica mentre centri paramagnetici di tipo sia organico che metallico sono noti costituire parte essenziale dell'intero processo fotosintetico. In questa tesi si farà uso di strumenti avanzati di spettroscopia di risonanza di spin elettronico per uno studio approfondito di tre classi di centri paramagnetici di origine sia biologica che artificiale accomunati dall'essere coinvolti più o meno direttamente in processi di conversione dell'energia solare. È noto come l'intorno proteico del sito attivo di una proteina sia di fondamentale importanza nella regolazione dell'intera attività enzimatica, così che lo studio approfondito dell'intorno proteico proposto in questo lavoro di tesi è fondamentale per una corretta e

completa descrizione dei meccanismi di conversione dell'energia solare.

Il primo sistema presentato è la forma ridotta del cluster ferro-zolfo della proteina HydF, un enzima coinvolto nel processo di maturazione della [Fe-Fe]-idrogenasi. Ad oggi l'intero processo di maturazione presenta ancora punti poco chiari, così che una dettagliata descrizione a livello molecolare del ruolo di HydF risulta di fondamentale importanza. Successivamente verranno esposti i risultati di uno studio sullo stato di tripletto del carotenoide coinvolto nel processo di fotoprotezione attivo nella proteina peridinin - chlorophyll *a* - protein (PCP). In questo caso lo studio ha permesso di identificare il ruolo primario di una molecola d'acqua nel processo di trasferimento di energia di tripletto tra i pigmenti coinvolti. Infine è stata indagata la possibilità di impiegare lo stato di tripletto foto-eccitato della molecola tetrafenilporfirina come potenziale *spin probe* nella tecnica di doppia risonanza *Double-Electron-Electron-Resonance* su di una serie di composti biomimetici. L'introduzione di questo nuovo approccio porta notevoli innovazioni nello studio strutturale basato su tale tecnica poiché le porfirine rappresentano una classe di pigmenti particolarmente diffusa in natura, costituendo la base di clorofille, batterioclorofille e del gruppo eme. Nello stesso capitolo viene presentata l'applicazione della tecnica ad un sistema biologico, la proteina PCP, con risultati promettenti.

La spettroscopia di risonanza paramagnetica elettronica in tutti questi casi si è dimostrata un valido strumento per l'indagine dei sistemi riportati nel lavoro, fornendo

nuovi dettagli strutturali circa i meccanismi di conversione di energia all'interno di sistemi biologici e chiarendo come la struttura a livello atomico dell'intorno del centro paramagnetico sia di fondamentale importanza per la progettazione futura di sistemi biomimetici capaci di convertire efficacemente l'energia solare in combustibile. Infine è stato dimostrato come lo stato di tripletto sia un valido *spin probe* per l'ottenimento di informazioni riguardanti la distanza e l'orientazione all'interno di sistemi biologici e biomimetici, aprendo la possibilità di sfruttare lo stato di tripletto come sonda per ottenere informazioni strutturali a livello molecolare.

ACKNOWLEDGEMENTS

My best thanks go to Dr Marilena Di Valentin who in the role of my supervisor constantly and patiently help me during these three years of doctorate. She possesses the special talent of having a nice word and a smile for every situation and of being always available to share her prolific knowledge with her students.

I also would like to thank Prof Donatella Carbonera for guiding me in the right direction during my first period of doctorate. She perfectly fills the role of leader of our research group, being able of getting control of the situation and promptly solving our mess.

I'm greatly indebted with all of our collaborators who make possible to achieve the results reported in this thesis. Great efforts have been done at the department of biology to prepare an infinite series of mutants of the HydF protein at the right concentration for EPR spectroscopy. I would like to thank Dr Paola Costantini, Dr Paola Berto, Francesca Vallese, Edith De Rosa, Lorenzo Maso and Laura Galazzo.
A special thanks goes also to Prof Antonino Polimeno, Dr Laura Orian and Claudia Tait who spent a lot of time performing calculations on the different PCP antenna complexes investigated in this thesis.
The success of the last work discussed in this thesis was possible only thanks to the great efforts and interest of Prof Marina Gobbo, Prof Antonino Polimeno, Dr Laura Orian, Enrico Zurlo and Mariagiulia dal Farra.

An exclusive thanks goes to all my family to whom this work is dedicated. They supported me during all these eight years away from home making possible to reach these results. I hope this will be the last thesis work you have to bear!

Finally a special thanks goes to the lovely creature that slipped in my life two years ago. She supported me either in the best and in the worst times, always driving me to the right way to continue the work even if this have meant to spent a lot of time away from each other.

For my family.

CHAPTER 1

INTRODUCTION

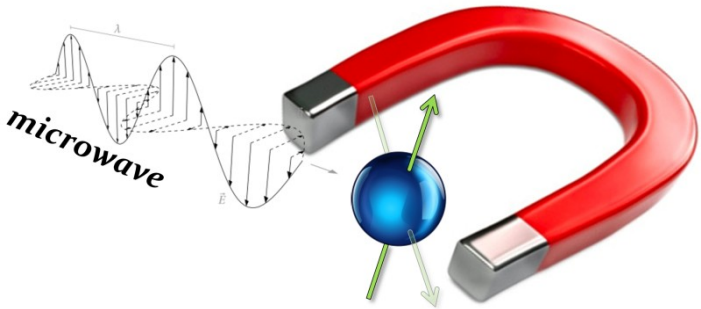

THE SCOPE OF THIS THESIS

This thesis deals with several advanced techniques of pulsed Electron Paramagnetic Resonance (EPR) employed here to investigate the structure of paramagnetic centers in complex systems involved in energy conversion at atomic resolution. Microwave pulses represent a powerful, evolving tools to manipulate magnetization and obtain in-depth description of paramagnetic sites and their surroundings. The coordinative environment of a biological [4Fe4S] cluster has been acutely characterized using a variety of EPR techniques ranging from the classical Continuous Wave to the Electron Spin Echo Envelope Modulation (ESEEM) spectroscopy and to the 2-D Hyperfine Sublevel Correlation (HYSCORE) spectroscopy. A wide site directed mutagenesis and deuterium oxide exchange of the protein buffer have also been necessary to study even more deeply the coordination environment as reported in chapter 3. The intriguing photoexcited variant of pulsed EPR experiment has been extensively employed to explore the proton environment of the triplet state of the carotenoid peridinin in the Peridinin-Chlorophyll *a*-Protein antenna complex (PCP). In this case the comparative study among different PCPs, supported by a Density Functional Theory approach in collaboration with prof. Antonino Polimeno and dott. Laura Orian, reveals a remarkable conservation of the exchangeable proton environment, suggesting a key role of the water network in the entire photoprotective machinery as seen in chapter 4. Finally, collecting the theoretical and experimental experience on the triplet state, the work

moved on the photoexcited triplet state of a tetraphenylporphyrin which has been demonstrated to be a potential spin label for measuring interspin distances and orientations with the Pulsed Electron Double Resonance (PELDOR), technique also known as Double Electron Electron Resonance (DEER). In the last decades the regular approach of DEER spectroscopy proved to be a very valuable tool for investigating the structure and the conformational changes of large biomolecules when lacking the crystal structure. In chapter 5 the results of the new spin label approach are presented showing a great enhancement in the sensitivity of the technique which opens the possibility of a wide employment of the methodology in the biological context. After the application of the technique to a series of model compounds employed to demonstrate the feasibility of the novel experiment, the PCP antenna has been investigated by exploiting the endogenous chlorophyll-a triplet state, gaining structural details of the photoprotective site.

1.1 THE SPIN ANGULAR MOMENTUM

Angular momenta belong to a special group of properties jointly named 'constants of motions' of an isolated system. These constants and their corresponding operators, generally referred to as $\hat{\boldsymbol{J}}$, play a fundamental role in the quantum mechanics of subatomic particles. Electrons possess two types of angular momenta related to the orbital motion and to their spin properties. The orbital angular momentum $\hat{\boldsymbol{L}}$ can be described in classical terms and is associated to the spatial wavefunction of the particle $\psi(\boldsymbol{r})$ while the spin angular momentum $\hat{\boldsymbol{S}}$ has no classical counterpart and it arises from an intrinsic property of the particle named spin.

All the quantum mechanical properties of the generalized angular momentum hold for the spin angular momentum; in particular the commutations properties are the following:

$$\left[\hat{\boldsymbol{S}}^2, \hat{\boldsymbol{S}}_z\right] = 0 \qquad (1.1)$$

$$\left[\hat{\boldsymbol{S}}_i, \hat{\boldsymbol{S}}_k\right]_{\mathrm{i}\neq\mathrm{k}} \neq 0 \qquad (1.2)$$

According to the commutation rules, some implications can be derived from eqq. (1.1 - 1.2), one of the most significant being that only $\hat{\boldsymbol{S}}^2$ and $\hat{\boldsymbol{S}}_i$, the operator related to one of the three Cartesian component of the momentum, can be simultaneously operators of the same electron wavefunction. The corresponding eigenvalues of the two operators, the squared magnitude of the momentum and its projection along the z

direction, are specified by two quantum numbers named s, the primary spin quantum number, and m_s, the secondary spin quantum number as depicted in figure 1.1 according to the following equations

$$\widehat{\boldsymbol{S}}^2|s,m_s\rangle = \hbar^2 s(s+1)|s,m_s\rangle \quad (1.3)$$

$$\widehat{\boldsymbol{S}}_z|s,m_s\rangle = \hbar m_s|s,m_s\rangle \quad (1.4)$$

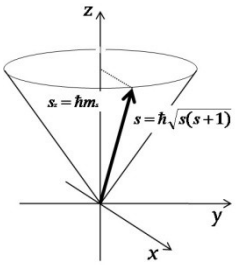

FIGURE 1.1 PICTORIAL REPRESENTATION OF AN ELECTRON SPIN ANGULAR MOMENTUM PLACED IN A HOMOGENEOUS MAGNETIC FIELD ALIGNED ALONG THE *Z* AXIS. THE MODULUS AND THE PROJECTION OF THE VECTOR ALONG THE *Z* AXIS ARE ALSO REPORTED.

In the case of the electron, s has the half-integer value of ½ while the allowed values for m_s range between $-s$ and $+s$ in integer steps, namely -½ and +½.

Due to the electric charge of the electron, a magnetic moment is associated to both the angular momenta. Specifically the orbital magnetic moment of an electron can be derived in analogy with the classical physics of a circulating electric current i in a circle of radius r on the xy plane. In such a system the magnetic moment μ is aligned with the z direction and has a magnitude:

$$\mu_z = \frac{q}{2m} mvr = \frac{q}{2m} l_z \qquad (1.5)$$

where q is the electric charge of the particle, m and v its resting mass and speed respectively.

Shifting to the spin angular momentum and considering that the magnetogyric ratio is defined as $\gamma = g * q/2m$, where g is the Zeeman correction factor and that the Bohr magneton is $\beta = \left|{}^{\gamma\hbar}/_{g}\right|$, we can write a parallel equation for the spin magnetic moment for a free electron:

$$\mu_z = \gamma_e \hbar m_s = -g_e \beta_e m_s \qquad (1.6)$$

The negative sign arises from the negative charge of the electron and implies that the magnetic moment vector lies on an anti-parallel direction compared to the spin angular moment vector.

1.2 THE ZEEMAN EFFECT

Placing a particle characterized by a non-zero spin magnetic moment in an external magnetic field $\boldsymbol{B_o}$ will result in an interaction of the magnetic moment with the field. This interaction is referred as the Zeeman effect [1, 2]. The Hamiltonian operator representing the specific interaction for an electron can be inferred from the classical expression for a magnetic dipole placed in an homogeneous external magnetic field aligned along the z direction :

$$\widehat{\mathcal{H}} = -\boldsymbol{B_0} \cdot \widehat{\boldsymbol{\mu}} = \beta_e \boldsymbol{B_0} \cdot \widetilde{\boldsymbol{g}} \cdot \widehat{\boldsymbol{S}}_z \qquad (1.7)$$

in which the g correction factor has been replaced for a more accurate description by the $\tilde{\boldsymbol{g}}$ tensor, a 3x3 matrix accounting for the anisotropy of the Zeeman interaction. Two spin eigenfunctions describe the spin states of a single electron, *α(e)* and *β(e)*, corresponding to the two allowed values of the secondary spin quantum number m_s, namely +1/2 and -1/2. Applying the previous Hamiltonian to the orthonormal spin eigenfunctions *α(e)* and *β(e)* and neglecting the g anisotropy gives two discrete values of energy:

$$\widehat{\mathcal{H}}|\alpha(e)\rangle = +{}^{1}/_{2}\, g_e \beta_e B_0 |\alpha(e)\rangle \qquad (1.8)$$

$$\widehat{\mathcal{H}}|\beta(e)\rangle = -{}^{1}/_{2}\, g_e \beta_e B_0 |\beta(e)\rangle \qquad (1.9)$$

According to these results the external magnetic field produces an energy separation of the states with different values of spin magnetic moment, *i.e.* of the states labelled with different values of the secondary spin quantum number m_s (see figure 1.2), the so-called Zeeman splitting.

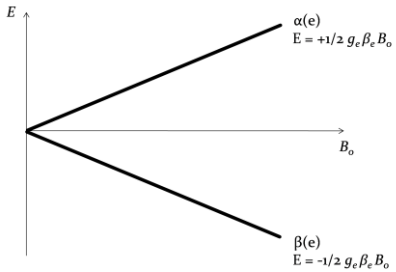

FIGURE 1.2 THE ZEEMAN SPLITTING OF A S=1/2 SYSTEM AS A FUNCTION OF THE EXTERNAL MAGNETIC FIELD B_0.

The Zeeman energy splitting is accompanied by a difference in the population of the two spin states P_α and P_β described by the Boltzmann distribution; in more detail the Boltzmann factor takes the form:

$$P_\beta \Big/ P_\alpha \propto e^{\frac{E_\alpha - E_\beta}{kT}} = e^{\frac{g_e \beta_e B_0}{kT}} \qquad (1.10)$$

in which k is the Boltzmann constant and T is the absolute equilibrium temperature of the system. The integrated transition intensity of an Electron Paramagnetic Resonance (EPR) absorption line is proportional to the excess of population of one of the levels involved in the transition with respect to the other. The small energy separations induced by the external magnetic field is the main cause of a general poor sensitivity of the magnetic spectroscopies, which in EPR is of the order of the tenth of μM of spins being detectable.

During a conventional continuous wave experiment (which will be discussed later in more details) the energy separation between the spin levels is matched by an oscillating external magnetic field $\boldsymbol{B_1}$ fed by a continuous wave polarized electromagnetic (EM) radiation at a proper frequency (usually in the microwave range) in order to match the primary selection rule $h\nu = \Delta E = g_e \beta_e$. The resonant condition and the relative orthogonality of $\boldsymbol{B_0}$ and $\boldsymbol{B_1}$ at the sample position ensure the absorption of energy by the spin system from the EM radiation which is detected as an EPR signal. This absorption phenomenon can be depicted as a spin flipping from a value of m_s to another, according to the

$\Delta m_s = \pm 1$ selection rule in order to guarantee the conservation of the total angular momentum, as the photon brings a unitary spin.

For the sake of completeness, it should be noted that the Zeeman interaction as defined in eq. 1.7 could involve a generic spin magnetic dipole interacting with an external magnetic field. At atomic level electrons are not the only particles having non-zero spin magnetic momentum since several nuclei are characterized by a net nuclear spin angular momentum (*i.e.* a non-zero nuclear spin quantum number *i*). The equations relating the energy of a spin state (eqq. 1.8 and 1.9) to the external field still hold also for the nuclear spin case if g_e and β_e are substituted with their nuclear counterpart g_n and β_n and the spin operator $\hat{\boldsymbol{S}}_{\boldsymbol{z}}$ with $\hat{\boldsymbol{I}}_{\boldsymbol{z}}$, the nuclear spin angular momentum operator. Two considerations can be made regarding the nuclear Zeeman interaction. Primarily, due to the positive charge of the nucleus, the sign of the nuclear magnetogyric ratio γ_n is positive too, but, since g_n can assume both positive and negative values (unlike g_e which is always a positive quantity), the energy order of nuclear spin states is not trivial and should be considered for every different nucleus under investigation. Secondarily, since the nuclear resting mass is about three orders of magnitude larger than that of electron, the energy separation of the spin states is about the same three orders of magnitude less than for the electronic case. This means that to promote nuclear spin transitions in the same external magnetic field a tinier EM energy quantum is needed (usually in the radiofrequency range), avoiding in general the

superposition of both electronic and nuclear Zeeman transitions.

1.3 Zero field interactions in EPR

Besides the Zeeman interaction, there are several other interactions involving electrons and nuclei that do not need an external field to manifest, collectively known as *Zero Field Interactions*. These interactions originates from two different physical phenomena, the classical dipole-dipole coupling of the magnetic momenta of electrons and nuclei and the quantum-mechanical overlap of the wavefunction of electrons and nuclei.

The hyperfine coupling

Hyperfine coupling is the interaction originating from the coupling of the magnetic momentum of the unpaired electron with that of the surrounding nuclei. It is a great source of structural information since it holds a well-defined dependence on the distance and orientations of the interacting dipoles. The Hamiltonian describing the interaction is a quite simple one

$$\hat{\mathcal{H}}_{HF} = \hat{\boldsymbol{S}} \cdot \tilde{\boldsymbol{A}} \cdot \hat{\boldsymbol{I}} \tag{1.11}$$

with the $\tilde{\boldsymbol{A}}$ term representing the 3x3 hyperfine coupling tensor, which holds all the information about the distance and the orientation of the interaction. The $\tilde{\boldsymbol{A}}$ tensor itself is formulated as the sum of two individual contributions: an isotropic component a_{iso}, deriving from the quantum mechanical properties of the electron

wavefunction, and an anisotropic, tensorial component $\widetilde{\boldsymbol{T}}$ describing the classical electron-nuclear dipole-dipole coupling.

The a_{iso} term is also known as the *Fermi Contact* term and it is given by:

$$a_{iso} = \frac{2}{3}\mu_0 g_e \beta_e \beta_n |\psi_0(0)|^2 \qquad (1.12)$$

It can be seen that it is proportional to the probability of finding the unpaired electron at the nucleus position, $|\psi_0(0)|^2$, a feature that only *s-orbital* electrons possess. This type of electrons are the root of the *Fermi contact* interaction and their spherical symmetry ensures the isotropic nature of the interaction. The same interaction is at the basis of the isotropic hyperfine coupling observed in π-type radicals, $CH_3^{\cdot}$ for example, which are characterized of a null probability of finding the electron at the nucleus position since both the carbon and the hydrogen atoms lie on a nodal plane of the π orbital. In this subtle case the π-type unpaired electron induce a polarization on the σ-type electrons bonding the two atoms, causing a net spin polarization at the hydrogen nucleus position, which results in an isotropic hyperfine interaction being observed.

The anisotropic component $\widetilde{\boldsymbol{T}}$ originates from the classical, orientation dependent, coupling of magnetic dipoles, here more specifically the electron spin magnetic dipole, $\boldsymbol{\mu}_e$, with the nuclear spin magnetic dipole, $\boldsymbol{\mu}_n$, of a surrounding nucleus placed at a distance r:

$$E_{dip} = \frac{\mu_0}{4\pi}\left[\frac{\boldsymbol{\mu}_e \cdot \boldsymbol{\mu}_n}{\boldsymbol{r}^3} - \frac{3(\boldsymbol{\mu}_e \cdot \boldsymbol{r})(\boldsymbol{\mu}_n \cdot \boldsymbol{r})}{\boldsymbol{r}^5}\right] \qquad (1.13)$$

Ignoring g_e and g_n anisotropy and substituting the classical magnetic dipoles with their corresponding quantum mechanical expressions, the Hamiltonian describing the anisotropic hyperfine interaction is obtained:

$$\hat{\mathcal{H}}_{dip} = \frac{\mu_0}{4\pi} g_e \beta_e g_n \beta_n \left[\frac{\hat{\boldsymbol{S}}\cdot\hat{\boldsymbol{I}}}{\boldsymbol{r}^3} - \frac{3(\hat{\boldsymbol{S}}\cdot\boldsymbol{r})(\hat{\boldsymbol{I}}\cdot\boldsymbol{r})}{\boldsymbol{r}^5}\right] \qquad (1.14)$$

The orientation dependence of this interaction, which is intrinsic to the dot products between each of the dipoles and the connecting vector $\boldsymbol{r}$ becomes also more explicit if the Hamiltonian is written in its tensor form in the hyperfine principal axis system:

$$\hat{\mathcal{H}}_{dip} = \tilde{\boldsymbol{T}} = \frac{\mu_0}{4\pi\hbar}\frac{g_e\beta_e g_n\beta_n}{\boldsymbol{r}^3}\begin{pmatrix} -1 & & \\ & -1 & \\ & & 2 \end{pmatrix} = \\ = \begin{pmatrix} -T & & \\ & -T & \\ & & 2T \end{pmatrix} \qquad (1.15)$$

in which the distance dependence has been collected in the dipolar T parameter.

The magnitude of the interaction reach its maximum value in the condition in which both the magnetic spins are aligned along the direction of the interspin vector $\boldsymbol{r}$, while the minima are in correspondence of the perpendicular directions. If the point-dipole approximation holds (which is commonly true for$r \geq 0.25$ nm) the distance can be inferred directly from the value of T.

THE EXCHANGE COUPLING

The exchange coupling refers to the interaction of electrons due to the overlap of the spatial wavefunctions

describing the electron orbitals. In this sense the exchange coupling is a completely quantum mechanical phenomenon which has no counterpart in classical mechanics.

The Hamiltonian defining the exchange interaction between two electron spins is the following:

$$\widehat{\mathcal{H}}_{exc} = \widehat{\boldsymbol{S}}_{\boldsymbol{1}} \cdot \tilde{\boldsymbol{J}} \cdot \widehat{\boldsymbol{S}}_{\boldsymbol{2}} \qquad (1.16)$$

in which the exchange coupling is represented by the 3x3 matrix $\tilde{\boldsymbol{J}}$. The most representative part of the $\tilde{\boldsymbol{J}}$ tensor is the isotropic part J_o that can be associated to a first approximation to the exchange integral between the (normalized) spatial wavefunction ϕ_i of the two interacting electrons (1) and (2):

$$J_0 = -2\left\langle \phi_a(1)\phi_b(2)\left| \frac{e^2}{4\pi\varepsilon_0 r} \right| \phi_a(2)\phi_b(1) \right\rangle \quad (1.17)$$

in which e is the electron charge, ε_o is the vacuum permittivity and r is the interspin distance.

The exponential decay dependence of the exchange coupling due to its wavefunction superposition nature means that the interaction is large only if the inter-electron distance is sufficiently small (r < 1.5nm) to allow a significant superposition of the wavefunctions. Thus the interaction is notable when dealing with triplets or higher spin states, which are characterized by exchange interactions generally much larger than the Zeeman splitting and any other magnetic interaction. The same interaction is responsible for the lower limit in PELDOR distance measurements, which is commonly set to 1.5nm. Approaching at shorter distances the exchange interaction between the two paramagnetic centers reach

considerable values, interfering with the pure dipolar component on which this technique relies (see chapter 2).

THE ELECTRON DIPOLAR INTERACTION

Similarly to the anisotropic dipolar component of the hyperfine interaction *T*, a through-space dipolar coupling is observed between a couple of electron spins. A similar Hamiltonian in which the nuclear spin operator is replaced with its electronic counterpart describes the electron dipolar interaction

$$\widehat{\mathcal{H}}_{ss} = \frac{\mu_0}{4\pi} g_1 g_2 \beta_e{}^2 \left[\frac{\hat{\boldsymbol{S}}_1 \cdot \hat{\boldsymbol{S}}_2}{\boldsymbol{r}^3} - \frac{3(\hat{\boldsymbol{S}}_1 \cdot \boldsymbol{r})(\hat{\boldsymbol{S}}_2 \cdot \boldsymbol{r})}{\boldsymbol{r}^5}\right] \qquad (1.18)$$

The Hamiltonian (1.18) can be simplified by some convenient algebra if it is expressed in terms of the total spin operator $\hat{\boldsymbol{S}} = \hat{\boldsymbol{S}}_1 + \hat{\boldsymbol{S}}_2$ and averaged on all the positions of the two electrons, leading to the following effective spin Hamiltonian

$$\widehat{\mathcal{H}}_{ss} = \hat{\boldsymbol{S}} \cdot \tilde{\boldsymbol{D}} \cdot \hat{\boldsymbol{S}} \qquad (1.19)$$

This interaction is of primary interest when dealing with paramagnetic systems in triplet state, characterized by strongly interacting electrons, in this case it is commonly referred to as *Zero Field Splitting*. The electron dipolar interaction is responsible for the splitting of the electronic triplet state into three sublevels even in the absence of an applied magnetic field as discussed later in this thesis.

The same dipolar interaction is pivotal for distance measurement by PELDOR spectroscopy. In this case the interaction concerns two far, weakly coupled

paramagnetic sites and the traceless $\widetilde{\boldsymbol{D}}$ tensor is commonly written in the principal axis frame:

$$\widetilde{\boldsymbol{D}} = \begin{pmatrix} -\omega_{dd} & & \\ & -\omega_{dd} & \\ & & +2\omega_{dd} \end{pmatrix} \qquad (1.20)$$

in which ω_{dd} is referred to as the dipolar interaction frequency, which is related to the inter-spin distance in the point dipole approximation by the following relation:

$$\omega_{dd} = \frac{\mu_0}{4\pi\hbar}\frac{g_1 g_2 {\beta_e}^2}{r^3} \qquad (1.21)$$

where g_1 and g_2 are the electronic g factors of the two interacting electrons.

A more complete treatment of the PELDOR spectroscopy and its application in distance measurements will be given in chapter 2.

1.4 The spin Hamiltonian in a static magnetic field: a summing up

All the interactions described and other minor terms, which have not been reported here for the sake of clarity and that generally do not have a significant weight in the determination of the total energy of the system, may occur simultaneously when dealing with a spin system under EPR investigation. The total spin Hamiltonian including electronic and nuclear magnetic terms and

zero field interactions is reported below while the single contributions are summed up in table 1.1

$$\widehat{\mathcal{H}} = \sum_{j=1}^{m}\{\beta_e \mathbf{B}_0 \cdot \tilde{\mathbf{g}}_j \cdot \hat{\mathbf{S}}_{z,j} + \hat{\mathbf{S}} \cdot \tilde{\mathbf{D}}_j \cdot \hat{\mathbf{S}} + \hat{\mathbf{S}} \cdot \tilde{\mathbf{J}}_j \cdot \hat{\mathbf{S}} + \sum_{i=1}^{n}\left(a_{iso,j}\hat{\mathbf{S}}_j \cdot \hat{\mathbf{I}}_i + \hat{\mathbf{S}}_j \cdot \tilde{\mathbf{T}}_{j,i} \cdot \hat{\mathbf{I}}_i - g_{n,i}\beta_{n,i}\mathbf{B}_0\hat{\mathbf{I}}_{z,i}\right)\} + \quad + \cdots \tag{1.22}$$

in which the summations are over all the *m* electrons and all the *n* coupled nuclear spins.

TABLE 1.1 SUMMARY OF THE MAIN TERMS OF A GENERAL ELECTRON SPIN HAMILTONIAN

Hamiltonian Term	Interaction	Physical Origin
$\boldsymbol{\beta_e B_0 \cdot \tilde{g} \cdot \hat{S}_z}$	Electronic Zeeman	Coupling of the electronic spin magnetic dipole with the external magnetic field
$\boldsymbol{-g_n \beta_n B_0 \hat{I}_z}$	Nuclear Zeeman	Coupling of the nuclear spin magnetic dipole with the external magnetic field
$\boldsymbol{a_{iso}\hat{S} \cdot \hat{I}}$	Fermi Contact	Non-zero electron density at the nucleus
$\boldsymbol{\hat{S} \cdot \tilde{T} \cdot \hat{I}}$	Anisotropic Hyperfine	Coupling of the electronic and nuclear spin magnetic dipoles each other
$\boldsymbol{\hat{S} \cdot \tilde{J} \cdot \hat{S}}$	Electronic Exchange	Overlap of electronic wavefunctions
$\boldsymbol{\hat{S} \cdot \tilde{D} \cdot \hat{S}}$	Electron Dipolar	Dipolar coupling of electron spins

1.5 THE TRIPLET STATE

Although the spin of the electron is invariably ½, the total spin of a paramagnetic species can reach plenty of integer and half-integer values depending on the number of unpaired electrons and the coupling scheme. A molecule in which the total spin of the electrons is one is said to be in a triplet state, due to the spin multiplicity

$2S + 1 = 3$. Apart from the Zeeman interaction, two of the previously described interactions causes the main energy splitting characterizing the triplet state, namely the exchange J_o and the magnetic dipolar $\widetilde{\boldsymbol{D}}$. Precisely a triplet state is distinguished from a biradical based on the much larger exchange coupling compared to the magnetic dipolar interaction so that two unpaired electrons lying on the same molecule give rise to a triplet state while when they are set apart of several Angstroms by a proper spacer and lay in two distinguished moieties the system is described as a biradical. More in detail, the exchange interaction is responsible for the separation of the triplet and singlet states while the anisotropic dipolar interaction removes the degeneracy of the three sublevels constituting the triplet state even if there is no external magnetic field, as summed up in figure 1.3.

The triplet state is defined by three spin wavefunction corresponding to the three allowed projections of the total spin onto the *z*-axis:

$$|T_{+1}\rangle = |\alpha_1\alpha_2\rangle M_s = +1$$

$$|T_0\rangle = {}^{1}\!/_{\sqrt{2}}\,|\alpha_1\beta_2 + \beta_1\alpha_2\rangle\, M_s = 0$$

$$|T_{-1}\rangle = |\beta_1\beta_2\rangle M_s = -1 \quad (1.23)$$

Taking a proper linear combination of these triplet spin wavefunction allows to work much easier in the zero-field case, as this new set of spin wavefunctions is quantized along the principal axis of the dipolar tensor $\widetilde{\boldsymbol{D}}$:

$$|T_x\rangle = {}^{1}\!/_{\sqrt{2}}\,|T_{-1} - T_{+1}\rangle$$

$$|T_y\rangle = {}^{i}/_{\sqrt{2}}\,|T_{-1} + T_{+1}\rangle$$

$$|T_z\rangle = |T_0\rangle \qquad (1.24)$$

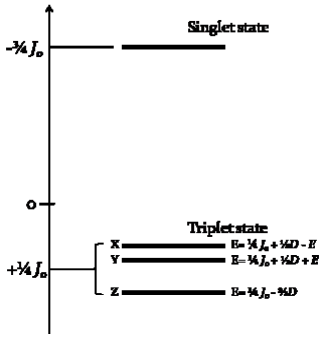

FIGURE 1.3 ENERGY DIAGRAM OF A TWO ELECTRON SYSTEM EXHIBITING EXCHANGE INTERACTION AND MAGNETIC DIPOLAR COUPLING. J_0<0, D>0, E<0.

The eigenvalues of the three states in absence of an external magnetic field, thus taking into account only the magnetic dipolar interaction, are the three diagonal terms of the dipolar tensor, namely D_x, D_y and D_z. Since the $\widetilde{\boldsymbol{D}}$ tensor is traceless, the three energies can be written in terms of only two independent parameters, commonly named D and E (the zero filed splitting parameters) defined as $D = {}^{3}/_{2}\,D_z$ and $E = {}^{1}/_{2}\,(D_x - D_y)$:

$$E_x = {}^{1}/_{3}\,D - E$$

$$E_y = {}^{1}/_{3}\,D + E$$

$$E_z = -\,{}^{2}/_{3}\,D \qquad (1.25)$$

When an external magnetic field $\boldsymbol{B_o}$ is applied, a special direction in space is introduced. In the following a *z*-directed B_o is presented, where *z* refers to the dipolar tensor axis system; the other two options in which the external magnetic field is aligned with the *x* and *y* axis can be readily derived by permutation of the formulæ. With the external magnetic field aligned along the z direction, $|T_z\rangle$ is still an eigenstate, while $|T_x\rangle$ and $|T_y\rangle$ are mixed together according to a mixing angle ϑ defined as $\vartheta = {}^1/_2 \tan^{-1}\left[\left(E_x - E_y\right)/2g\beta_e B_0\right]$:

$$|\sigma_x\rangle = \cos\vartheta|T_{+1}\rangle - \sin\vartheta|T_{-1}\rangle$$

$$|\sigma_y\rangle = \sin\vartheta|T_{+1}\rangle + \cos\vartheta|T_{-1}\rangle$$

$$|\sigma_z\rangle = |T_z\rangle = |T_0\rangle \qquad (1.26)$$

It should be noted that in the limit of very low magnetic field $\vartheta \to \pi/2$ and the $|\sigma_i\rangle$ eigenfunctions approach smoothly to the $|T_i\rangle$, while on the other hand on strong fields spin becomes totally quantized by the magnetic field and the eigenfunctions move toward the $|T_{+1}\rangle$, $|T_0\rangle$ and $|T_{-1}\rangle$ set (as $\vartheta \to 0$) as reported in figure 1.4.

Applying the Hamiltonian accounting for the Zeeman and dipolar interaction to the eigenstates (1.26) results in the energy of the three triplet sublevels being solved:

$$E_x = {}^1/_2\left(E_x + E_y\right) + {}^1/_2\left(E_x - E_y\right)\tan\vartheta + \\ + g\beta_e B_0$$

$$E_y = {}^1/_2\left(E_x + E_y\right) - {}^1/_2\left(E_x - E_y\right)\tan\vartheta - \\ - g\beta_e B_0$$

$$E_z = -{}^2/_3\, D \qquad (1.27)$$

Eigenstates and corresponding energies can readily be obtained when the external magnetic field is aligned along the *x* and *y* directions considering the same procedure illustrated above. The dependence of the energy levels on the strength of the external magnetic field is depicted in figure 1.4.

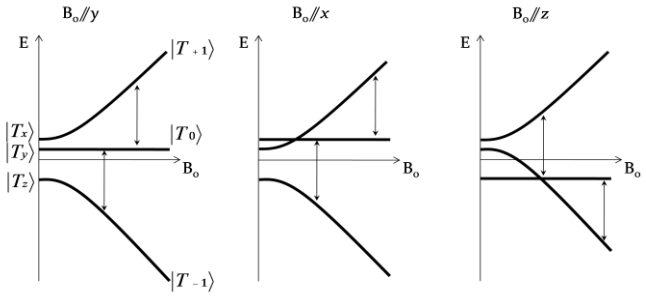

FIGURE 1.4 TRIPLET ENERGY LEVELS OF A SYSTEM CHARACTERIZED BY $D>0$ AND $E<0$ (FOR EXAMPLE TETRAPHENYLPORPHYRIN). TRANSITIONS LABELED BY ARROWS CORRESPOND TO "$\Delta M_S=\pm 1$" OBSERVED TRANSITIONS IN EPR.

Usually molecules possess a singlet electronic ground state: electronic levels are well separated in energy and electrons pair together with opposite spins according to the Pauli's exclusion principle. If one of these electrons is excited to a higher electronic level usually the system still continues to be in a singlet state since any change of the spin is forbidden during an electronic transition and the electronic state is labeled as S_1. But in presence of a spin-orbit coupling this spin selection rule is no longer so strictly valid and an *intersystem crossing* process to a metastable, but long-lived, triplet state can take place. This is the case for example of porphyrin, chlorophyll, fullerene and many aromatic hydrocarbons under strong

photoexcitation. The intersystem crossing process is characterized by a high anisotropy of the rate of population of the three spin sublevels T_X, T_Y and T_Z which leads to a spin polarization of the sublevels (see fig. 1.5). The reason of this effect is the anisotropy of the spin-orbit coupling itself which reflects in the matrix elements $\langle S_1|\widehat{\mathcal{H}}_{so}|T_X\rangle$, $\langle S_1|\widehat{\mathcal{H}}_{so}|T_Y\rangle$ and $\langle S_1|\widehat{\mathcal{H}}_{so}|T_Z\rangle$ being different one from the other.

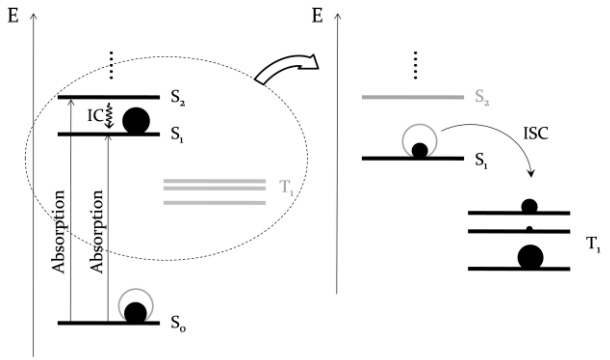

FIGURE 1.5 SCHEMATIC REPRESENTATION OF ENERGY LEVELS AND TRANSITIONS INVOLVED IN THE ANISOTROPIC POPULATION OF A TRIPLET STATE VIA INTERSYSTEM CROSSING (ISC) FROM AN EXCITED SINGLET STATE. IC STANDS FOR INTERNAL CONVERSION. BLACK DOTS REPRESENT THE RELATIVE POPULATION OF THE ELECTRONIC STATES (NOT IN SCALE).

Several other population paths for triplet states are possible over the intersystem crossing. Among these the *triplet-triplet energy transfer* (TTET) is of particular interest, especially when dealing with photosynthetic machinery where it is at the basis of the photoprotective mechanism [3]. In this case triplet state population is transferred from one molecule to another in close proximity (almost in Van der Waals contact [4]) via a

double electron transfer process in a total spin conservation frame[5, 6]. Also this mechanism leads to a spin polarized final triplet state and the spin polarization now holds information about the relative geometry of the two partners involved in the TTET. The population of the *i*-esim acceptor sublevel (*i*=x, y, z) is actually calculated even in presence of an external magnetic field as a sort of projection of the donor population vector P^D from the donor onto the acceptor ZFS axis frame as explicated by the formula [7-9]:

$$P_i^A \propto \sum_k \cos^2 \vartheta_{ik} \cdot P_k^D \qquad (1.28)$$

ϑ_{ik} representing the angle between the *i*- and *k*-esim ZFS axis of the TTET acceptor and donor respectively (*j*, *k* = X, Y, Z).

From equation (1.28) it appears that the correct determination of the ZFS axis frame with respect of the molecular frame is essential for the interpretation of spectral parameters in triplet state EPR when TTET process takes place, as is the case of the above cited photoprotective machineries. In chapter 4, dedicated to the investigation of the photoprotective site of the antenna complex from a marine dinoflagellate organism, more details will be presented regarding the orientation of ZFS axis system with respect to the molecular frame of chlorophyll and carotenoid molecules.

1.6 The classical continuous wave EPR experiment

In a classical continuous wave (CW) EPR experiment the energy separation between the spin states (see fig. 1.2) due to the Zeeman splitting and all the other interactions previously described is varied by sweeping the external magnetic field B_0.The matching of the energy separation by an electromagnetic (EM) monochromatic radiation results in the resonant absorption of energy which is detected as an EPR signal. The external magnetic field $\boldsymbol{B_0}$ is usually supplied by an electromagnet which can range from zero to about 1.7 T. For stronger magnetic fields, superconducting magnets are required. The CW-EM radiation is fed at a fixed frequency (9.5 GHz *approx.*, X-Band) and relatively low power (mW range) by a Gunn diode electronic oscillator inserted into the microwave bridge. The choice of the spectrometer operating frequency (and consequently of the external magnetic field strength) depends on several factors, first of all a better signal to noise ratio (S/N) at low frequencies, which is a consequence of the inverse scaling of the resonator and sample dimensions with the frequency [10]. Another factor is the reduction of the electronic components and cavity dimensions on going at higher frequencies which means higher costs and smaller sample volumes. These and other factors drive the choice of microwave sources in the 9.5 GHz range for the most common commercial spectrometers, which correspond to a convenient centimeter range for the

cavity and waveguide dimensions and to a 340 mT magnetic field (g = 2).

The microwaves travel from the source along a hollow metal waveguide and reach the sample inserted into the resonator whose impedance is coupled to that of the waveguide by a tunable iris. The resonator is built to properly accommodate the low-power EM radiation from the waveguide and store a considerable energy as a standing wave at the fundamental resonant frequency. EPR resonators are also designed to minimize the amplitude of the electric field $\boldsymbol{E_1}$and consequently maximize $\boldsymbol{B_1}$ at the sample position in order to minimize dielectric losses due to the absorption of the electric portion of the EM radiation which usually excites rotational energy levels of the molecules instead of spin transitions. A key requirement for the magnetic field $\boldsymbol{B_1}$ to be absorbed by the spin system is the orthogonality between $\boldsymbol{B_0}$ and $\boldsymbol{B_1}$ which is guaranteed during the design stage. A picture of the two most common resonators employed in EPR spectrometers and their corresponding contour lines of electric and magnetic fields are represented in figure 1.6.

EPR spectrometers commonly work in reflection rather than transmission mode, that is the signal from the resonator uses the same waveguide used to send microwave into the resonator itself. The reflected wave is properly routed to the detection system by a circulator, which is a passive, non-reciprocal device capable of directing entering microwaves from one port into the next in a one-way rotation. The detection is usually performed by a rectifier Schottky diode kept in

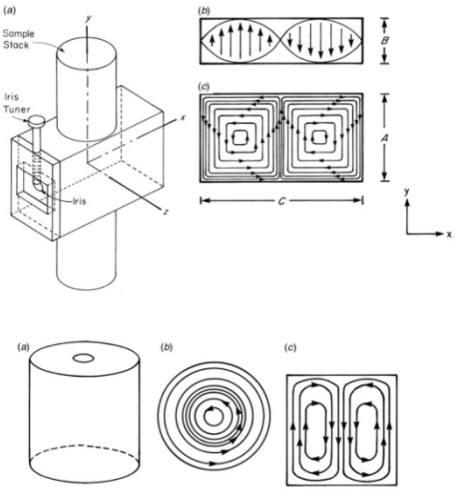

FIGURE 1.6 SCHEMATIC REPRESENTATION OF TWO RESONATORS (A) AND THE CORRESPONDING ELECTRIC (B) AND MAGNETIC (C) FIELD CONTOURS. TOP PANEL: A RECTANGULAR PARALLELEPIPED TE_{102} RESONATOR. BOTTOM PANEL: A CYLINDRICAL TE_{011} RESONATOR. FIGURE TAKEN FROM [11].

its linear regime (100-300 μA) by an appropriate bias current.

Low-frequencies noise reduction is achieved by a special kind of detection called *phase-sensitive detection* which pairs the fast modulation of the external magnetic field B_0 with the *lock-in* amplified detection, resulting in a low noise first derivative of the absorption EPR signal. The modulation is realized usually at 100 kHz at the small amplitude of few Gauss by specific modulation coils (as a rule of thumb modulation amplitude should be less than 1/10 of the full width at half maximum of the most narrow spectral line to avoid distortion in the lineshape). The current intensity of the output signal detected by the diode is then proportional to the slope of the

absorption, resulting in the first derivative lineshape. The noise reduction is obtained by selectively amplifying only the rectified 100 kHz signal and rejecting all the other frequencies through a *lock-in* amplifier.

A detailed scheme of the components of a commercial CW-EPR spectrometer is presented in figure 1.7

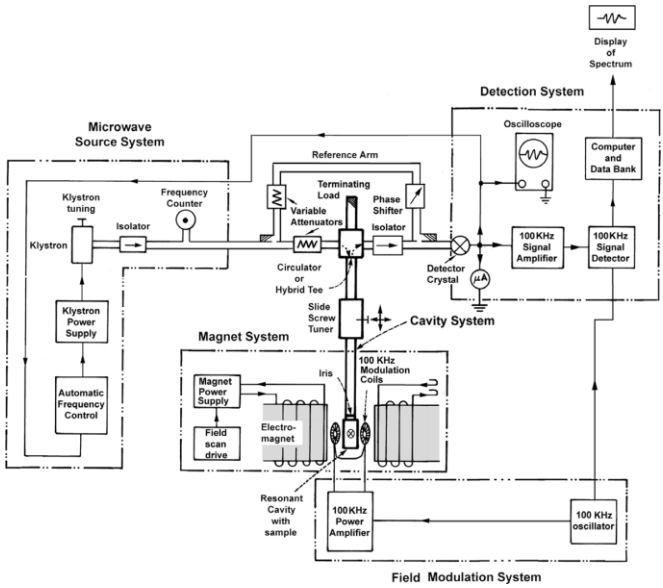

Figure 1.7 Schematic representation of a CW-EPR spectrometer. Figure taken from [11].

CHAPTER 2

PULSE EPR TOOLS FOR STRUCTURE INVESTIGATION

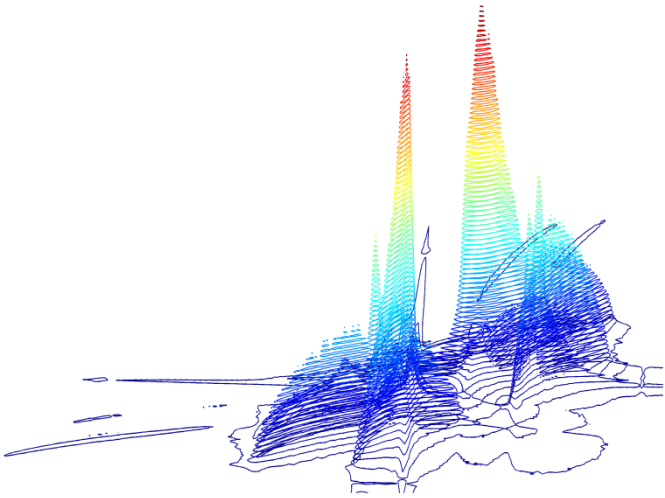

In the previous chapter it was stated that electrons possess an intrinsic angular momentum as a consequence of the quantum mechanical property named spin. When dealing with a real EPR experiment as in this chapter, an ensemble of spin of the order of the Avogadro's number has to be taken into account so that a classical vector representation can be easily applied. This model describes the evolution of a macroscopic magnetization under the application of static and time-dependent magnetic fields and relaxation phenomena in a classical way. A simple but effective description of the main pulse EPR experiment is achieved using the vector model, while for a deeper comprehension a quantum mechanical description via the density operator formalism (which will not be treated here) is essential (see ref. [12] for a complete and detailed description of theory and application of pulse EPR).

2.1 THE VECTOR MODEL

Considering an ensemble of spin-½ particles in a static magnetic field $\boldsymbol{B_0}$, the z-component of the spin magnetic moment is well-defined for every spin, being +1/2 or -1/2 ħ units, while the x and y components are random and quantum mechanically inaccessible. Summing up all the single magnetic moment vectors results in the xy component to vanish and a macroscopic magnetization $\boldsymbol{M_0}$ parallel to the external magnetic field to raise up because of the small excess of m_s -1/2 population as depicted in figure 2.1 (for an electron the spin magnetic

moment lies anti-parallel to the corresponding spin vector, eq. (1.6)).

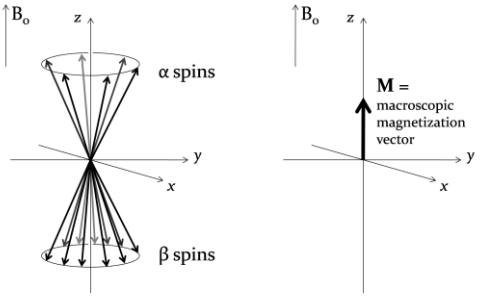

FIGURE 2.1VECTORS REPRESENTING THE INDIVIDUAL SPINS OF AN ENSEMBLE OF ELECTRONS IN AN EXTERNAL MAGNETIC FIELD B_0 (LEFT PANEL), AND THE CORRESPONDING MACROSCOPIC MAGNETIZATION VECTOR (RIGHT PANEL).

In this representation every individual spin precesses about the external magnetic field at an angular frequency termed *Larmor precession frequency* ω_L due to the spin vector tilt from the external magnetic field direction (see fig. 1.1):

$$\omega_L = {}^{g_e\beta_e}/_{\hbar} B_0 \qquad (2.1)$$

It results that the same vector model can be described in two ways: considering a static (lab) frame with a rotating spins or, on the other way, considering a frame rotating at the Larmor frequency in which the specific precessing spins appear as static vectors. The most useful frame for describing the effects of the $\boldsymbol{B_1}$ pulses on the magnetization is the frame rotating at the convenient frequency dictated by the pulse frequency but in some specific cases some other rotating frequencies might be chosen.

The $\boldsymbol{B_1}$ pulses consist usually of short, intense burst of microwave centred at a specific frequency ω_P, while the polarization is linear and perpendicular to the *z*-direction. As depicted in figure 2.2, this polarization can be decomposed as sum of a left and a right circularly polarized $\boldsymbol{B_1}$ fields in the lab frame. In the rotating frame the two circular components result in a fixed component (generally chosen parallel to the *x*-direction) and a counter-rotating component which is largely out of resonance and it is generally neglected.

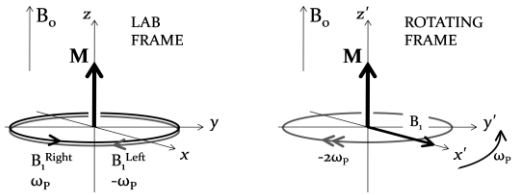

FIGURE 2.2LINEARLY POLARIZED B_1 FIELD AS A SUM OF TWO COUNTER-ROTATING CIRCULARLY POLARIZED FIELDS. THE LAB FRAME (LEFT) AND THE ROTATING FRAME (RIGHT) REPRESENTATIONS.

According to the rotating frame description, as long as the pulse is applied, the magnetization vector $\boldsymbol{M}$ precesses about $\boldsymbol{B_1}$ with a frequency ω_1 (also known as pulse strength) as described by the following Bloch equations:

$$M_x = 0$$

$$M_y = -M_0 \sin(\omega_1 t_p)$$

$$M_z = M_0 \cos(\omega_1 t_p) \qquad (2.2)$$

in which t_p is the pulse length. $\omega_1 t_p$ is collectively represented by β and it is called the *flip angle* because it corresponds to the angle covered by the precessing magnetization $\boldsymbol{M}$ about the B_1 field.

Relaxation phenomena in pulse EPR

Intervals between two subsequent pulses are identified as *free evolution periods*. During these time intervals, usually referred to as τ or T, relaxation phenomena take place in order to restore the equilibrium magnetization. After a pulse the system undergoes a transformation which brings the magnetization out of thermal equilibrium, the latter characterized by the complete alignment of the magnetization $\boldsymbol{M_o}$ along the z-direction. Thinking about a $\pi/2$ pulse (a pulse whose flip angle β is 90°), the net effect on the magnetization is to turn it on the xy plane, precisely to align it along the -y direction of the rotating frame (see eq. (2.2)), which corresponds clearly to an out-of-equilibrium situation. Two distinct relaxation phenomena occur at this point, a *longitudinal relaxation* and a *transverse relaxation* as depicted in figure 2.3.

The longitudinal relaxation tends to restore the z component of $\boldsymbol{M_o}$; the energy required to change the m_s number is provided by transient fluctuating magnetic fields which are in turn induced by lattice vibrations and molecular motions. The longitudinal relaxation involves energy flows between the spin system and the surrounding and it is also usually referred to as *spin-lattice* relaxation and its characteristic time is defined as T_1.

The transverse relaxation cancels out the *xy* component of ***M***, promoting the loss of phase coherence of the single spins after the pulse so that they begin to randomly set apart one from another. It is an adiabatic process whose energy flows are confined between one spin to another in a *flip-flop* process. For this reason the transverse relaxation is frequently labeled as *spin-spin* relaxation and its characteristic time is defined as T_2.

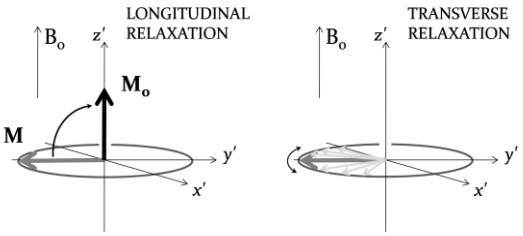

FIGURE 2.3 EFFECTS OF THE TWO MAIN RELAXATION PROCESSES OPERATING ON A SPIN SYSTEM AFTER A $\pi/2$ PULSE HAS BEEN APPLIED IN ORDER TO TURN THE MACROSCOPIC MAGNETIZATION ***M*** TO THE $-Y$ DIRECTION.

Both relaxation processes are extremely significant when dealing with pulse EPR. For example spin-spin relaxation (which occurs in a faster time-scale than spin-lattice relaxation) does not allow to employ the pulse sequences as for the NMR experiment, which are based on the *free induction decay* (FID) detection. In the EPR case the FID signal relaxes so fast that it cannot be detected due to the instrumental dead time of few hundreds of nanoseconds.

2.2 The Field Swept Electron Spin Echo experiment

As mentioned before the fast relaxation prevents FID detection which instead is usually employed in NMR pulse sequences. To overcome this limitation, an echo sequence is regularly employed in which the FID signal generated by a $\pi/2$ pulse is refocused by a π pulse after a free evolution period τ, allowing the detection of a spin echo at a same time τ after the π pulse. The detailed pulse scheme is represented in figure 2.4. The first $\pi/2$ pulse along the *x*-direction has the effect of turning the resting magnetization $\boldsymbol{M_o}$ on the –*y* axis. At this point a free evolution period τ starts during which the two relaxation phenomena previously described take place. More in detail, the longitudinal relaxation slowly reduces the plane component of the magnetization in favor of the (undetectable) *z* component while the transverse relaxation induce the spread of the individual spins far apart, further reducing the in-plane component of $\boldsymbol{M}$. It should be noted that the fanning of the spins in the *xy* plane is also induced by the slight differences in the precession frequencies of the spins which in turn are produced by small dissimilarities in the spin surrounding. After time τ a π pulse is sent to the sample whose effect is to turn all the magnetization vectors by 180° about the *x* axis without changing their rotation directions. This means that after a second time τ all the magnetization vectors, which have been spread out by the frequency differences will be again aligned along the *y* axis. Note that the plane component of the

magnetization, which has been lost due to relaxation phenomena, is not refocused by the π pulse. The detection system is designed to measure the *x* (imaginary) and *y* (real) component of the magnetization ***M*** simultaneously; the refocused magnetization vectors along the *y* axis is called *electron spin echo* or *Hahn echo* from Erwin Hahn, the father of the spin echo.

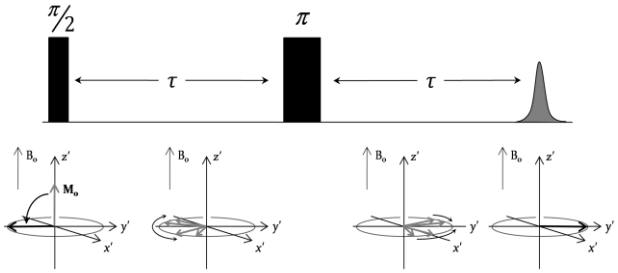

FIGURE 2.4 PULSE SEQUENCE AND DIAGRAMS DESCRIBING THE MOTION OF THE MAGNETIZATION VECTORS IN A HAHN ECHO EXPERIMENT.

The field swept electron spin echo (FSESE) experiment consists in monitoring the echo intensity (*i.e.* the integral over the entire echo) while the external magnetic field is swept across the entire EPR spectrum. The result is an absorption EPR spectrum which is free from lineshape distortions due to the field modulation generally employed in CW-EPR. On the other hand the FS-ESE spectrum may be distorted by some orientation-, B_0- and τ- dependent phenomena, such as nuclear effects or anisotropic relaxations. For this reason a reliable EPR lineshape is obtained by the FS-ESE technique only if several experiments at different values of the τ interval are recorded and summed up, especially

when the paramagnetic site is surrounded by ^{14}N or ^{2}H nuclei which, as will be discussed later, can introduce spectral distortions in the FS-ESE spectrum. In these cases a comparison of the FS-ESE with the classical CW-EPR is recommended.

2.3 THE ESEEM EXPERIMENT

The spin echo generated by a two pulse sequence decays as the τ value is incremented, mainly because of the non-refocusable transverse relaxation process which destroys the spin coherence in the *xy* plane. As observed for the first time by Rowan, Hahn and Mims in 1965 the echo decay is modulated by the presence of magnetically active nuclei in the paramagnetic surrounding as the τ delay is varied [13]. This effect is called *electron spin echo envelope modulation* and represents a significant source of structural information about the primary coordination sphere of the paramagnetic center and beyond.

A qualitative explanation of the 2-pulse ESEEM effect can be provided considering the interaction between an electron spin and a nuclear spin I = ½ as reported in figure 2.5. Two magnetic fields, $\boldsymbol{B_{IS}}$ (the field generated by the nucleus in correspondence of the electron spin) and $\boldsymbol{B_{SI}}$ (the field generated by the electron in correspondence of the nuclear spin), are induced by the two magnetic momenta and summed to the external magnetic field $\boldsymbol{B_o}$. Thus the electron experiences an effective magnetic field $\boldsymbol{B_S} = \boldsymbol{B_o} + \boldsymbol{B_{IS}}$ and correspondingly the magnetic field acting on the nucleus

is $\boldsymbol{B_I = B_o + B_{SI}}$. Since electron spin angular momentum is about three orders of magnitude larger than the nuclear one, $\boldsymbol{B_{SI}}$ (which can be estimated in several hundreds of Gauss at a distance of some angstroms) is the same three orders of magnitude larger than $\boldsymbol{B_{IS}}$ which thus it turns to be almost negligible. As a consequence the quantization axis for the electron spin practically coincides with $\boldsymbol{B_o}$, whereas the nuclear spin quantization axis may differ appreciably from $\boldsymbol{B_o}$ as depicted in figure 2.5, left panel.

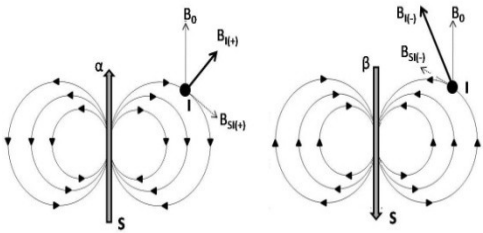

FIGURE 2.5 EFFECTIVE MAGNETIC FIELD $\boldsymbol{B_I}$ ACTING ON A NUCLEUS (REPRESENTED BY A BOLD BLACK DOT) BEFORE (LEFT) AND AFTER (RIGHT) THE INVERSION OF THE ELECTRON SPIN MAGNETIC MOMENT. THE SUDDEN CHANGE IN THE QUANTIZATION AXIS OF THE NUCLEAR SPIN IS RESPONSIBLE FOR THE ESEEM EFFECT.

When the π microwave pulse is applied to the system (provided that the pulse length is short compared to the Larmor precession period of the nucleus) the effect is a sudden change of the secondary spin quantum number of the electron with the main consequence of inverting the relative magnetic field $\boldsymbol{B_{SI}}$. The spin magnetic momentum of the nucleus has no time to adiabatically follow the rapid change of the effective magnetic field and immediately starts to precess about the new field $\boldsymbol{B_I}$ inducing small variations in the local field experienced

by the electron (see figure 2.5, right panel). This periodical variation of the local field experienced by the electron spin is at the basis of the incomplete rephasing of the spin packets that leads to the periodical modulation of the echo intensity observed in an ESEEM experiment. The structure information comes from the modulating frequencies due to the nuclear and hyperfine interaction Hamiltonian of the surrounding nuclei.

The two-pulse scheme described by Rowan, Hahn and Mims is essentially a Hahn echo sequence performed at a fixed external magnetic field in which the τ delay is varied. The corresponding echo modulation function $V_{2p}(\tau)$ is the following:

$$V_{2p}(\tau) = 1 - {}^{k}/_{4}\left[2 - 2\cos(\omega_{\alpha}\tau) - 2\cos(\omega_{\beta}\tau) - \right.$$
$$\left. - \cos(\omega_{-}\tau) + \cos(\omega_{+}\tau)\right] \qquad (2.3)$$

in which k is the modulation depth parameter which is proportional to the product of the allowed and forbidden transition probabilities, ω_{α} and ω_{β} are the nuclear frequencies in the α and β electron spin manifolds and ω_{+} and ω_{-} are their sum and difference combinations. The main drawbacks of this technique are the quick decay of the echo intensity which mainly depends on the T_2 characteristic time and the presence of sum and difference combination frequencies $\omega_{\alpha} \pm \omega_{\beta}$. Both these disadvantages are overcame by introducing the 3-pulse ESEEM scheme depicted in figure 2.6, which relies on the 3-pulse stimulated echo sequence with a fixed τ value and a variable T delay [14]. As it can be stated from the modulation function (eq. 2.4), this technique is free from the combination frequencies, thus

providing simpler spectra. The echo modulation function is the following:

$$V_{3p}(\tau,T) = 1 - {}^{k}/_{4}\{[1-\cos(\omega_\beta\tau)]\cdot[1-\cos(\omega_\alpha(T+\tau))] + \\ + [1-\cos(\omega_\alpha\tau)]\cdot\left[1-\cos\left(\omega_\beta(T+\tau)\right)\right]\} \qquad (2.4)$$

Moreover, the magnetization vector is stored along the z axis during the incrementing period T, removing the T_2 dependence of the echo decay in favor of the slower T_1 dependence. The dependence of the oscillation amplitude on the chosen τ delay results in blind spots occurring at certain τ values depending on the nuclear frequencies themselves, a drawback which is get over by performing several experiments at different τ values and adding them up, as in the previous case of FS-ESE experiment.

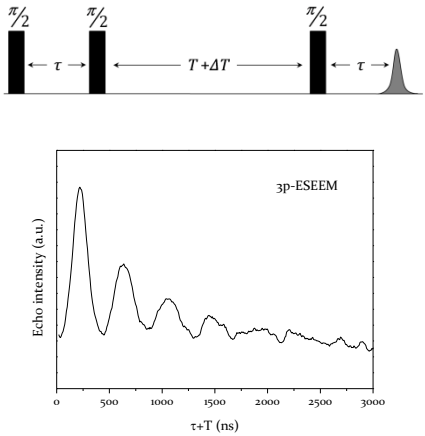

FIGURE 2.6(TOP)3P-ESEEM SEQUENCE (ΔT IS THE INCREMENTAL STEP OF THE T DELAY). (BOTTOM) EXAMPLE OF AN EXPERIMENTAL 3P-ESEEM IN WHICH THE STRONG MODULATIONS ARE DUE TO DEUTERIUM NUCLEI COUPLED TO THE PARAMAGNETIC CENTER.

The structural information that can be obtained from the ESEEM experiment derives from small hyperfine interactions between the paramagnetic centre and the surrounding nuclei. Exact simulation of the ESEEM traces and of the corresponding frequency domain spectra obtained via Fourier transformation allows to gain the value of both the isotropic and the dipolar components of the hyperfine tensor in an orientation selection regime. From the complete hyperfine tensor, distance and orientation of the surrounding nuclei can be achieved.

For a more exhaustive and detailed description of ESEEM theory and its applications see ref. [15-17].

2.4 The HYSCORE EXPERIMENT

The pulse sequence for the *hyperfine sublevel correlation spectroscopy* (HYSCORE) is basically a 3-pulse ESEEM in addition to an hard and unselective mixing π pulse, between the second and the third $\pi/2$ pulses as depicted in figure 2.7. The effect of this pulse is to suddenly reverse the populations of the electronic spin manifolds from α to β and vice versa. In this way nuclear coherences that are evolving in one of the two spin manifolds during the t_1 period due to the ESEEM effect are turned into the other manifold and continue to evolve with a frequency that is now characteristic of this second manifold during the interval t_2. Time intervals t_1 and t_2 are varied independently, giving rise to a two-dimensional interference map which is analyzed by

means of Fourier transform. The result is a 2-D frequency domain spectrum in which peaks are found at (ω_α, ω_β) and (ω_β, ω_α) if the condition $|A| < 2|\omega_I|$ holds ("weak coupling" regime) or at the frequency coordinates (ω_α, $-\omega_\beta$) and ($-\omega_\alpha$, ω_β) if the condition $|A| > 2|\omega_I|$is instead satisfied, (the "strong coupling" regime). This is an additional source of information and reduces the spectral overlapping, setting apart nuclei characterized by different coupling regimes.

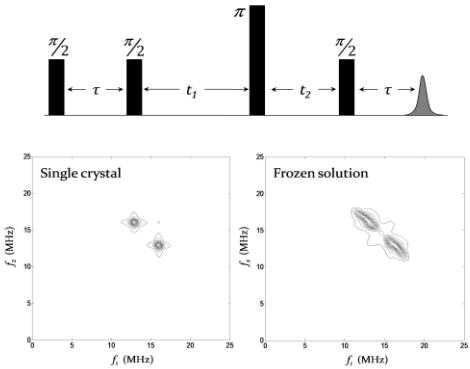

FIGURE 2.7 (TOP) PULSE SEQUENCE FOR THE HYSCORE EXPERIMENT. (BOTTOM) HYSCORE SPECTRA CALCULATED FOR A SINGLE PROTON IN THE WEAK COUPLING REGIME IN SINGLE CRYSTAL (LEFT PANEL) AND IN FROZEN SOLUTION (RIGHT PANEL). CALCULATION WAS DONE USING THE EASYSPIN PACKAGE [18].

HYSCORE spectroscopy is very useful when dealing with complex systems characterized by several coupled nuclei because peaks of nuclei with different hyperfine interaction are usually well set apart. Moreover when the sample is a frozen solution, as in most cases and also in the specific ones described in this thesis, the HYSCORE signals are no longer sharp peaks but become elongated and curled ridges because several relative orientations between the molecule and the external magnetic field

are represented at the same time. From the displacement and the curl of the ridge both the isotropic and dipolar hyperfine components can be graphically inferred [19] as a good starting point for the computer simulation of the spectrum.

2.5 THE DEER EXPERIMENT

The *Double electron-electron resonance* (DEER) spectroscopy, also known as *Pulse electron double resonance* (PELDOR), has been widely employed in the last decade, becoming one of the most exploited EPR technique for structure investigation especially in biomolecules. Firstly introduced in 1959 by Bowers and Mims [20] and latterly developed by Milov and co-workers [21, 22], DEER is a two-frequency pulse EPR technique which consists in monitoring the refocused spin-echo of a set of electron spins while a second set is excited at a different microwave frequency. In this way the electron-electron dipolar and spin exchange interactions taken together are separated from all the other spin interactions.

The most common pulse sequence is the so-called four-pulse DEER which consists of a Hahn echo sequence refocused by a π pulse characterized by fixed time intervals (the *observer sequence*) and an hard π pulse centered at a different microwave frequency (the *pump pulse*) which is swept between the two observer π pulses, as illustrated in figure 2.8. In the simplest case of negligible exchange interaction (interspin distance >1.5 nm, see section 1.3), the effect of the pump pulse is to

invert the state from α to β and vice versa of a set of electron spins, which in turns affect the precession frequency of the coupled observer spins by a term ω_{dd} (exactly the dipolar coupling between the two set of spins, see chapter 1). The non-refocusable phase delay gained by the observer spins affects the final echo intensity and it is proportional to the time interval between the Hahn echo and the pump pulse *t* according to the relation $\phi = \omega_{dd} \cdot t$. The refocused echo amplitude *V(t)* is the following:

$$V(t) = \prod_i \{1 - \lambda_i [1 - \cos(\omega_{dd} t)]\} \qquad (2.5)$$

in which λ_i is the fraction of spins effectively inverted by the pump pulses ($\lambda \approx 0.5$ for a nitroxide spin inverted by a 12 ns pulse at X-band frequency) and the product runs over all the spins coupled to the observer.

Equation (2.5) does not take into account the presence of a background function due to the interaction of pairs of spins not on the same molecule. The complete modulation formula can be factorized as follows

$$V(t) = F(t)B(t) \qquad (2.6)$$

where *F(t)* is the *form factor* which accounts for the intramolecular electron-electron dipolar interactions, usually the strongest and most attractive interactions, while *B(t)* is the *intermolecular background factor* which considers all the long-range intermolecular electron-electron dipolar interactions. While the function *F(t)* is known, the background factor *B(t)*, which depends on several experimental parameters in a non-trivial way, requires an appropriate choice of the background model

in order to finally extract a correct form factor *F(t)* from the experimental data *V(t)*.

The DEER time trace appears as a modulation of the refocused echo intensity as represented in figure 2.8. From equation (2.5) it follows that the modulation frequency corresponds to the dipolar coupling between the two interacting spins, when the exchange interaction is negligible (which is generally true for spin separation larger than 1.5 nm).

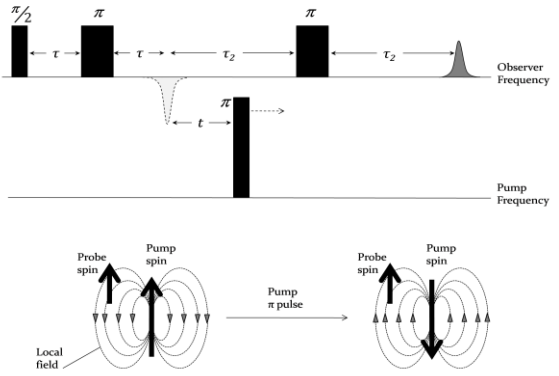

FIGURE 2.8 (TOP PANEL) FOUR-PULSES DEER SEQUENCE. THE PUMP $\boldsymbol{\pi}$ PULSE IS SWEPT BETWEEN THE TWO OBSERVER $\boldsymbol{\pi}$ PULSES. (BOTTOM PANEL) EFFECT OF SUDDENLY CHANGE THE PUMP SPIN STATE. THE LOCAL FIELD INDUCED BY PUMP SPIN ON THE OBSERVER IS IMMEDIATELY CHANGED TOO, INDUCING A SLIGHT CHANGE IN THE PRECESSION FREQUENCY OF THE OBSERVER.

A Fourier transform analysis of the time domain DEER trace, for a frozen sample and in the absence of strong anisotropic interactions, provides a frequency domain spectrum, called the dipolar spectrum, and characterized by a *Pake Pattern* shape due to the

simultaneous presence in the same sample of multiple relative orientations of the molecule with respect to the external magnetic field $\boldsymbol{B_o}$. This spectrum contains information about the dipolar frequency of spin pairs at different relative orientations (see figure 2.9). The interspin distance can be obtained from the dipolar spectrum according to the equation:

$$\nu_{dd} = \frac{g_1 g_2 \beta_e \mu_0}{4\pi h r^3}(3cos^2\vartheta - 1) \qquad (2.7)$$

Equation (2.7) is quite similar to (1.21) except for the orientation term $(3cos^2\vartheta - 1)$ which accounts for the multiple relative orientations of the interacting spins with respect to the external magnetic field previously introduced, being ϑ the angle between the interspin vector $\boldsymbol{r}$ and the external magnetic field $\boldsymbol{B_o}$.

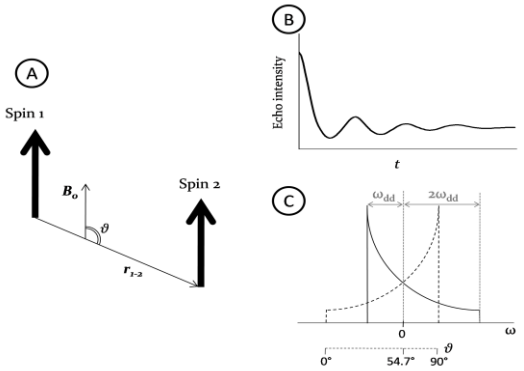

FIGURE 2.9 (A) REPRESENTATION OF THE DISTANCE VECTOR $\boldsymbol{r_{1-2}}$ BETWEEN SPIN 1 AND SPIN 2 AND THE $\boldsymbol{\vartheta}$ ANGLE BETWEEN $\boldsymbol{r_{1-2}}$ AND $\boldsymbol{B_o}$. (B) TIME DOMAIN MODULATION OF THE REFOCUSED ECHO INTENSITY DUE TO THE DIPOLAR INTERACTION. (C) CALCULATED PAKE PATTERN AND CORRESPONDENCE BETWEEN $\boldsymbol{\omega}$ AND $\boldsymbol{\vartheta}$ (LOWER SCALE).

A deeper analysis of the experimental data allows to obtain not only the main distance between two paramagnetic centers, but also the distance distribution, which is often a powerful source of structural information. DEER spectroscopy can be employed to investigate conformational motions and flexibility in the sub-nanometer range, making use of intrinsic paramagnetic sites or the well-developed spin labeling technique, employing for example nitroxide spin probes, as discussed in several dedicated papers and reviews [23-26].

2.6 Orientation selection in pulse EPR

All the pulse EPR sequences described in this chapter except for the FS-ESE are static field experiments, which means that the entire experiment is performed at a fixed value of the external magnetic B_o. Every microwave pulse employed is a nominal square pulses characterized by a short but finite length, in the order of few nanoseconds, which implies that the associated frequency profile, obtained by Fourier transform of the pulse function, is a *sinc* function ($sinc\,(x) = \frac{\sin\,x}{x}$). The full width at half maximum (FWHM) of the associated *sinc* pulse profile is usually considered as the pulse bandwidth, *i.e.* the frequency spectrum carried by an EM pulse centered at a fixed frequency due to the uncertainty principle. It follows that a typical 16 ns long $\pi/2$ pulse has an associated bandwidth of about 62.5 MHz ($1/t_p$ where t_p is the pulse length) or, moving to

magnetic field units, 2.2 mT (at g_e). Such a bandwidth is usually much smaller than the spectral width of a frozen solution EPR spectrum. The main consequence is that when a microwave pulse sequence is applied at a certain magnetic field value, only a small fraction of the entire spectrum is excited, or, in other words, only molecules with certain orientations with respect to the external magnetic field are selected by the choice of the B_o value, as illustrated in figure 2.10, and for this reason an orientation selection is performed during the pulse EPR experiment.

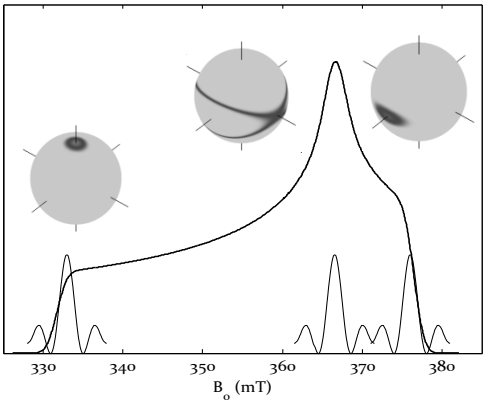

FIGURE 2.10 GRAPHIC REPRESENTATION OF THE ORIENTATION SELECTION IN PULSE EPR. SOLID LINE: CALCULATED FS-ESE SPECTRUM ($\boldsymbol{g_x = 1.85, g_y = 1.90, g_z = 2.10}$). BROKEN LINE: SHAPE OF A 16$\boldsymbol{ns}$ PULSE (FWHM=2.2 $\boldsymbol{mT}$) APPLIED IN CORRESPONDENCE OF THE THREE MAGNETIC FIELD VALUES CORRESPONDING TO THE PRINCIPAL VALUES OF THE $\boldsymbol{g}$ TENSOR. EXCITED ORIENTATIONS ARE REPRESENTED BY DARKER SHADES ON THE SPHERES REPRESENTING THE $\boldsymbol{g}$ TENSOR FRAME.

The orientation selection represents a powerful tool in pulse EPR investigation of powder sample, *i.e.* frozen solutions, since it allows to perform "single crystal-like" experiments on randomly oriented systems. Like a single crystal experiment, the orientation selection allows to select a restricted set of orientations of the sample when applying a specific pulse sequence and it can be changed by shifting the external magnetic field value. By means of such experiments, the complete determination of interaction tensors (*i.e.* principal values and orientation) is accessible also in the case of powder samples.

2.7 PHOTOEXCITED PULSE EPR

All the pulse EPR techniques described in the previous sections can be applied to photoexcited, transient paramagnetic species. In this thesis photoexcited pulse EPR will be acutely exploited to investigate the structure of molecular systems including paramagnetic centers in the photoexcited triplet state. These transient species are usually generated by pulse laser irradiation of samples in the resonator during the EPR experiment itself. As a rule of thumb when the short laser pulse (5 ns) is sent to the sample the triplet paramagnetic species is generated in a period in the order of 100 ns. Waiting a proper *delay after flash* period the complete microwave pulse sequence is driven to the sample and the EPR signal is recorded. Then the same sequence made of a laser shot followed by the microwave sequence is repeated until an adequate signal to noise ratio is

obtained as described in figure 2.11 for the case of the photoexcited FS-ESE technique.

As already discussed in chapter 1, photoexcited triplet states are characterized by a non-Boltzmann population of the three spin sublevels of the triplet state, defined as spin polarization. The spin polarization is responsible for the peculiar shape of the EPR spectra of frozen triplet state molecules. Spectra appear with both absorption and emission EPR lines depending on the relative population of the levels involved in the transitions. Moreover in a frozen powder spectrum, corresponding to frozen solutions, every orientation of the molecule with respect to the external magnetic field is represented with a specific probability weight. This is again manifested in the shape of the spectrum which is characterized by six sharp turning points, corresponding to two opposite transitions for every canonical orientation, where the external magnetic field lies parallel to one of the principal axis of the $\widetilde{D}$ tensor as reported in figure 2.11.

As a non-equilibrium paramagnetic species, the photoexcited triplet state begins to relax as soon as it is generated so in principle the whole microwave sequence operates on a decaying signal. The photoexcited triplet states are usually recognized as long-living transient species, whose characteristic relaxation times are of the order of several tenth of microseconds, much longer than the length of the entire microwave sequence (which usually ranges from 0.5 to 5 μs depending on the experiment). An interesting phenomenon related to the relaxation process is the anisotropic decays of the three

spin sublevels T_X, T_Y and T_Z. This relaxation reflects in the change of the intensity and the shape of the final spectrum as the delay after flash (DAF) is incremented giving time to the system to relax. Note that this effect is not always deleterious: sometimes, as is the case of carotenoid triplet state, the anisotropic decay of the triplet populations causes an increment of the intensity of a specific transition, thus making it more suitable for EPR investigation.

Combining different pulse EPR techniques with laser photoexcitation results in a wide range of powerful methods to deeply investigate the fine molecular and electronic interactions involved in the photosynthetic pathways. In this thesis, the photoexcited FS-ESE, ESEEM and DEER techniques have been employed in the structural investigation on both photosynthetic proteins and biomimetic model compounds, as will be discussed in chapters 4 and 5.

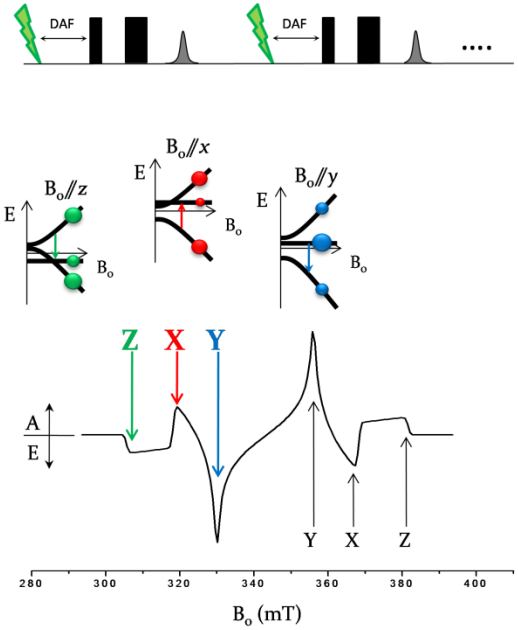

Figure 2.11 Top panel: photoexcited FS-ESE pulse sequence.. DAF stands for "delay after flash". Bottom panel: Calculated FS-ESE for a photoexcited tetraphenylporphyrin frozen solution at low temperature. All the six canonical transitions are marked. (see also figures 1.6 and 1.7). For the low-field ones also a schematic representation of relative population of the three sublevel is shown. The arrows denote the EPR transitions, while the circles are representative of the relative population of the level. Note the absorptive and emissive feature of the transitions due to the non-Boltzmann population of the triplet sublevels.

CHAPTER 3

THE COORDINATION ENVIRONMENT OF THE [4Fe4S] CLUSTER IN THE HydF PROTEIN AS PROBED BY ESEEM AND HYSCORE SPECTROSCOPIES

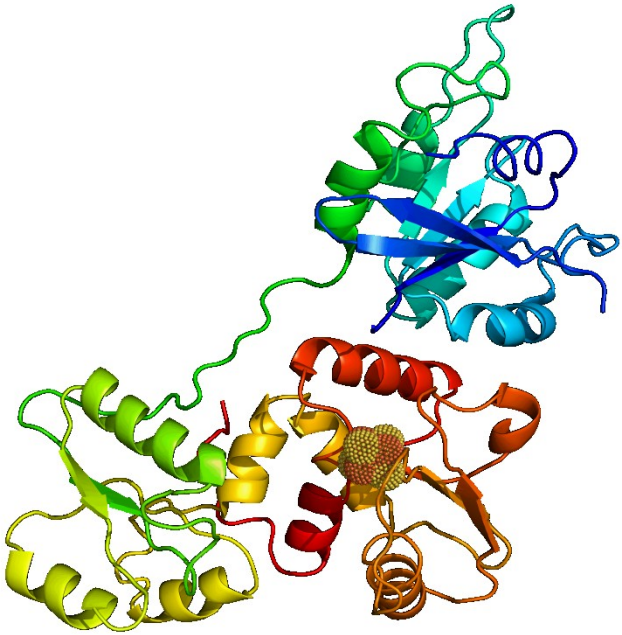

Hydrogenases are a wide group of enzymes capable of catalyzing the reduction of protons to molecular hydrogen and vice versa:

$$2H^{+}_{aq} + 2e^{-} \rightleftarrows H_{2,gas}$$

Hydrogenases are very common enzymes in nature, being found in bacteria, archea and some eukaryotic organisms. Specific metal active sites are generally required for the reaction to take place at the mild conditions of living organisms. From this point of view hydrogenases can be classified according to the composition of the active site, distinguishing into three phylogenetically distinct classes: [NiFe], [FeFe] and [Fe]-only hydrogenases [27, 28]. A peculiarity of [NiFe] and [FeFe] sites is the presence of the small and unusual inorganic molecules CO and CN^{-} ligated to the iron atom of the binuclear active site in addition to organic sulfur bridges between the two metal centers, while the third class, the [Fe]-only hydrogenases, is characterized by a single metal center in the active site with unusual coordination sphere which also contains CO ligands. A summing up of the three classes of hydrogenases active site is reported in figure 3.1.

While [NiFe] hydrogenases are predominantly hydrogen oxidizing enzymes, [FeFe] hydrogenases are usually more active in reducing protons to molecular hydrogen with a production rate that can reach 10^4 molecules of hydrogen per enzyme per second at room temperature [29]. This is a major reason for driving a huge amount of research on the hydrogenases theme in the last decade.

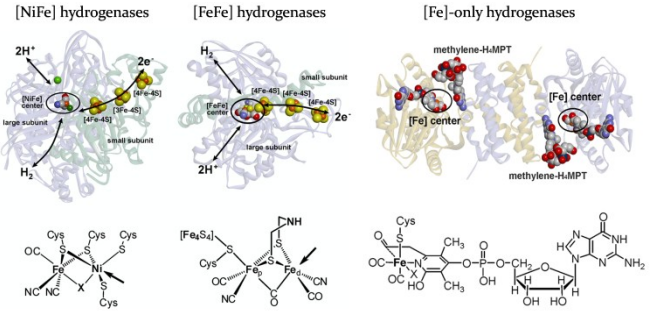

FIGURE 3.1 TOP: STRUCTURES OF [NIFE], [FEFE] AND [FE]-ONLY HYDROGENASES FROM DESULFOVIBRIO VULGARIS [30], *DESULFOVIBRIO DESULFURICANS* [31]AND *METHANOCALDOCOCCUS JANNASCHII* [32],RESPECTIVELY. BOTTOM: CHEMICAL STRUCTURE OF THE ACTIVE SITE. THE ACTIVE SITE OF [FEFE] HYDROGENASE, COMPOSED BY A BINUCLEAR [FEFE] MOIETY (THE SO-CALLED H-CLUSTER) LINKED TO A [4FE4S] CLUSTER IS OF PARTICULAR INTEREST FOR THE WORK. FIGURE TAKEN FROM [33].

A deep understanding of the molecular mechanisms responsible for the high catalytic efficiency of these enzymes could lead to the development of efficient and noble metal-free "artificial hydrogenases". These future, cheap devices will disclose the door for a "hydrogen economy" based on a clean production of hydrogen from renewable sources like water.

The work described in this chapter regards the investigation by means of CW and advanced pulse EPR techniques of the active site of the HydF protein. HydF is an accessory protein required to correctly assemble and insert the binuclear active site of [FeFe] hydrogenase, the so-called H-cluster. According to this specific role, this protein is also usually referred to as a *maturase* protein together with the HydE and HydG proteins.

3.1 An outline on the HydF protein

Maturase regulatory proteins, HydE, HydF and HydG, were discovered in the early 2000s after they were identified as strictly essential players for the proper formation of the [FeFe] hydrogenase HydA [34, 35]. Among these, HydF holds the pivotal double role of scaffold on which the [FeFe] H-cluster is properly built by the action of HydE and HydG and the role of carrier of the latter into the *apo*-HydA protein, terminating in this way the maturation process [36-39]. The peculiar role of the three proteins involved, particularly regarding HydE and HydG, is still not clear and different maturation pathways has been drawn since now. The most recent complete maturation pathway scheme has been proposed in 2014 [33]; it gathers results from several previous investigations on the single steps of the process into a unitary plan. The schematic representation is reported in figure 3.2.

Recently, it has been demonstrated that HydF binds a totally inorganic [4Fe4S] cubane-like cluster and also a 2Fe unit, but only the latter is effectively transferred to the *apo*-HydA in the very last step of the hydrogenase maturation [37, 40]. All HydF proteins known to date share a common [4Fe4S] binding motif in the primary structure ($CxHx_{46-53}HCxxC$) with three cysteine and two histidine highly conserved residues that are supposed to participate to the binding of the cluster. The three dimensional structure of HydF from *Thermotoga neapolitana* (*Tn*) was recently solved at atomic

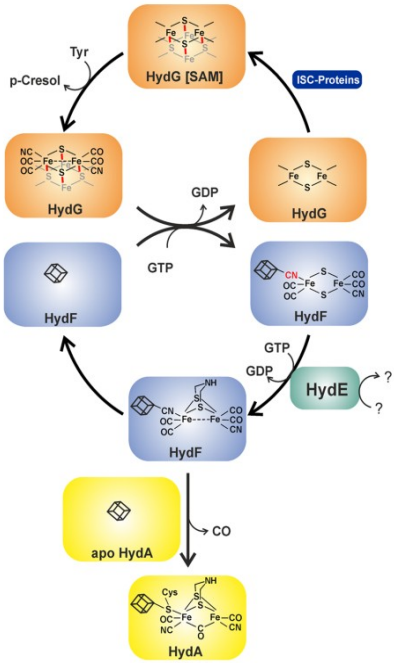

FIGURE 3.2 PROPOSED MECHANISM OF [FEFE] HYDROGENASE MATURATION. HYDF RECEIVES A PREFORMED 2FE MOIETY FROM HYDG. IT IS THEN COMPLETELY FORMED WITH THE INSERTION OF AN AMINO-DITHIOL BRIDGING LIGAND BY HYDE AND FINALLY TRANSFERRED TO THE *APO*-HYDA PROTEIN.

resolution but unfortunately only the oxidized *apo* form, a [4Fe4S] lacking HydF protein in which all the three conserved cysteine residues are involved in intra- and inter-molecular cystinyl bridges, has been crystallized [41]. The asymmetric unit is constituted by a monomer but the biological active form is the dimer or the tetramer of the protein. Three different domains can be observed in the crystallized $HydF_{Tn}$ monomer: the already cited [4Fe4S] binding domain located in the C-terminus region; a GTP binding domain, structurally related to that of other GTPases, where conserved amino

acids useful for the hydrolysis of GTP are situated; and finally a dimerization domain located in the central portion of the enzyme, as represented in figure 3.3.

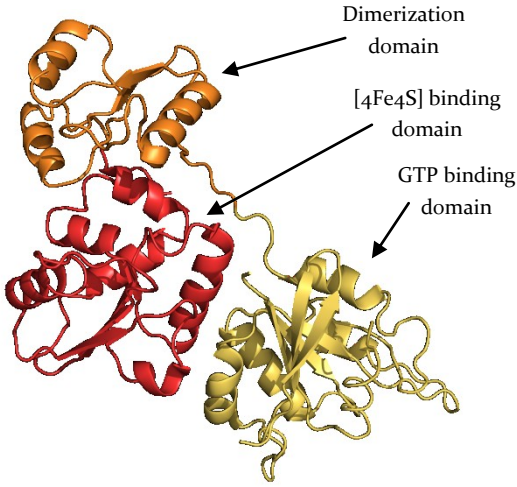

FIGURE 3. 3CARTOON REPRESENTATION OF THE MONOMER HYDF$_{TN}$ PROTEIN. DIFFERENT COLORS INDICATES THE THREE FUNCTIONAL DOMAINS OF THE PROTEIN. PDB ENTRY: 3QQ5 [41].

The aim of the present investigation is to characterize the cluster coordination surrounding of the [4Fe4S] cluster from HydF$_{Tn}$, unveiling the role of the three conserved cysteines and identifying the nature of the fourth ligand, also in relation with data published for other HydF proteins.

3.2 The role of the conserved cysteine residues in the coordination of the [4Fe4S] cluster in the HydF protein

Previous investigations based on site-specific mutagenesis indicate that at least two of the three conserved cysteines in the [4Fe4S] binding domain are essential for the assembly of a functional H-cluster in HydF from *Clostridium acetobutylicum* (*Ca*) [42]. In our investigation of the cysteine role in both *Tn* and *Ca*, a series of mutated *holo*-HydF proteins has been expressed and purified from *Escherichia coli*. Site-directed mutagenesis has been addressed to the three conserved cysteine residues C302, C353 and C356 in the cluster binding domain of $HydF_{Tn}$ as illustrated in figure 3.4, which were substituted with the isosteric residue serine. Sodium dithionite was added prior of freezing the solution of protein, under nitrogen atmosphere, in order to reduce the cluster from the EPR silent $[4Fe4S]^{3+}$ to the $[4Fe4S]^{+}$ which instead is EPR active with a total spin ½ (for the details of the protein expression and purification and the sample preparation for EPR investigation see appendix A.1).

The CW-EPR investigation on the three mutants compared to the wild type (WT) HydF from *Tn* is illustrated in figure 3.5 (for the spectrometer condition at which these spectra and the following have been obtained see Appendix A.1). Spectra of as-isolated $HydF_{Tn}$ prior of the reduction are reported in panel A.

The WT form shows two intense signals centered around g=2.00 and g=4.30 which are easily assigned to an oxidized $[3Fe4S]^{+}$ cluster and non-specifically bounded Fe(III) respectively.

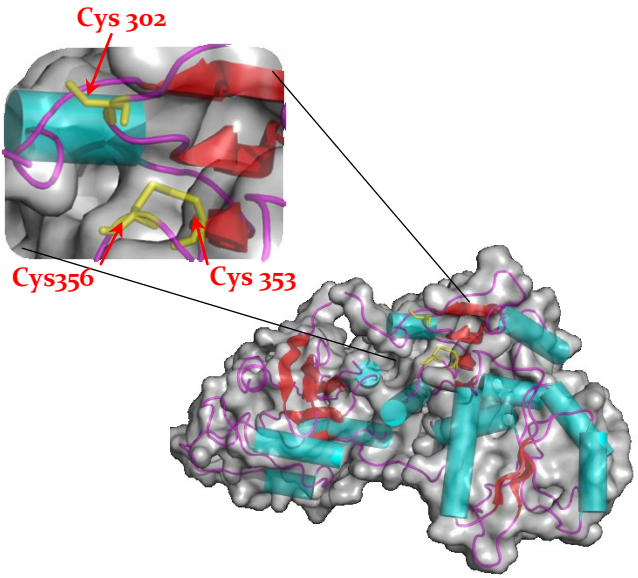

FIGURE 3.4 CARTOON REPRESENTATION OF HYDF PROTEIN MONOMER FROM ***Tn*.** THE INSET SHOWS THE THREE CONSERVED CYSTEINE RESIDUES. NOTE THE CYSTINYL BRIDGE BETWEEN C353 AND C356 DUE TO THE OXIDIZING CONDITIONS DURING CRYSTALLIZATION (SEE TEXT).

After reduction with sodium dithionite (figure 3.5, panel B) new EPR signals characterized by a quasi-axial profile are observed in the region ranging from g=2.1 to g=1.8. The g-tensor principal values, g_x=1.850 g_y=1.895 g_z=2.044, have been obtained from spectral simulation. The signal is assigned to the S=1/2 $[4Fe4S]^{+}$ cluster as previously

reported for HydF from *Thermotoga maritima* (*Tm*) [43]. Interestingly, the substitution of every cysteine residue causes the disappearance of the axial signal due to the assembled [4Fe4S] cluster, a clear sign that the three highly conserved cysteines are all essential for a correct cluster assembly in $HydF_{Tn}$.

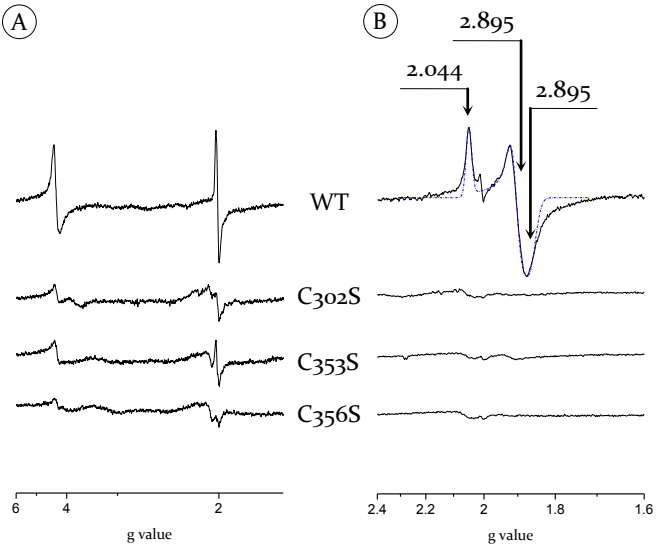

FIGURE 3.5 X-BAND CW-EPR SPECTRA OF WILD TYPE AND MUTANT HYDF PROTEIN FROM ***Tn*** IN FROZEN SOLUTION (10K). PANEL A:AS-ISOLATED PROTEIN, SHOWING THE g=4.3 AND THE $[3Fe4S]^{+}$ SIGNALS. PANEL B: REDUCED PROTEIN WITH THE ADDITION OF 20***mM*** SODIUM DITHIONITE. THE SPECTRAL SIMULATION OF THE EPR SPECTRUM OF THE WT PROTEIN IS ALSO REPORTED (DOTTED LINE). THE PROTEIN CONCENTRATION RANGES FROM 100μM TO 300 μM.

In the CW-EPR spectrum of reduced WT HydF protein a narrow signal is also noticeable in the g=2 region (almost undetectable in the spectra of mutants). A temperature dependence analysis reveals that this signal reaches a

maximum at about 40 K, while the signal due to the [4Fe4S] cluster progressively decays at temperatures higher than 20 K. Its origin is attributed to the presence of the reducing agent (sodium dithionite), but its nature is still unknown. Moreover, the relaxation behavior of this signal suggests that it is located near the cluster so that a role in the catalytic process has not to be excluded.

As already stated above, all HydF proteins known to date share a highly conserved [4Fe4S] binding motif at their C-terminus composed of three cysteines and two histidines. CW-EPR reveals that substituting one of the sulphydryl group with the hydroxyl of the serine residue (which has been found before in few cases as an alternative ligand for FeS clusters [44-46]) results in the complete inability of assembling the cluster by the $HydF_{Tn}$ protein. Similar results has already been postulated for two of the three conserved cysteine residues, namely C353 and C356 in $HydF_{Ca}$ [42]. Our results on the $HydF_{Tn}$ indicate that mutation of the C304 residue in $HydF_{Ca}$ is expected to cause the cluster assembly to fail too. We investigated this hypothesis by means of an H_2 evolution assay on the [FeFe]-hydrogenase when matured with both wild-type and C304S mutant $HydF_{Ca}$ protein. Results denote a significant decrease in the production of molecular hydrogen from reduced methylviologen from a value of 70±9.5 nanomoles of H_2 per milliliter of cell culture solution per minute for the WT-$HydF_{Ca}$ to an undetectable signal for the hydrogenase matured in presence of C304S-$HydF_{Ca}$.

3.3 The role of the two conserved histidines in the binding process of the [4Fe4S] cluster in HydF

It is well known that a typical [4Fe4S] cubane-like cluster requires four ligand to complete the coordination sphere, one for each iron ion at the cluster's edge. Our CW-EPR investigation identified three of the four ligands to be the conserved cysteines in both HydF from *Tn* and *Ca*. The best candidates to the role of fourth cluster ligand are the two histidine residues in the conserved cluster-binding motif ($CxHx_{46\text{-}53}HCxxC$). As reported in figure 3.6 a closer look to the crystal structure of *apo*-$HydF_{Tn}$ reveals that H304 and H352 are in close proximity to the hypothetical cluster location, suggesting the possible involvement of histidine nitrogen in the ligation of the [4Fe4S] cluster, which is a common feature among FeS clusters in nature as among hydrogenases themselves [47, 48].

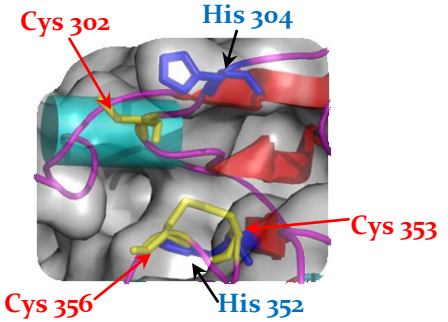

Figure 3.6 Cartoon representation of the [4Fe4S] cluster coordinative site. Coordinating cysteines are depicted as yellow bold segments. The two conserved histidine residues H304 and H352 are depicted as bold blue segments.

A previous HYSCORE investigation on the cluster coordination of HydF from *Tm* has definitely excluded the presence of any nitrogen-based ligand [43], making our investigation more intriguing because of a potential non-conventional and organism-dependent type of coordination. Our analysis started from the CW-EPR, as in the previous paragraph, to test possible macroscopic implication of histidine/alanine substitution on cluster assembly. Results are reported for reduced HydF protein from both the organisms in figure 3.7.

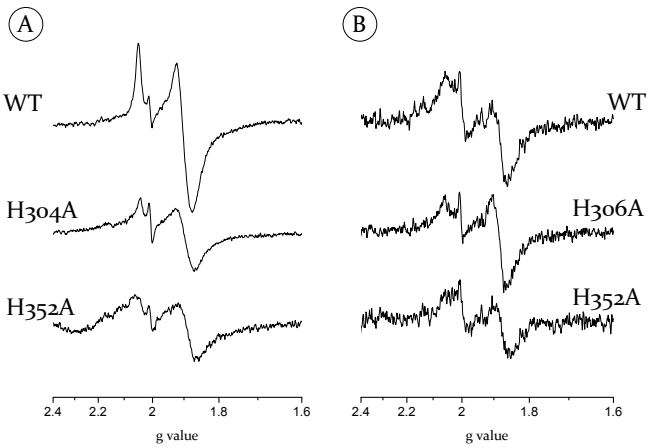

FIGURE 3.7 X-BAND CW-EPR SPECTRA OF WILD TYPE AND MUTANT REDUCED HYDF PROTEIN IN FROZEN SOLUTION (10K) FROM ***Tn*** (PANEL A, PROTEIN CONCENTRATION AS IN FIGURE 3.5) AND ***Ca*** (PANEL B, PROTEIN CONCENTRATION RANGES FROM 50 ***μM*** AND 250 ***μM***).

As it can be inferred directly from the EPR spectra, substitution of the conserved histidine residues in the cluster binding motif does not compromise the correct assembly and ligation of the [4Fe4S] cluster in both the organisms under investigation. The spectra of the

$HydF_{Ca}$ protein appear far less intense than the corresponding ones for $HydF_{Tn}$ due to a reduced protein concentration.

The *g*-tensor principal values have been obtained by means of spectral simulation. WT-$HydF_{Ca}$ is characterized by the same quasi-axial signal recorded for WT-$HydF_{Tn}$ but with slightly different values: g_x=1.831 g_y=1.874 g_z=2.050. Interestingly, the substitution of H304 (H306) does not affect the *g* values of the spectra at all, meaning that negligible changes are introduced in the cluster surrounding when this residue is replaced with the hydrophobic alanine and suggesting a minor involvement of H304 (H306) in the cluster coordination. On the contrary mutants H352A from both organisms exhibit a slight shift of the *g*-tensor principal values (1.840, 1.875 and 2.055 in H352A-$HydF_{Tn}$ and 1.836, 1.862 and 2.045 in H352A-$HydF_{Ca}$).

CW-EPR indicates that there could be some minor involvement of the two conserved histidine residues but those residues are definitely not as crucial for cluster assembly as the cysteine residues are. To better characterize the role of H304 (H306) and H352 in the coordination of the cluster and possibly unveil some implications in the catalytic process we performed low-temperature HYSCORE spectroscopy on the paramagnetic $[4Fe4S]^+$ cluster of the reduced wild-type and histidine-mutant HydF proteins from both *Tn* and *Ca*. HYSCORE spectroscopy is particularly useful in this case since the interaction of the paramagnetic species with surrounding nitrogen nuclei is clearly observable as reported in several works [49-54]. The HYSCORE

frequency map obtained for the wild-type HydF protein from *Tn* and *Ca* in correspondence of the most prominent g_y field position are reported in figure 3.8.

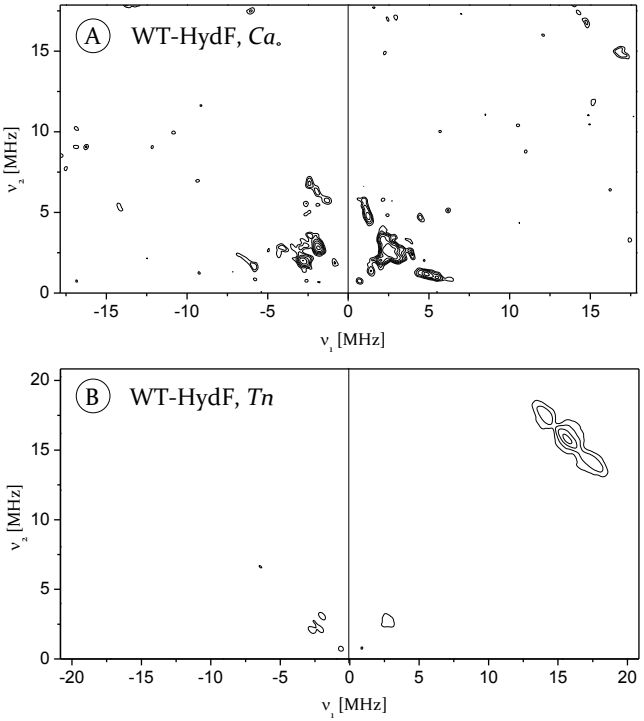

FIGURE 3.8 HYSCORE SPECTRA OF REDUCED WILD-TYPE HYDF PROTEIN FROM ***Ca*** (PANEL A) AND FROM ***Tn*** (PANEL B) IN FROZEN SOLUTION (10K)RECORDED AT A MAGNETIC FIELD CORRESPONDING TO THE g_y POSITION.

Differences between the two spectra are clearly evident and concern mainly the low frequency region between 0 and ±7.5 MHz in both the quadrants. These signals are fingerprints of one or more interacting nitrogen nuclei and are found only in $HydF_{Ca}$, thus unquestionably excluding a nitrogen coordination of the cluster in

$HydF_{Tn}$ and at the same time indicating an organism-dependent coordination of the [4Fe4S] cluster in HydF proteins. Moreover, the presence of nitrogen signals also in the left quadrant (the so-called +- quadrant) are indicative of a strong coupling regime in which the hyperfine interaction, expressed in frequency units, is more than twice larger than the Larmor frequency of the nitrogen ($A \gg 2\omega_L$), being the Larmor frequency of ^{14}N 1.077 MHz at 350 mT.

In the case of the interacting nitrogen found in $HydF_{Ca}$ quadrupolar and hyperfine terms has been obtained from the so-called double quantum transition cross-peaks, the prominent signals located at (-2.6; 6.6) and (-6.6; 2.6) MHz. The values of the total hyperfine interaction along g_y A_{gy} = 4.2±0.2 MHz and of the quadrupolar term $K^2(3+\eta^2)$ = 0.71 MHz^2 are in the range of those reported for histidine ligands of iron-sulfur clusters [54-57]. In order to identify the fourth ligand of the [4Fe4S] from $HydF_{Ca}$, we have performed HYSCORE spectroscopy on the two histidine mutants H306A and H352A. The results are summed up in figure 3.9 together with the HYSCORE map corresponding to the WT-$HydF_{Ca}$ for comparison. Again significant differences between the two mutants are observable in the nitrogen fingerprint region of the spectra. The H306A mutant shows the same nitrogen pattern of the wild-type, with the same quadrupolar and hyperfine interaction terms while interestingly the spectrum of the H352A mutant lacks all the cross-peaks due to a strongly coupled nitrogen, clearly indicating that the histidine 352 is the fourth ligand of the [4Fe4S] cluster of HydF from *Ca*.

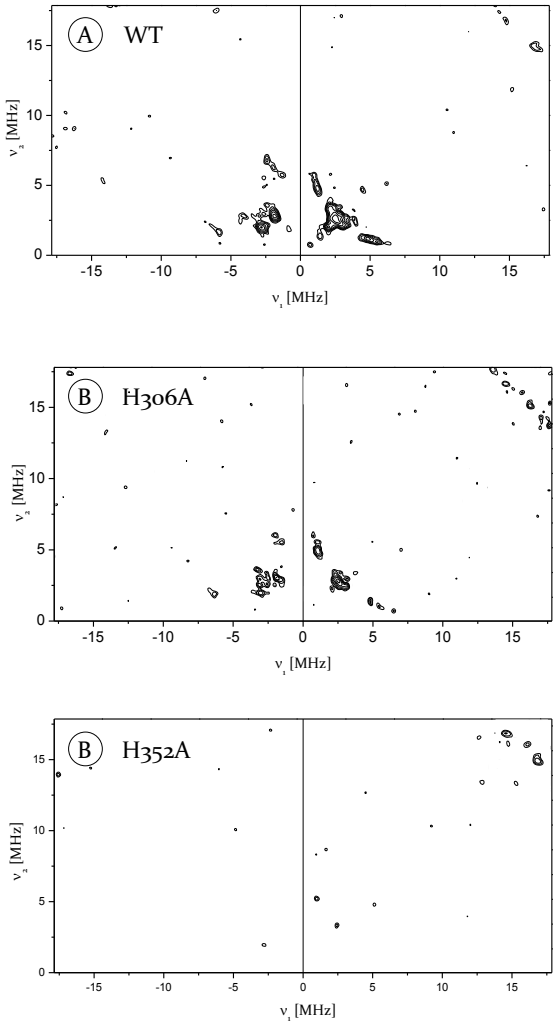

Figure 3.9 HYSCORE spectra of the reduced $HydF_{CA}$ protein in frozen solution (10K) recorded in correspondence of the g_y field position. Panel A: WT-$HydF_{CA}$. Panel B: H306A-$HydF_{CA}$. Panel C: H352A-$HydF_{CA}$.

Experimental results on the HydF protein from the two organisms reveal that only the three conserved cysteines are strictly required for cluster binding, whereas the fourth ligand can vary depending on the species. This evidence to speculate that the non-cysteinyl coordination as well its variability may have some implications in the complete assembly of the H-cluster precursor in HydF. Non-cysteinyl ligation of iron-sulfur clusters occurs in several enzyme and in each case it has a functional significance [58, 59]. The two conserved histidines might have some functional role although they are not involved in the direct coordination of the cluster, as expected from their high degree of conservation. For example, it has been demonstrated via hydrogen evolution assays that both H306 and H352 residues, which are not crucial for cluster assembly in *Ca* (see fig. 3.7), are strictly required for a correct [FeFe]-hydrogenase activation, a result that could be extended *bona fide* to the *Tn* case [60].

3.4 The proton environment of the [4Fe4S] cluster of the HydF protein from Thermotoga neapolitana

The interchangeability of the fourth coordination position of the [4Fe4S] cluster formerly described has driven our attention to the investigation of the non-nitrogen ligation of the cluster in the $HydF_{Tn}$ protein. Few examples of oxygen coordination to iron-sulfur cluster are reported in literature, mainly regarding

serine, aspartate or glutamate residues [44-46]. Looking close to the crystal structure of *apo*-HydF$_{Tn}$ four highly conserved oxygen-based ligands can be found in the vicinity of the [4Fe4S] cluster binding site which could be potential ligands, *i.e.* E300, D310, D337 and Y380 as depicted in figure 3.10. Following the same procedure employed in the EPR investigation described in the previous paragraphs a wide site-directed mutagenesis has been performed in order to selectively substitute the four selected residues with alanine.

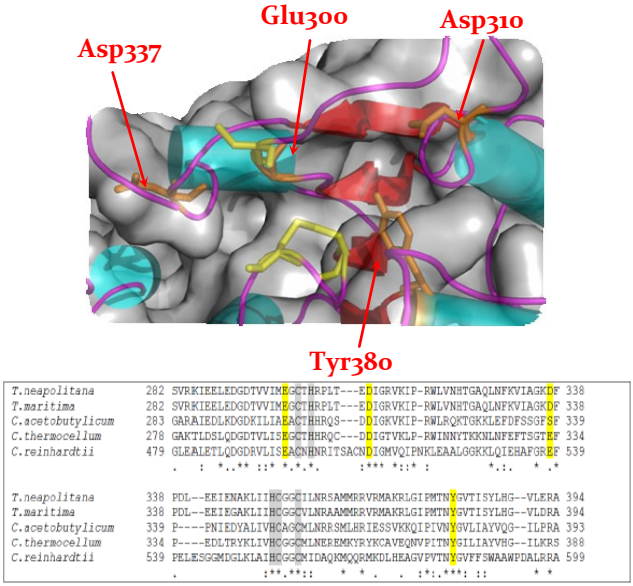

FIGURE 3.10 TOP PANEL: CARTOON REPRESENTATION OF THE [4FE4S] CLUSTER COORDINATIVE SITE. COORDINATING CYSTEINES ARE DEPICTED AS YELLOW BOLD SEGMENTS. POTENTIAL OXYGEN-BASED ENDOGENOUS LIGANDS ARE REPRESENTED AS BOLD ORANGE SEGMENTS. BOTTOM PANEL: MULTIPLE SEQUENCE ALIGNMENT OF THE C-TERMINUS OF HYDF PROTEINS FROM DIFFERENT ORGANISMS. CONSERVED CYSTEINES AND HISTIDINES ARE HIGHLIGHTED IN GREY, MUTATED OXYGEN-BASED RESIDUES ARE HIGHLIGHTED IN YELLOW.

Low-temperature CW-EPR on the reduced $HydF_{Tn}$ proteins and the corresponding spectral simulations, reported in figure 3.11, reveal that the investigated residues are not crucial for the correct cluster assembly, since the reduced cluster signal is always observable with comparable yields and minor effects on *g* factors (collected in table 3.1).

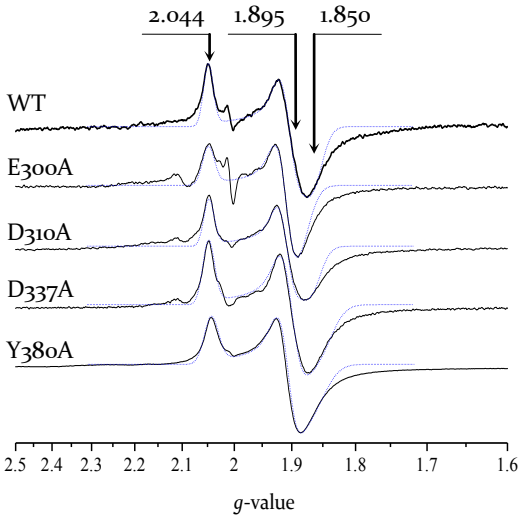

FIGURE 3.11 X-BAND CW-EPR SPECTRA OF FROZEN SOLUTION (10K) OF WILD TYPE AND MUTANT HYDF PROTEIN IN FROZEN SOLUTION (10K) FROM ***Tn*** (SOLID LINE)TOGETHER WITH SPECTRAL SIMULATIONS (DOTTED LINE). PROTEIN CONCENTRATION RANGES FROM 100***μM***AND 300 ***μM***.

TABLE 3.1 SPECTROSCOPIC PARAMETERS USED IN THE SIMULATIONS OF THE CW-EPR SPECTRA REPORTED IN FIGURE 3.11

	g_z, g_y, g_x	Isotropic linewidth (mT)
Wild-Type	2.044, 1.895, 1.850	2.5
E300A	2.047, 1.910, 1.878	1.0
D310A	2.046, 1.907, 1.867	2.5
D337A	2.045, 1.896, 1.853	1.0
Y380A	2.043, 1.905, 1.866	2.5

As already noticed during the investigation on the role of the conserved histidine residues, only important changes upon substitution can be traced with CW-EPR, *i.e.* disappearance of the signal when the cluster in not assembled or variations of the g-factors when the geometry of the cluster and the ligand environment is varied. In order to unveil possible minor interaction between oxygen-based residues and the cluster, the same samples has been HYSCORE. The most abundant isotope of oxygen (99.76%) is ^{16}O which is magnetically silent (I=0), so HYSCORE cannot reveals directly the interaction of the cluster with surrounding oxygen nuclei. The HYSCORE map of the reduced WT-HydF_{Tn} protein reported in figure 3.8, panel A, shows only cross-peaks in the region of 15 MHz, easily assigned to protons in proximity of the cluster, being the free Larmor frequency of proton 15.3 MHz at 350 mT. Spectral resolution has been improved here with the aim of recognizing minor changes in the proton environment which could highlight possible interaction of the cluster with the four oxygen-based residues considered. The proton region of the corresponding HYSCORE spectra are reported in figure 3.12. Three different ridges are

clearly observable in all the spectra numbered from I to III, underlined by colored lines in figure 3.12.

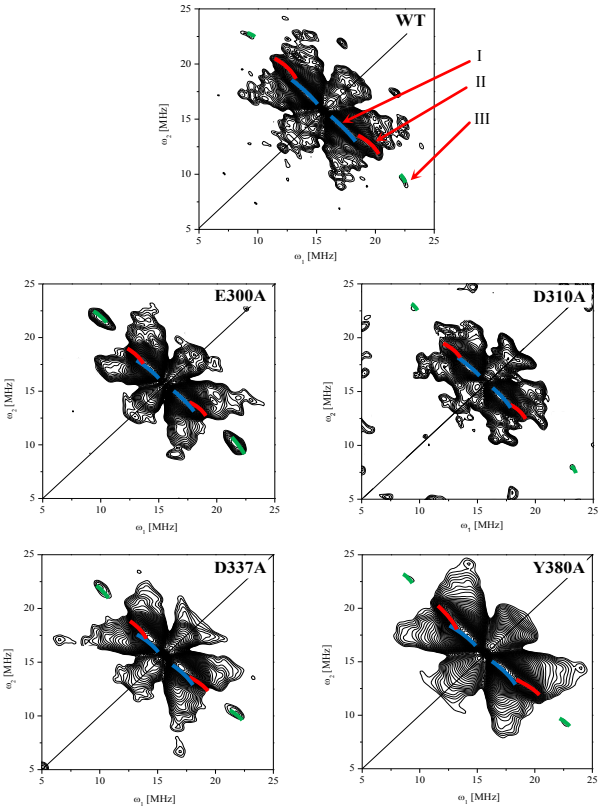

FIGURE 3.12 PROTON REGION OF THE HYSCORE SPECTRA OF REDUCED WT AND MUTANT HYDF PROTEIN FROM ***Tn*** IN FROZEN SOLUTION (10 K)RECORDED AT THE g_y POSITION (SEE FIGURE 3.11). COLOR CODE: BLUE=RIDGE *I*; RED=RIDGE *II*; GREEN=RIDGE *III*.

Ridge III is characterized by a strong hyperfine coupling ranging from 14 to 16 MHz, with a major isotropic component as suggested by the large displacement from

the anti-diagonal line, which indicates that these protons are bounded to some spin-bearing atom. Comparison with literature data on iron-sulfur clusters suggests that these cross-peaks are the signature of the β-cysteinyl methylenic protons of the three coordinating cysteine residue which are invariably characterized by large hyperfine interactions [56, 61-65].

Based on this assignment, ridges III are supposed to be present in every mutant investigated and thus are not really informative about changes in cluster surrounding upon mutations. Ridges I and II instead originate from less interacting protons but still in the coordination sphere of the cluster as they lay closer to the anti-diagonal line. For this reason they can be considered as sort of marker for the fine adjustments of the proton environment. Negligible variation of these ridges are observed comparing the WT and the explored set of mutant, which can be taken as an evidence that the investigated oxygen-based residues are neither involved in the direct coordination of the cluster nor in specific interactions such as H-bond bridges in close proximity to the cluster of $HydF_{Tn}$ protein [66].

These observations have stimulated the hypothesis that the potential ligand for the [4Fe4S] cluster of the HydF from *Tn* could be a sulfur- or oxygen-based molecule. For this reason we have performed a deeper investigation of the proton environment by means of high resolution HYSCORE spectroscopy at the three field positions corresponding to the *g*-tensor principal axes combined with D_2O exchange in order to investigate the accessibility and exchangeability

properties of the site. Results are summed up in figure 3.13, where WT and D_2O-exchanged $HydF_{Tn}$ spectra are compared in order to highlight the effect of proton to deuteron substitution.

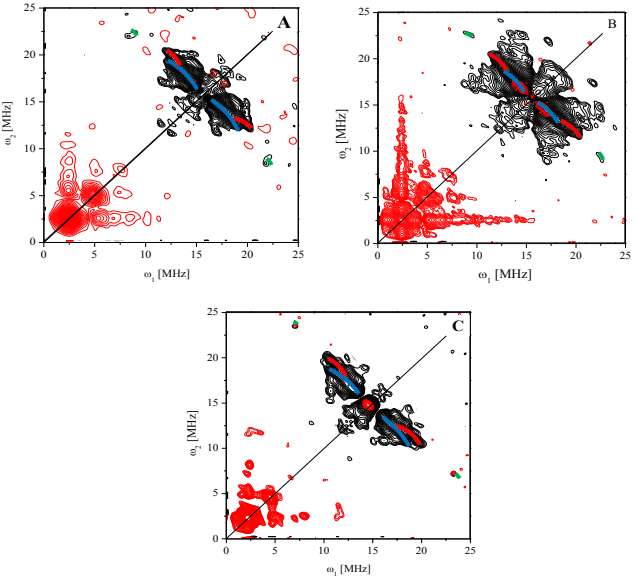

FIGURE 3.13 HYSCORE SPECTRA OF REDUCED WT-HYDF PROTEIN FROM ***Tn*** IN FROZEN SOLUTION (10 K) BEFORE (BLACK CONTOUR) AND AFTER (RED CONTOUR) D_2O EXCHANGE, RECORDED AT FIELD POSITIONS CORRESPONDING TO THE PRINCIPAL VALUES OF THE $\boldsymbol{g}$ TENSOR. COLOR CODE: BLUE=RIDGE *I*; RED=RIDGE *II*; GREEN=RIDGE *III*.

Spectra relative to the WT-$HydF_{Tn}$ (black contours in figure 3.13) show a very poor anisotropy on moving from the quasi-equivalent g_x and g_y field positions toward the g_z. Significant differences between the spectra in terms of number and position of the ridges are immediately noticed in the D_2O-exchanged sample. Ridge III is the only one appearing entirely conserved upon deuterium

exchange (the effect is particularly evident in correspondence of the g_z position, while on the g_x and g_y positions it is slightly less trivial because of the presence of τ dependent blind spots).

This evidence strongly supports the previous assignment of this ridge to the non-exchangeable, strongly interacting β-cysteinyl protons of the cluster-coordinating cysteines. On the contrary, the D_2O exchange completely affects the sharp ridge number II, which is no longer observable in the proton region of the HYSCORE spectra at any field position, suggesting an easy exchangeability of these protons. The third set of protons already identified (ridge number I) partially disappears when the deuterium exchange is performed, underlining their exchangeability but at the same time a weak signal in the proton region, clearly visible only in correspondence of the most intense g_y position, is still persisting. This unexchangeable ridge has a clearly different shape with respect to the overlapped ridge number I, appearing less elongated and curved, suggesting that it belongs to a fourth family of non-exchangeable protons never observed before. The position near the diagonal line and the slight curvature of the ridge both suggest that the protons giving rise to this signal are characterized by small hyperfine values and could be tentatively assigned to weakly coupled, non-exchangeable protons belonging to the protein environment of the cluster. Focusing on the low-frequencies region of the HYSCORE map, several new cross-peaks appear after D_2O exchange which demonstrates that some deuterium atoms effectively move in close proximity to the [4Fe4S] cluster.

In order to disentangle these crowded spectral regions and to better characterize the proton region signals, the complete computer fitting of the frequency domain of the HYSCORE spectra before and after deuterium exchange has been performed using an home-written Matlab® routine based on the Easyspin package [18].Simulation of the exchangeable proton region before the deuterium exchange is reported in figure 3.14, for the two most significant field positions corresponding to g_y and g_z. The simulation of ridges I and II is satisfying when two different sets of protons, characterized by distinct hyperfine parameters, are employed. Surprisingly no orientation selection at all is needed for the simulation.

More Looking at simulations more in detail, ridge I is characterized by a null isotropic hyperfine interaction and a dipolar term of 3.0±0.5 MHz which correspond to a distance of 3±1 Å, being the uncertainty given both by the error on the dipolar interaction estimation and to the ambiguity on the spin projection factor of the total spin of the cluster onto the ligated iron ion as described in [67]. The simulation of ridge II requires a 3.5±1.0 MHz isotropic contribution and a 5.0±0.5 MHz dipolar term (T parameter), which both suggest a stronger interaction with the cluster and a shorter distance, ranging between 2.1 Å and 3.0Å. The relatively large isotropic contribution to the hyperfine coupling denotes a considerable extension of the cluster wavefunction onto protons of ridge II, thus supporting the proximity of these fully exchangeable protons to the paramagnetic center. Hyperfine parameters employed for the simulation of

the HYSCORE maps and the corresponding distances are reported in table 3.2.

The same parameters, opportunely scaled for the ratio of the magnetogyric ratio between proton and deuterium nuclei ($\gamma_H/\gamma_D = 6.514$, correctly simulate the HYSCORE spectra of the D_2O-exchanged sample at both field positions investigated as reported in figure 3.14. This result clearly highlights the accuracy of the simulation parameters employed for the proton region and remarks the exchangeability properties of protons belonging to ridge I and II.

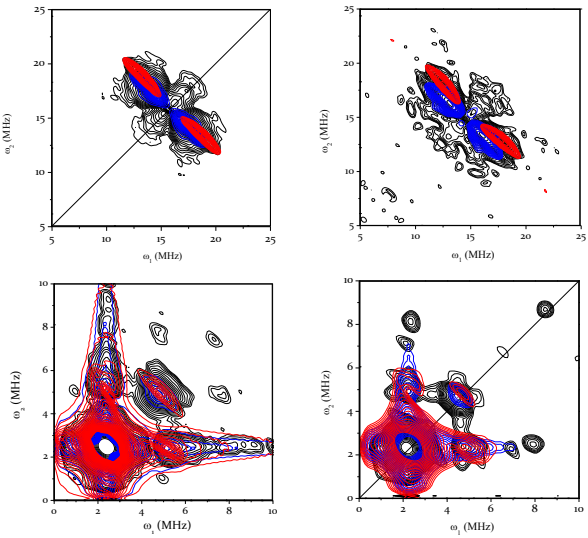

FIGURE 3.14 HYSCORE SPECTRA AND RELATIVE SIMULATIONS FOR THE HYDF PROTEIN FROM ***Tn*** IN FROZEN SOLUTION (10 K) MEASURED AT g_y AND g_z (SEE FIGURE3.5). BLACK CONTOURS ARE THE EXPERIMENTAL DATA, BLUE AND RED CONTOURS REPRESENT THE SIMULATED CONTRIBUTIONS OF RIDGE I PROTONS (BLUE) AND RIDGE II PROTONS (RED).TOP PANELS: PROTON REGION OF THE WILD TYPE PROTEIN. BOTTOM PANELS: DEUTERIUM REGION OF THE D_2O-EXCHANGEDPROTEIN.

The HYSCORE simulation has been performed also for the new set of unexchangeable protons, which appears after deuterium exchange in the proton region. Results are summed up in figure 3.15 and in table 3.2 Both the null value of the isotropic hyperfine constant and the small value for the dipolar interaction (2.5±0.5 MHz *T* parameter corresponding to a 3.3±0.5 Å distance in the point-dipole approximation) support the assignment of this extra ridge to a set of protons belonging to the protein backbone or to residues located around the cluster, looking in detail at the crystal structure of *apo*-$HydF_{Tn}$.

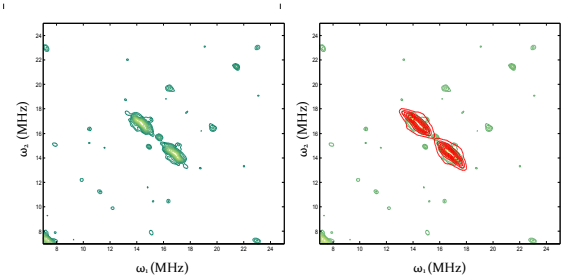

FIGURE 3. 15 HYSCORE MAP (LEFT PANEL) AND CORRESPONDING SIMULATION (RIGHT PANEL, RED CONTOUR LINES) OF THE PROTON REGION FOR THE D_2O-EXCHANGED REDUCED HYDF PROTEIN FROM ***Tn*** IN FROZEN SOLUTION (10 K). RIDGE NUMBER IV IN THE TEXT.

In order to further strengthen the estimation of the hyperfine parameters obtained from HYSCORE simulations and to determine the number of protons directly involved in the exchange process, 3p-ESEEM experiments have been performed on both the wild type and D_2O-exchanged $HydF_{Tn}$ protein in frozen solution. The time traces, collected in correspondence to six different values of the external magnetic field ranging

from g_z = 2.044 to g_x = 1.850, are shown in figure 3.16. The traces are presented as ratios between the traces of the D_2O-exchanged and the untreated proteins in order to cancel out contributions to the modulation due to unexchangeable protons. The time traces have been Fourier transformed according to the procedure described in [68] to obtain frequency domain spectra (for the details see appendix A.1). The time traces reveal the presence of deep modulations due to the interaction of the cluster with surrounding deuterium nuclei. At the same time no orientation selection can be noticed, the change in the modulation frequency being a pure effect due to the shift of the deuterium Larmor frequency on sweeping the external magnetic field. Simulations of the 3p-ESEEM time and frequency domains have been performed using an home-written FORTRAN® routine (for the details see appendix A.1). Hyperfine parameters for the exchangeable protons belonging to ridges I and II derived from the previous simulation of the HYSCORE maps completely fit the simulation of the 3p-ESEEM traces as reported in figure 3.16.

Simulation of both time and frequency 3p-ESEEM traces allow to obtain in addition the important information on the number of interacting deuterons, which is not achievable simply by the HYSCORE map simulation. Two deuterons with the parameters of set I, derived from the HYSCORE simulations, and a single deuteron from set II have been here employed in the simulation. A number of weakly interacting matrix deuterons has also been added in order to correctly reproduce the traces. A set of 30 exchangeable matrix deuterons has been also considered, estimating the number of the protein

exchangeable protons in proximity to the hypothetic cluster position (distance < 10 Å, T term of the dipolar interaction calculated from the point-dipole approximation stronger than 0.035 MHz). The number of the strongly interacting exchangeable protons is in agreement with the sharpness of the HYSCORE ridges, which indicates that a small and precise number of protons is giving rise to the ridge.

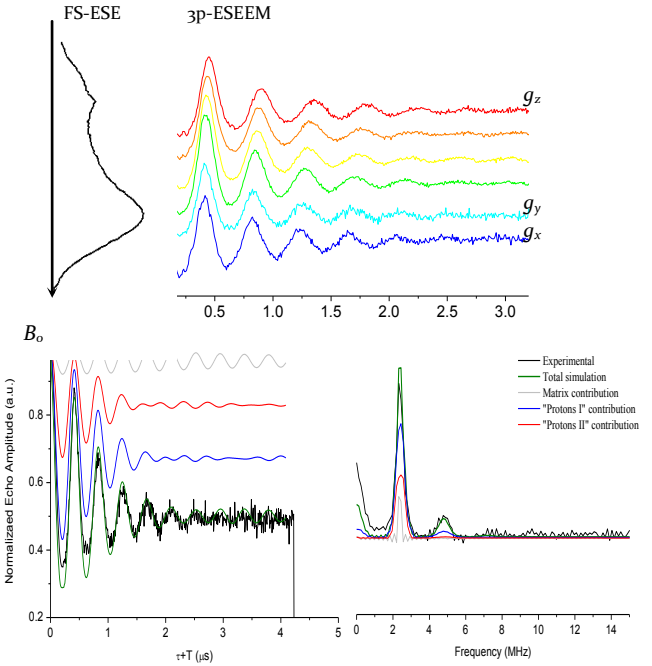

FIGURE 3.16 3P-ESEEM TRACES AND CORRESPONDING SIMULATION OF REDUCED HYDF PROTEIN FROM ***Tn***. TOP PANEL: 3P-ESEEM TIME TRACE DEPENDENCE ON THE EXTERNAL MAGNETIC FIELD WHEN SWEPT FROM g_z TO g_x. BOTTOM PANEL: SIMULATION OF THE TIME (LEFT) AND FREQUENCY (RIGHT) DOMAINS OF THE 3P-ESEEM SPECTRUM COLLECTED AT A FIELD POSITION CORRESPONDING TO g_y. DIFFERENT CONTRIBUTIONS ARE HIGHLIGHTED WITH DIFFERENT COLORS.

TABLE 3.2 SIMULATION PARAMETERS OF THE HYSCORE AND ESEEM SPECTRA FOR THE WT $HydF_{T.N.}$ PROTEIN: HYPERFINE COUPLINGS, DISTANCE AND NUMBER OF PROTONS.

	a_{iso} (MHz)	T (MHz)	Distance* (Å)	N° of protons (from ESEEM)
Ridge *I*	0	3.0±0.5	2.5-3.5	2
Ridge *II*	3.5±0.1	5.0±0.5	2.1-3.0	1
Ridge *III*	Total hyperfine interaction: 15±1 MHz			--
Ridge *IV*	0	2.5±0.5	2.8-3.8	--

* Distances have been calculated using the point dipole approximation.

ASSIGNMENT OF EXCHANGEABLE AND NON-EXCHANGEABLE PROTONS

From the HYSCORE and 3p-ESEEM investigation on the reduced $HydF_{Tn}$ protein previously described, a new description of the proton environment of the [4Fe4S] cluster is emerging. It has been demonstrated that this cluster has a peculiar incomplete cysteinyl coordination with three coordinating cysteines residues and a non nitrogen-based, non-protein, fourth ligand. Two distinct sets of interacting exchangeable protons sets has been identified in close proximity to the cluster (protons I and II), both characterized by an easy exchange with deuterium and a geometry which appears to be very labile, as demonstrated by the complete lacking of orientation selection in both HYSCORE and ESEEM. These evidences suggest that these protons belong to a very flexible coordinated molecule or, more realistically, to a small molecule which is free to access the cluster and characterized by a very low rotational energetic barrier when in close proximity to it.

More in detail, the single proton belonging to set II appears to be very close to the cluster, with an Fe-H estimated distance estimated of 2.1-3.0 Å which implies that it is directly bonded to the electron-donor atom/ion coordinating the cluster in its fourth position. The strong isotropic component of the hyperfine interaction indicates a significant extension of the cluster wavefunction on the coordinated molecule suggesting that only two or three bonds separate proton II from the edge of the cluster. Excluding any coordination by proximal aminoacidic residues, experimental results favor the hypothesis that the fourth ligand can be a small organic sulfide as is the case of glutaredoxins [69-73], or an hydroxyl ion, like the aconitase and the dihydroxy-acid dehydratase cases [74, 75] for which similar values of hyperfine interaction has been determined [76]. A tentative model of the [4Fe4S] cluster for HydF from *Tn,* as obtained from spectroscopic data and in the hypothesis that the fourth ligand is a free hydroxyl ion, is reported in figure 3.17.

Protons belonging to set I are characterized by a smaller dipolar interaction compared to set II, which corresponds to a longer Fe-H distance. Many residues in close proximity to the cluster possess relatively acidic protons particularly prone to deuterium exchange. Since ridge I has been demonstrated to be insensitive to site-directed mutagenesis of the nearest oxygen-bearing residues E300, D310, D337 and Y380, the assignment moves tentatively to the two histidine residues, H304 and H352, which could play a peculiar role in the coordination of the cluster also in *Thermotoga neapolitana*.

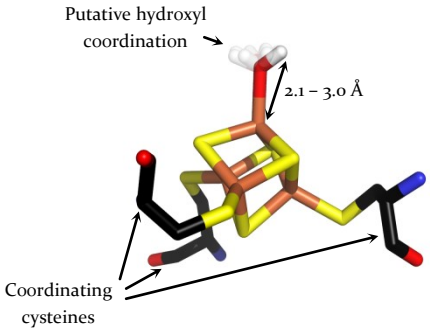

FIGURE 3.17 TENTATIVE MODEL OF THE [4FE4S] COORDINATION SURROUNDING IN HYDF FROM ***Tn*** AS INFERRED FROM EPR SPECTROSCOPY.

Non exchangeable protons, giving rise to ridge III in the HYSCORE spectra, are characterized by high value of the hyperfine interaction parameters and a complete insensitivity to the explored site-directed mutations. The not well-defined ridges prevent the disentangling of the isotropic and dipolar terms of the hyperfine interaction and the consequent evaluation of the distance from the cluster edge. Nevertheless, comparison with literature data allows to reasonably assign these signals to the methylenic protons of the coordinating cysteines.

The non exchangeable protons belonging to set number IV are characterized by small dipolar hyperfine interaction and a null isotropic interaction, corresponding to a Fe-H distance ranging from 2.8 to 3.8 Å. This evidence suggests that these protons can be assigned tentatively to the protein backbone or to some residues near the cluster, but their identity is still controversial.

3.5 Conclusions and future perspectives

In conclusion, this work has provided a key insight into the coordination surrounding of the [4Fe4S] cluster of the maturase protein HydF from two different organisms, *i.e. Clostridium acetobutylicum* and *Thermotoga neapolitana*. The crucial point is the interchangeability of the fourth non-cysteinyl ligand in distinct organisms which suggests a pivotal role of this coordination position in fine tuning the whole maturation process. Moreover, the non-protein coordination discovered in the $HydF_{Tn}$ is very interesting since only few such cases are reported in the literature [69-73]. If the hypothesis of an hydroxyl coordination holds, the coordination of the [4Fe4S] cluster in HydF from *Thermotoga neapolitana* would be peculiar since to date only the aconitase enzyme possesses an iron-sulfur cluster ligated by a water/hydroxyl moiety, which is crucial for the entire catalytic process.

Further spectroscopic investigations based on $H_2{}^{17}O$ exchange are in progress to directly measure the oxygen coordination of the hydroxyl to the iron ion and to confirm this hypothesis. The final aim is to draw an overall picture on how the complex H-cluster is assembled and transferred into the *apo*-HydA protein by the HydF maturation protein.

CHAPTER 4

A COMPARATIVE INVESTIGATION ON THE PROTON ENVIRONMENT OF THE PHOTOPROTECTIVE SITE IN PCP ANTENNA COMPLEXES BY MEANS OF PHOTOEXCITED 3P-ESEEM SPECTROSCOPY

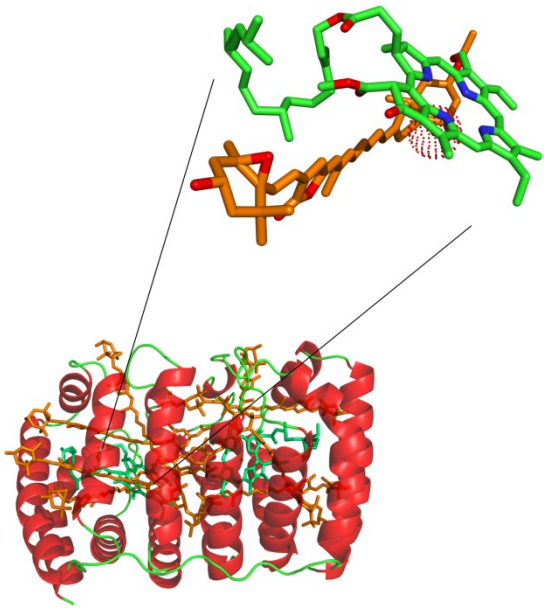

Oxygenic photosynthesis is universally considered the most significant chemical process taking place on Earth. By means of light energy and extremely specialized protein machineries, photosynthetic organisms are able to fix carbon from atmospheric carbon dioxide into highly energetic carbohydrates according to the following reaction:

$$nCO_2 + nH_2O \xrightarrow{h\nu} nC(H_2O) + nO_2 \qquad (4.1)$$

Carbohydrates, produced by the photosynthesis, represent up to now the final energetic source which has been most exploited by mankind, in earlier times in the form of wood and then of carbon, fat and oil which are direct derivatives of animal and vegetal carbohydrates. Moreover, the by-product of the reaction, *i.e.* molecular oxygen, has allowed the development of life on the Earth as it is, permitting the evolution of higher animal species based on an oxygenic metabolism and thus closing the redox cycle started by photosynthetic organisms as illustrated in figure 4.1.

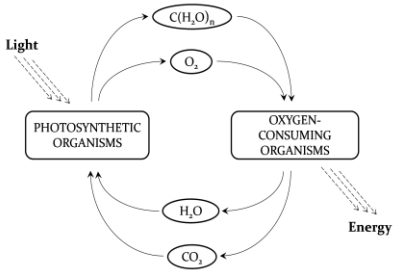

FIGURE 4.1 SCHEMATIC REPRESENTATION OF THE CYCLE OF CARBOHYDRATES THAT CONVERTS THE LIGHT ENERGY INTO CHEMICAL ENERGY FOR THE BIOSYNTHESIS OF COMPLEX ORGANIC MOLECULES IN HETEROTROPHS.

Photosynthesis is performed by several different species of bacteria, algae and plants but the whole process follows a similar scheme in which energy from light is absorbed by peculiar proteins named *light harvesting complexes* (LHC) or *antenna complexes* and then transferred to the *reaction center* where charge separation takes places.

In higher plants the whole light-dependent photosynthetic reaction is summed up in the so-called *Z-scheme*, reported in figure 4.2 and briefly described below. In the reaction centers of photosystem II a chlorophyll molecule (P680) absorbs a photon and releases an electron in a photo-induced charge separation process which is repeated twice. The two electrons are soon transferred (micro- to milliseconds timescale) via an electron transport chain (with consequent chemiosmotic synthesis of ATP) to the photosystem I where they fill the holes left by another double photo-induced charge separation on the P700 chlorophyll pigments. Electrons from P700 chlorophylls, excited by the absorption of light, enter a chain of iron-sulfur electron acceptors that drive electrons to the reduction of $NADP^+$ to NADPH by the $NADP^+$ reductase enzyme. Finally the cycle is closed by the oxidation of a water molecule that provides the electrons to fill the holes of the photosystem II chlorophyll molecules from which the reaction started. These highly energetic molecules are in turn employed in the reduction of carbon dioxide to carbohydrates in a series of reactions that don't need the presence of light and are then commonly referred to as *dark reactions*.

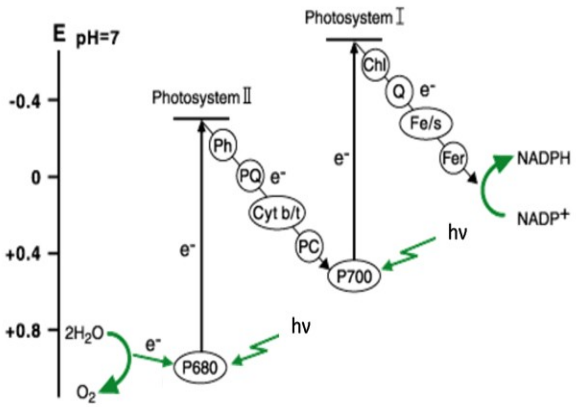

FIGURE 4.2 REPRESENTATION OF THE "Z-SCHEME" OF OXYGENIC PHOTOSYNTHESIS IN THE REDOX POTENTIAL SCALE. LEGEND: ***Ph*** IS PHEOPHITIN, ***PQ*** PLASTOQUINONE, ***Cyt b/t*** CYTOCHROME ***b/t***, ***PC*** PLASTOCYANIN, ***Chl*** CHLOROPHYLL ***Q*** QUINONE, ***Fe/S*** IRON-SULFUR CENTERS, ***Fer*** FERREDOXIN

Photosynthetic organisms have evolved in order to optimize the absorption of energy from light in different environments, ranging from the deepest oceanic hydrothermal vents where the only light available is the faint glow from the black smokers, to the deserts where plants have to fight against extreme aridity and sunlight conditions. Light capture is relied on the already cited light harvesting complexes which consist of a specialized molecular apparatus containing large amounts of photoactive pigments dedicated to the absorption of light and the subsequent transfer and funneling of the energy towards the reaction centers; figure 4.3 illustrates top and side views of LHC*II*, the main light harvesting complex of higher plants.

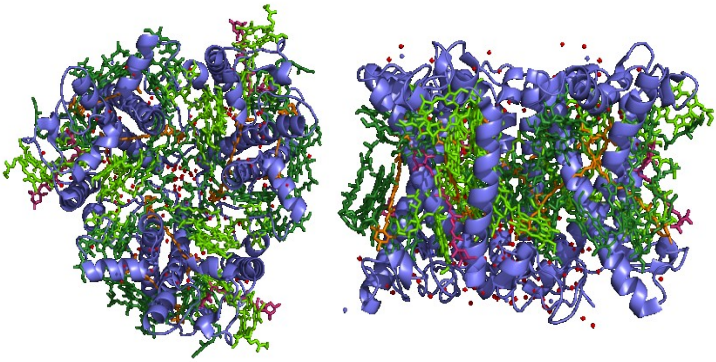

Figure 4.3 Top (left) and side (right) view of LHC*II* from pea (PDB: 4LCZ) [77]. Pigments color code: lutein and neoxanthin carotenoids are in orange and pink respectively, chlorophylls-***b*** are in light green, chlorophylls-***a*** are in dark green.

Despite the high evolution differentiation of LHCs, their pigments can be grouped into only three structural classes as summed up in figure 4.4: chlorophylls and bacteriochlorophylls, carotenoids (carotenes and xanthophylls) and phycobilins [78]. Chlorophylls and bacteriochlorophylls are usually termed as the primary pigments, directly involved in the energy transfer to the reaction centers. Since these molecules possess a peculiar absorption spectrum characterized (with minor deviations) by two main absorption bands, called B and Q bands, in the UV-blue and in the red regions of the spectrum, they are regularly accompanied by accessory pigments like carotenoids and phycobilins. Accessory pigments work absorbing light in the central region of the solar spectrum between 450 and 550 nm, where chlorophylls are almost inactive chromophores, and transferring energy to the chlorophylls themselves in a process called *singlet-singlet energy transfer*, thus optimizing the absorption of energy from the sun.

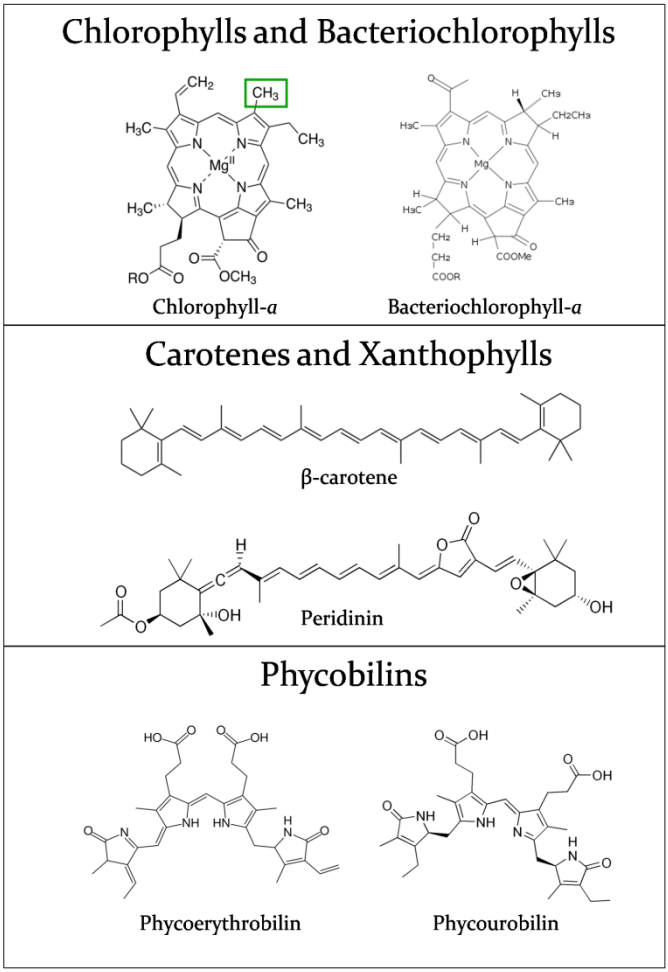

FIGURE 4.4 CHEMICAL STRUCTURE OF SOME REPRESENTATIVE MOLECULES OF THE THREE CLASSES OF PHOTOSYNTHETIC PIGMENTS FOUND IN LIGHT HARVESTING COMPLEXES.

Carotenoids have another pivotal role inside LHCs other than accessory pigments that is the photoprotective function. Photosynthesis is an intrinsically inefficient process, being only 3-6% (11% theoretical) of the incident radiant energy effectively converted into chemical energy [79]. Energy losses are mainly due to the restricted spectral active range (400-700 nm) of photosystems, the incomplete absorption of incident light, the degradation of higher energy photons to bio-available 680 and 700 nm photons and the energy loss during the synthesis of carbohydrates. All the excess of light energy must be promptly dissipated by the photosynthetic machinery to avoid damaging of the apparatus. More in detail the excess of incident photons can cause a large fraction of the chlorophyll molecules to be excited to their triplet state, becoming powerful oxygen sensitizers. Carotenoids are capable of quickly scavenging the triplet state of chlorophylls via *triplet-triplet energy transfer* (TTET), since their triplet state usually lies lower in energy compared to the chlorophyll triplet state and also to the oxygen singlet state, as depicted in figure 4.5. As already discussed in chapter 1, this mechanism allows to transfer the triplet state excitation from the chlorophyll (the donor) to the carotenoid (the acceptor) in a tenth of nanoseconds timescale. Since TTET takes place in a spin conservation frame, because of the peculiar mechanism described in section 1.5, the polarization of the carotenoid triplet state reflects the polarization of the donor and the relative geometry of the pigment pair. In this sense EPR spectroscopy, specifically in its time-resolved variant, has revealed to be a powerful tool to investigate pigment

geometry and energy pathways in the photosynthetic apparatus [80-83].

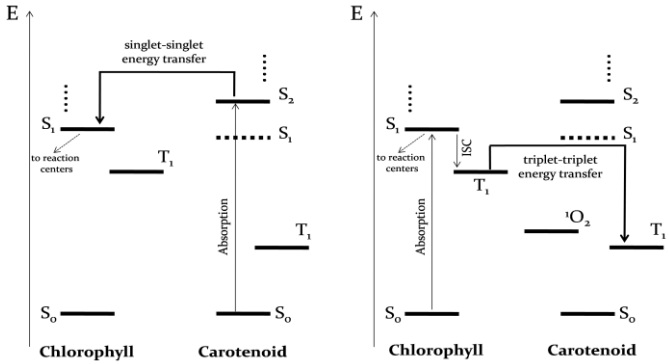

FIGURE 4.5 SCHEME OF THE ELECTRONIC LEVELS REPRESENTING THE PRINCIPAL PATHWAYS OF SINGLET-SINGLET ENERGY TRANSFER (LEFT PANEL) BY WHICH CAROTENOIDS ACT AS ACCESSORY PIGMENTS, AND OF TRIPLET-TRIPLET ENERGY TRANSFER (RIGHT PANEL) BY WHICH CAROTENOIDS SCAVENGE THE CHLOROPHYLLS TRIPLET STATE.

4.1 THE PCP ANTENNA COMPLEX

The peridinin-chlorophyll *a*-protein (PCP) is the main antenna complex of many photosynthetic dinoflagellate marine organisms. It is a water-soluble antenna complex and it is characterized by an unusually large carotenoid (peridinin) to chlorophyll *a* ratio (4:1), which ensures an optimal absorption of the green-blue light (470 to 550 nm). The singlet-singlet energy transfer yield almost reaches unity, making PCP a perfectly evolved protein machinery for the absorption of light beneath the sea level.

The crystal structure of the most common, water soluble Main Form PCP (MFPCP) from the dinoflagellate *Amphidinium carterae* (*Ac*) has been solved at a resolution of 2.0 Å [84]. The protein crystallizes as a homotrimer; every monomer subunit is characterized by a pseudo-c_2 symmetry between the N- and C-terminus domains each containing a chlorophyll *a* molecule surrounded by four peridinin molecules in van der Waals contact with the tetrapyrrole ring. As a result every PCP monomer contains two chlorophylls *a* and eight peridinins arranged in a pseudo-$c_2$symmetry as illustrated in figure 4.6.

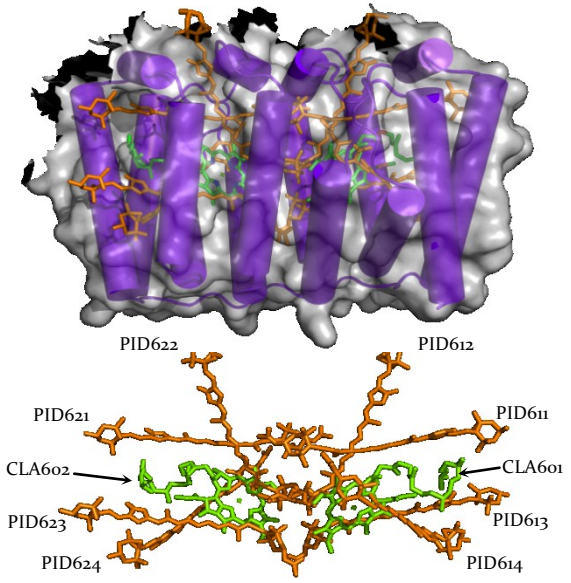

FIGURE 4.6 TOP PANEL: CARTOON REPRESENTATION OF THE MONOMER OF MFPCP PROTEIN FROM ***Ac*** (PDB ENTRY: 1PPR) [84]. PERIDININS AND CHLOROPHYLLS PIGMENTS ARE BURIED IN A HYDROPHOBIC POCKET. BOTTOM PANEL: SPATIAL ORGANIZATION OF PIGMENTS WITH RELATIVE NOMENCLATURE AS INTRODUCED BY HOFMANN [84].

Along with the MFPCP, a minor component has also been reported which is eluted from an anion exchange column at high salt concentration [85]. This form of PCP is called High Salt PCP (HSPCP) and, despite the fact that it shares only 31% of primary structure homology with MFPCP, the pigments arrangement is surprisingly similar among the two proteins as determined from the crystal structure solved by Schulte and coworkers (Brookhaven Protein Data Bank entry: 2C9E) [86]. The main difference is the lack in the HSPCP of a pair of symmetry related peridinins called PID612 and PID622.

The TTET photoprotective pathway has been extensively studied in PCP by means of advanced optical [87, 88] and EPR [81, 82, 89-91] spectroscopies. More in detail time-resolved EPR, together with spectral simulation, allowed the identification of two specific chlorophyll triplet quenching paths each involving a precise peridinin molecule: CLA601-PID614 and the pseudo-symmetry related CLA602-PID624 [82]. The unique feature that characterizes these pairs of pigments is the presence of a water molecule located between the chlorophyll and the peridinin molecules. This water molecule is coordinated to the Mg atom of chlorophyll and hydrogen bonded to the histidine H66(H229) residue. TTET relies on the overlap between the wavefunctions of the donor and the acceptor since, as already introduced in chapter 1, according to the Dexter's model it can be considered a simultaneous double electron transfer. Recently, photoexcited ESEEM spectroscopy combined with D_2O exchange and supported by DFT calculations demonstrated that the interfacial water molecule found in PCP is integral part

of the entire photoprotective system, along with chlorophyll *a* and peridinin, providing a bridge for the wavefunctions of the two pigments involved in TTET [92]. In this work, 2p- and 3p-ESEEM traces of untreated and D_2O-exchanged MFPCP have been collected at several external magnetic fields in order to account for orientation selection. At the same time a multi-level DFT geometry optimization has been performed to define the spatial orientation and the full set of hyperfine interaction tensors of the peridinin triplet state including the two non-equivalent water protons, absent in the X-ray crystal structure. These data have been employed as starting points for the numerical simulation of the ESEEM traces leading to a remarkable final agreement between experimental and calculated traces, providing the hyperfine tensor information and demonstrating, through the EPR parameters, the crucial role of the structured water molecule in the photoprotective system.

In this thesis, the same approach described for the MFPCP has been applied to the photoprotective sites of HSPCP from *Ac* and to the PCP antenna complex of a different organism, *Heterocapsa pygmaea* (*Hp*), whose crystal structure also has been solved [93]. Despite the 30% sequence homology both the light harvesting complexes investigated shares a common-featured photoprotective site as illustrated in figure 4.7, with a water molecule located at the interface between the pair of pigments involved in the TTET process, suggesting a key role for the conserved water in the photoprotective mechanism of different PCP forms.

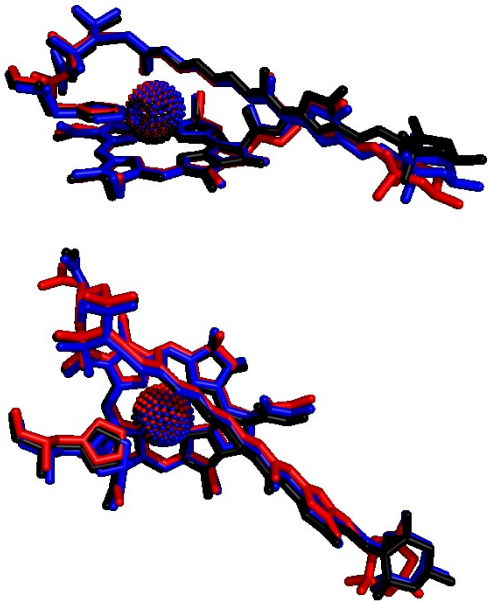

Figure 4.7 Comparison of the structure of the photoprotective sites in MFPCP (black), HSPCP (red) and PCP from ***Hp*** (blue) as determined by X-ray crystallography [84, 86, 93]. Steric hindrance of the water molecule is represented by a dotted sphere, the phytol side chain of chlorophylls are omitted for clarity

4.2 3P-ESEEM spectroscopy on different forms of PCP antenna complex

As discussed in chapter 2, the time-resolved or FS-ESE spectrum of a photoexcited triplet state gives information on the polarization of the triplet state, by simulation of the characteristic intensity pattern, with

emission lines accompanying enhanced absorption features, and about the *Zero Field Splitting* parameters from the field position of the six turning points. The FS-ESE spectra of HSPCP and PCP from *Hp* recorded at 20 K and a DAF of 50 ns are reported in figure 4.8; identical spectra has been obtained for the D_2O-exchanged samples. For the detailed experimental conditions see appendix A.1. As can be immediately noted, they closely resemble that of MFPCP, which has already been simulated considering the triplet state localized on the photoprotective peridinins PID614(624) [81], underlining the already discussed strong similarities in the photoprotective sites between the different PCP forms as obtained from X-Ray crystallography.

Photoexcited 3p-ESEEM has been performed at three different values of the external magnetic field corresponding to the three low-field canonical transitions Z^- (300 mT), Y^+ (314 mT) and X^+ (326.5 mT). Following the procedure proposed by Mims [68], 3p-ESEEM traces have been collected both for the untreated and the D_2O-exchanged samples and then the quotient envelope trace $^{D_2O}/_{H_2O}$ has been calculated in order to remove from the deuterium-exchanged trace the contribution of unexchangeable protons and consequently keeping modulations due only to the effectively exchanged protons, as exemplified in figure 4.8. Quotient time traces collected at the three canonical transitions for the two antenna complexes under investigation and the relative frequency domain spectra (obtained via cosine Fourier transformation) are

reported in figure 4.9 in red and blue together with the main form PCP from Ac.

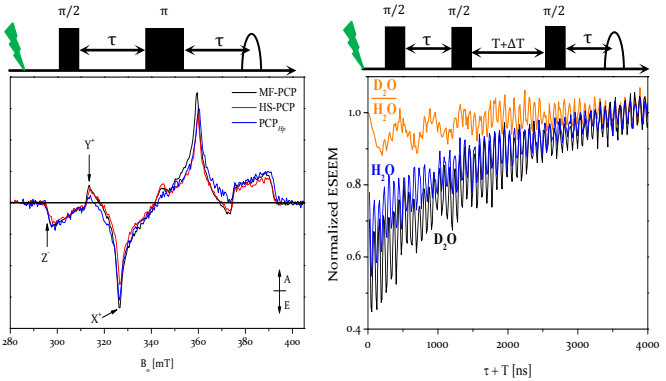

FIGURE 4.8 LEFT PANEL: LOW-TEMPERATURE PHOTOEXCITED FS-ESE SPECTRA OF HSPCP AND PCP FROM HP AND COMPARISON WITH MFPCP FROM AC(COLOR CODE AS IN FIGURE 4.7). ARROWS INDICATE THE FIELD POSITIONS AT WHICH ESEEM TRACES HAVE BEEN COLLECTED. RIGHT PANEL: ESEEM TIME TRACES COLLECTED AT THE X^+ POSITION FOR THE UNTREATED (BLUE TRACE) AND D_2O-EXCHANGED (BLACK TRACE) PCP FROM ***Hp*** TOGETHER WITH NORMALIZED DEAD-TIME RECONSTRUCTED QUOTIENT TRACE (ORANGE). THE ORDINATE SCALE REFERS ONLY TO THE QUOTIENT TRACE.

The comparison with the corresponding traces for the MFPCP complex (black traces, [92]) reveals strong similarities among the different PCP complexes investigated. Deep and slow modulations due to coupled deuterons characterize all the 3p-ESEEM traces collected in correspondence of the X^+ and Y^+ canonical transitions (see fig. 4.8 for the definition of the transition). As a preliminary analysis of the frequency domain spectra suggests, modulation frequencies in the 2 MHz region of the spectra appear quite the same among the three PCP

complexes here compared, with a slight difference that can be noted only in correspondence of the Y^+ transition, where MFPCP appears modulated at a slightly higher frequency (difference < 0.5 MHz).

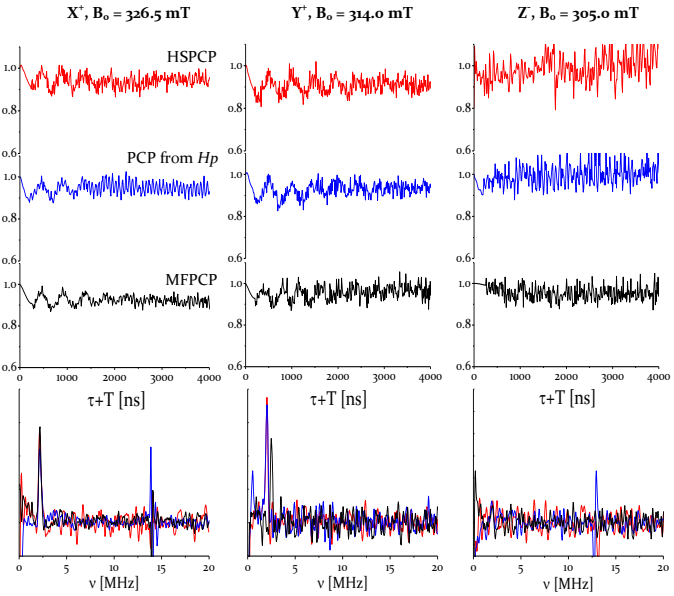

FIGURE 4.9 3P-ESEEM QUOTIENT TRACES COLLECTED AT THE THREE CANONICAL ORIENTATIONS OF THE ZFS TENSOR FOR HSPCP (RED TRACE) AND FOR PCP FROM ***Hp*** (BLUE TRACE)AND COMPARISON WITH THE TRACES FOR MFPCP (BLACK TRACE) [92]. TIME TRACES ARE REPORTED IN TOP PANELS, CORRESPONDING FREQUENCY DOMAIN SPECTRA IN BOTTOM PANELS.

Dispersion signals in the 15 MHz region are indicative of some residual modulation due to unexchanged protons due to an incomplete deletion of the proton contribution by the envelope division procedure. Traces collected at the Z^- magnetic field position appear free of any modulation in the low frequency region, again in complete analogy with the published data for MFPCP.

This specific and characteristic behavior of the 3p-ESEEM trace can be easily addressed to a strong and well-defined orientation selection due to the large anisotropy of the dipolar interaction between electrons in the peridinin triplet state compared to the pulse bandwidth of 3p-ESEEM. According to this effect only a small fraction of the peridinin molecules characterized by a precise orientation of the ZFS tensor (and thus of the hyperfine tensor) with respect to the external magnetic field is selectively excited in every single experiment performed in correspondence of the ZFS turning points. The strong orientation selection distinctive of the ESEEM spectroscopy applied to the peridinin triplet state is outlined in figure 4.10. Here the effect of a typical $\pi/2$ pulse of 16 ns applied at different values of the external magnetic field is represented in terms of orientation selection for the excited molecules. It can be seen immediately that performing a 3p-ESEEM at different values of the external magnetic field is selective in terms of orientations of the peridinin molecule with respect to the external magnetic field.

The strong orientation selection observed in the collected ESEEM traces indicates that deuterons giving rise to the modulations have a structurally defined arrangement, as in the case of the easily exchangeable protons of a water molecule coordinated to the chlorophyll pigment and engaged in a hydrogen bond network. Moreover, the absence of sum combination peaks in the frequency domain spectra at about twice the Larmor frequency of deuterium suggests that only a limited number of deuterons contributes to the trace [16].

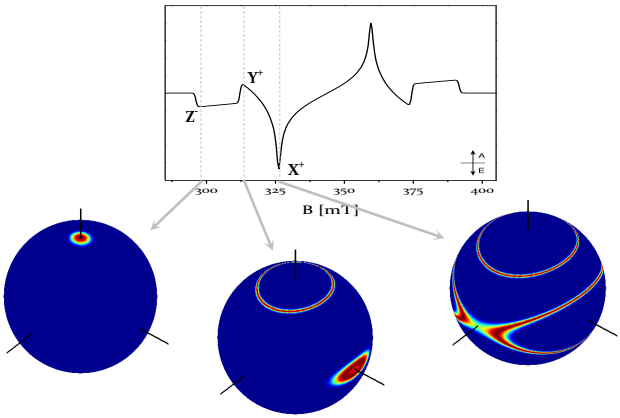

Figure 4.10 Calculated powder EPR spectrum for a triplet state with ZFS and population parameters corresponding to the peridinin triplet state in PCP. The weights of the orientations contributing to the spectrum at the canonical positions X^+, Y^+ and Z^- are plotted on a unitary sphere, redder shades corresponds to higher weights while blue areas indicate orientations that don't contribute to the spectrum.

4.3 Combined ESEEM and computational investigation on the geometry of the photo-protective site and on the hyperfine interaction parameters of the peridinin triplet state

As a good starting point for the simulation of the ESEEM modulations previously introduced, an initial set of hyperfine tensor parameters of the peridinin triplet state

have to be determined. For this reason the correct geometry of the photoprotective site has to be determined.

Despite the crystal structures of both the investigated PCP complexes have been solved at high resolution, showing large similarities between PCP from different organisms, they suffer some limitations and geometry optimization is needed in order to calculate the hyperfine interaction tensors. First of all the crystal structures are solved in a static protein environment that is far away from the physiological medium while at the same time protein concentration is orders of magnitude larger than it is in physiological conditions; these evidences set some cautions regarding the fine positioning of the pigments in PCPs, which are expected to experience some distortions induced by the crystallization conditions. Moreover crystal structures lack information about protons, and therefore also about those belonging to the water molecule, whose orientation with respect to the TTET partners and to the coordinating histidine residue is of primary interest for an accurate simulation of 3p-ESEEM traces. Since magnetic spectroscopy interactions are highly sensitive to the molecular structure it clearly turns out that great care has to be addressed to the fine determination of the geometry of the photoprotective site in the PCP antenna complexes.

Following the same approach described in [92], ONIOM calculations at a B3LYP/6-13G(d):UFF level were performed in collaboration with Dr. Laura Orian (Department of Chemical Sciences, university of Padova)

and Dr. Claudia Tait (Center for Advanced Electron Spin Resonance, Oxford university) in order to take into account the effect of the protein environment on the geometry of the photoprotective site. In the ONIOM approach the inner layer constituted by the two TTET partners peridinin and chlorophyll *a*, the interposed water molecule and the histidine involved in the hydrogen bond with the water molecule itself has been described at a B3LYP/6-13G(d):UFF level; the outer layer, which includes all the residues located at a distance of 4 Å from the atoms of the peridinin and chlorophyll *a* molecules, has been treated at molecular mechanics level.

The reliability of the ONIOM optimization has been tested by computing the EPR spectrum of the peridinin triplet state, whose specific polarization pattern depends on the geometry of the photoprotective site, and comparing it to the experimental one; corresponding results are reported in figure 4.11.

Triplet state spectra can be calculated in the TTET frame and depend on the polarization of the donor and the relative geometry of the pigments involved, according to the spin projection formula (1.28) presented in chapter 1. The polarization pattern of the donor chlorophyll *a* employed in the simulation of time-resolved EPR spectra of MFPCP has already been published [82]; in the following calculation of the FS-ESE spectra of HSPCP and PCP from *Hp* the same pattern P_x=0.37, P_y=0.41, P_z=0.22 has been employed. The orientation of the ZFS axis with respect to the molecular frame of donor and

acceptor is of primary significance in the determination of the matrix of squared cosines of eq. (1.28).

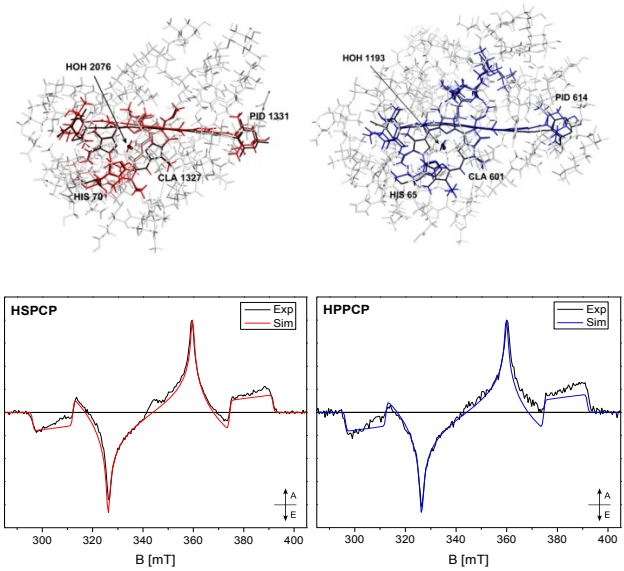

Figure 4.11 Top panel: Comparison between the X-ray structures (black) and the B3LYP/6-31G(d):UFF optimized structures (color) for HSPCP and PCP from ***Hp***. Amino acids included in the outer ONIOM layer are grey-colored. Bottom panel: Comparison between the experimental photoexcited FS-ESE spectra of HSPCP and PCP from ***Hp*** recorded at 20 K(black traces) and the calculated spectra calculated from the relative orientation of chlorophyll ***a*** and peridinin obtained from geometry optimization (colored trace).

While the ZFS axis orientation with respect to the optical axis for chlorophyll *a* has been already determined [94, 95], no data are currently available for peridinin. Orientation of the ZFS tensor thus has been calculated by means of the principal components

analysis which is a statistical interpolation of the atoms bearing triplet spin density on peridinin [80]. D and E parameters for peridinin have been taken from literature [81]. More details are reported in Appendix A.1.

Triplet state spectra are very sensitive to the polarization pattern of the triplet state, which in the TTET frame depends on the polarization of the donor and the relative geometry of the pigments involved, according to the spin projection formula (1.28) presented in chapter 1. The polarization pattern of the donor chlorophyll *a* employed in the simulation of time-resolved EPR spectra of MFPCP has already been published [82]; in the following calculation of the FS-ESE spectra of HSPCP and PCP from *Hp* the same pattern P_x=0.37, P_y=0.41, P_z=0.22 has been employed. The orientation of the ZFS axis with respect to the molecular frame of donor and acceptor is of primary significance in the determination of the matrix of squared cosines of eq. (1.28). While the ZFS axis orientation with respect to the optical axis for chlorophyll *a* has been already determined [94, 95], no data are currently available for peridinin. Orientation of the ZFS tensor thus has been calculated by means of the principal components analysis which is a statistical interpolation of the atoms bearing triplet spin density on peridinin[80]. As a rule of thumb oblate spin distribution like that of chlorophylls are characterized by a Z axis perpendicular to the plane while prolate distributions like that of polyenes shows a Z axis parallel to the principal axis of the distribution. D and E parameters for peridinin have been taken from literature [81].

ONIOM optimized structures exhibit minor variation compared to the relative X-Ray structures, as can be evaluated from figure 4.12, where the comparison between the structure of the photoprotective sites is shown with superimposed chlorophyll rings. The most remarkable outcome of the geometry optimization regards the orientation of the interposed water molecule, HOH2076 in HSPCP and HOH1193 in PCP_{Hp}, respectively. The oxygen atom is in both cases 2.1 Å away from the Mg^{2+} ion at the center of the tetrapyrrole ring, confirming its coordinative function as compared with typical Mg^{2+}-O distances in water-coordinated porphyrins [96]. One of the two water protons points toward the τ nitrogen of the proximal histidine residue at a distance of 1.7 Å suggesting it is involved in a hydrogen-bond network. The second proton points toward the conjugated chain of peridinin, with a shortest H-$^{\pi}$C distance of 2.5 Å for HSPCP and 2.7Å for PCP_{Hp} respectively. A detailed representation of the geometry-optimized photoprotective sites is reported in figure 4.12.

Density Functional Theory (DFT) calculations of the triplet spin density, at a B3LYP/EPR-II-6-31G(d,p) level, has been performed for the chlorophyll-HOH-peridinin system in HSPCP and PCP from *Hp* after geometry optimization. Mapping of the spin density on the single atoms of the peridinin and water is reported in table 4.1 for all the PCP forms. Interestingly a small but significant spin density has been found on the oxygen atom of the interposed water, supporting the hypothesis that the water molecule is a conserved element of the photoprotective site in different PCP antenna complexes.

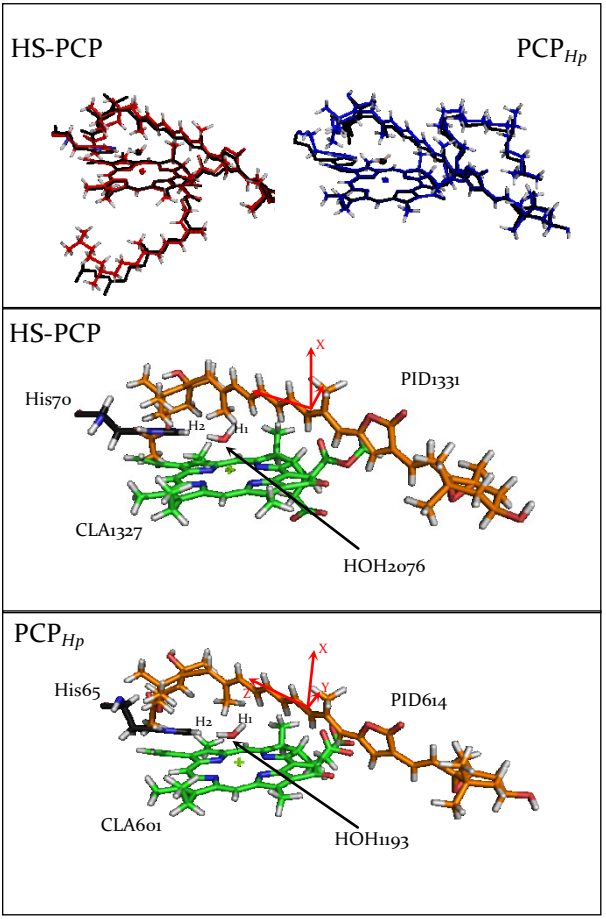

Figure 4.12 Top panel: comparison between crystal structures (black) and B3LYP/6-31G(d):UFF optimized structures for the HSPCP (red) and PCP from ***Hp*** (blue). Bottom panels: detailed representation of the optimized structures of the photoprotective sites of HSPCP and PCP from ***Hp***. ZFS tensor orientation calculated for peridinin are reported in red arrows. Phytol tails of chlorophylls have been removed for clarity.

TABLE 4.1 MULLIKEN SPIN DENSITIES OF SELECTED ATOMS ON THE SYSTEM CONSTITUTED BY THE CONJUGATED CHAIN OF PERIDININ AND THE WATER MOLECULE LOCATED IN THE PHOTOPROTECTIVE SITE, FOR ALL THE PCP FORMS

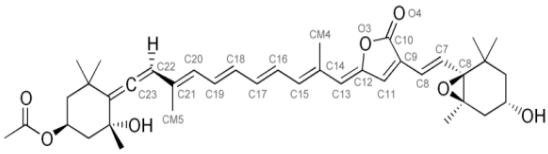

Atom	Triplet spin density, HSPCP[(a)]	Triplet spin density, PCP_{Hp}[(a)]	Triplet spin density, MFPCP[(a, b)]
C1	0.014	0.016	0.016
C6	-0.016	-0.017	-0.017
C7	0.197	0.196	0.202
C8	-0.089	-0.089	-0.093
C9	0.238	0.235	0.242
C10	0.020	0.019	0.016
C11	-0.039	-0.041	-0.048
C12	0.248	0.246	0.257
C14	0.236	0.239	0.228
C15	0.161	0.152	0.191
C16	0.081	0.088	0.065
C17	0.288	0.280	0.300
C18	-0.063	-0.056	-0.076
C19	0.333	0.334	0.334
C20	-0.122	-0.121	-0.131
C21	0.303	0.308	0.300
C22	-0.095	-0.101	-0.099
C23	0.206	0.223	0.208
C24	-0.035	-0.036	-0.038
CM4	-0.016	-0.016	-0.015
CM5	-0.022	-0.021	-0.022
O3	0.131	0.129	0.135
O(H_2O)	0.002	0.002	0.002

(a) For peridinin only spin densities larger than 0.015 have been included in the table

(b) Data for MFPCP taken from [92]

DFT calculations hyperfine interaction tensors have also been calculated for the two protons of the interposed water molecule at a B3LYP/EPR-II-6-31G(d,p) level of theory. Not only the hyperfine couplings, but also the orientation of the hyperfine tensor of each proton with respect to the peridinin ZFS frame is required for a correct simulation of the 3p-ESEEM traces in order to properly describe both the modulation frequency and the strong orientation selection observed. Details on all the DFT calculations are reported in appendix A.1.

Hyperfine tensor values expressed in terms of principal values and orientation with respect to the ZFS frame of the peridinin (Euler angles), as obtained from DFT computations, are reported in table 4.2 and compared to the corresponding values obtained for MFPCP. As it can be immediately inferred from these parameters, the two protons are far from being equivalent, which is a direct consequence of the structured frame in which the water molecule is located. A significant isotropic component has been obtained for both the water protons, larger on proton H1 which points towards the conjugated chain of peridinin, where the triplet state is mainly located. This remarkable result, together with the non-zero triplet spin density found at the oxygen atom of water, can confirm the key role of water in actively linking the two partners of TTET if the hyperfine tensors here obtained from the calculations is validated by the experimental 3p-ESEEM traces.

TABLE 4.2 HYPERFINE PARAMETERS FOR THE TWO PROTONS OF THE WATER MOLECULE, OBTAINED BY DFT CALCULATIONS, FOR ALL THE FORMS OF PCP.

	HSPCP		**PCP$_{Hp}$**		**MFPCP**[(a)]	
	H1	H2	H1	H2	H1	H2
A_{xx} (MHz)	-1.65	0.61	-1.38	0.57	-1.85	0.70
A_{yy} (MHz)	1.98	-0.45	1.43	-0.46	1.78	-0.61
A_{zz} (MHz)	-0.33	-0.16	-0.05	-0.11	0.07	-0.10
a_{iso} (MHz)	-0.43	-0.06	-0.22	-0.04	-0.43	-0.10
α	-69	-135	-114	-128	130	50
β	3	12	8	11	6	20
γ	24	17	71	12	-170	20

[(a)] Data for MFPCP taken from [92]

4.4 ESEEM DATA ANALYSIS AND SIMULATION

The complete numerical simulation of a set of 3p-ESEEM traces collected at several magnetic fields is undoubtedly a hard task. The modulation frequency and depth, the ordinate offset of the time trace, the width and number of peaks in the frequency domain spectrum and the orientation selection are all features of the experimental trace that must be contemporarily reproduced during the simulation. A set of parameters regarding the system under investigation and the major magnetic interactions have to be introduced and fine-tuned to reach a proper and fully-reliable simulation. When correctly performed, the simulation of 3p-ESEEM traces returns the complete description of the paramagnetic center and its magnetic environment.

All the exchangeable protons in proximity to the photoprotective site are expected to contribute to the

quotient ESEEM trace. These protons can be grouped into three separate classes:

- The exchangeable protons of the protein, of the pigments other than the photoprotective peridinin and of generic water molecules (globally referred to as matrix protons);
- The exchangeable protons of the photoprotective peridinin molecule;
- The two exchangeable protons of the water interfaced between the chlorophyll and peridinin molecules involved in TTET.

The contribution from exchangeable matrix protons has been taken into account considering all the exchangeable protons in proximity to the peridinin triplet state other than those of the peridinin itself and of interfaced water, employing an improved spherical model simulation [16]. Because of the elongated shape of the peridinin molecule and consequently of the spin density distribution, matrix protons have been classified and included in a series of subsequent hyperfine isosurfaces rather than concentric spheres calculated in a point dipole approximation. All the protons included between two succeeding hyperfine isosurfaces are considered to randomly contribute to the ESEEM trace with an average hyperfine interaction A_{mid} with axial symmetry, resulting in a hyperfine tensor of the generic form (A_{mid} A_{mid} -2A_{mid}). The arbitrary choice of the axial symmetry of the hyperfine tensor is valid since most of the matrix protons fall outside the 0.01 MHz isosurface and the calculations show that the tensor rhombicity becomes negligible at this level. The 3p-ESEEM

simulation of the matrix protons contribution for the X^+ transition of HSPCP is reported in figure 4.13, (similar results have been obtained for PCP from *Hp*). The resulting modulation depth is far too small with respect to the experimental one, allowing us to unambiguously exclude that the observed modulation comes from exchangeable matrix protons.

The peridinin molecule is characterized by a couple of hydroxyl groups, whose protons, in principle, are exchangeable and can contribute to the 3p-ESEEM trace (see fig. 4.4 for the peridinin molecular structure). As previously described the hyperfine interaction tensors of these two protons have been calculated at the B3LYP/EPR-II-6-31G(d,p) level of theory and the corresponding echo envelope modulation was simulated. The simulation for the X^+ transition of the peridinin triplet state in HSPCP, depicted in figure 4.13, unequivocally excludes a major contribution of the peridinin protons in the 3p-ESEEM modulation (similar results are obtained for PCP from *Hp*).

The initial parameters of the simulation the 3p-ESEEM traces of HSPCP and PCP from *Hp* samples considering the contribution from the interfaced water protons were the set of hyperfine interaction parameters obtained from quantum mechanical calculations summed up in table 4.2. A non-complete agreement between the values reported in the table and those employed for a correct simulation are therefore expected, mainly because of the approximations necessarily introduced during the computation but the refinement is very small proving and validating the accuracy of the calculations. The

experimental modulation depth and frequency are finely reproduced with only slight adjustments of the computed values of the hyperfine interaction parameters as reported in figure 4.13, for the 3p-ESEEM trace corresponding to the X^+ transition of the peridinin triplet state for HSPCP(similar results have been obtained for PCP from *Hp*). The hyperfine tensor orientation does not require any adjustment since the orientation selection, with particular attention to the lack of modulation in correspondence of the Z transition, is well matched. Hyperfine values employed for the simulation of the water protons contribution are summed up in table 4.3.

TABLE 4.3 REFINED HYPERFINE PARAMETERS FOR THE TWO WATER PROTONS H1 AND H2 EMPLOYED FOR THE ESEEM SIMULATION IN FIGURE 4.13 AND 4.14

	HSPCP		**PCP$_{Hp}$**	
	H1	H2	H1	H2
A_{xx} (MHz)	-2.5	0.8	-2.5	0.8
A_{yy} (MHz)	2.5	-0.7	2.5	-0.7
A_{zz} (MHz)	0	-0.1	0	-0.1
a_{iso} (MHz)	-0.4	-0.1	-0.4	-0.1
α	-69	-135	-114	-128
β	3	12	8	11
γ	24	17	71	12

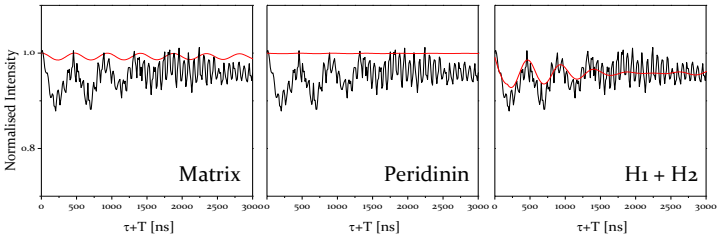

FIGURE 4.13 SIMULATION OF THE 3P-ESEEM QUOTIENT TRACE OF THE PERIDININ TRIPLET STATE AT THE X^+ CANONICAL ORIENTATION OF THE ZFS TENSOR (B_0 = 314 ***mT***)CONSIDERING THE CONTRIBUTIONS OF THE THREE SETS OF EXCHANGEABLE PROTONS IN HSPCP. SIMULATION PARAMETERS ARE REPORTED IN TABLE 4.3.

Although the simulations demonstrate that the major contribution to the ESEEM trace is due to the interfaced water protons and that matrix and peridinin exchangeable protons are not responsible for the deep modulations experimentally observed, they are expected to contribute to the ESEEM trace with a minor contribution. For this reason, a global simulation has been carried out in which the three different contributions previously analyzed have been taken into account, summing the echo envelope modulations according to the product rule [12] for the two investigated system at the three canonical orientations of the ZFS tensor as reported in figure 4.14. The simulations appear in good agreement with the experimental data, although no significant improvement comes from the contribution of the other sets of protons. Modulation frequency, depth and damping are well reproduced and also the strong orientation selection. ESEEM time traces hold information about the number of the interacting nuclei as well, mainly related to the offset of the time trace from zero. Simulations were performed employing two structured deuterons

and adding a definite number of almost negligible deuterons as a further support of the validity of the initial hypothesis that the main contribution comes from the water protons. Indeed two protons are needed for the correct simulation of the ESEEM time traces.

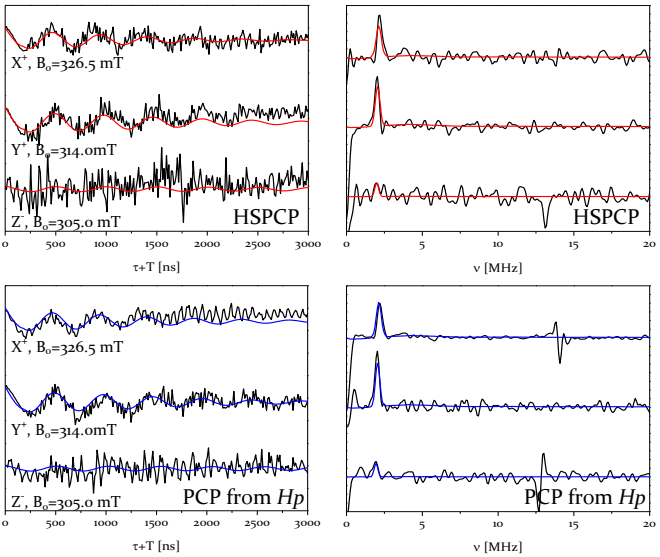

Figure 4.14 Simulation (color traces) of the overall set of experimental 3p-ESEEM traces (in black) for the HSPCP and PCP from *HP*, as obtained combining the three contributions described in the text. Time traces are on the left panels while the corresponding frequency domain spectra are on the right panels. Color code: red HSPCP, blue PCP from ***Hp***.

4.5 Conclusions and future perspectives

This work reinforces the results already published for the PCP antenna complex, which is one of the most investigated light harvesting complex and can be used as a model for the photoprotective strategy in photosynthetic antennas [92]. A structured water molecule has been identified in the x-ray structure, which is interfaced between the photoprotective pair of pigments, namely the chlorophyll *a* and the corresponding photoprotective peridinin. Quantum mechanical calculations combined with simulations of the 3p-ESEEM experiments performed in the presence of D_2O-exchangeunambiguously show that this special water molecule is part of the photoprotective site, which is involved in the TTET process against singlet oxygen formation under high light conditions. TTET can be described as a simultaneous double electron process, whose exponential decay rate dependence on the distance is twice that of the corresponding electron transfer process. The overlap between wavefunctions may become critical at even shorter distances for TTET as compared to electron transfer. For this reason, superexchange models involving a bridge or the medium interposed between the donor and the acceptor molecules, become even more important when describing TTET. Several theoretical and experimental works have demonstrated that water can participate in electron transfer processes as a superexchange bridging molecule [97-101].

The presence of a molecular bridge becomes of primary significance when fast transfers are required in order to preserve the entire photosynthetic machinery.

In this work, the investigation has been extended to other PCP complexes, namely High-Salt PCP from *Ac* and PCP from *Hp*, in order to reinforce the hypothesis n the key role played by the water molecule at the interface between the two pigment involved in photoprotection. By means of hybrid classical quantum mechanical calculations, it has been demonstrated that both the proteins possess a structured water molecule interfaced between the photoprotective pair. DFT calculations reveal that a significant fraction of the triplet spin density is located on the oxygen atom of the interfacing water molecule, as previously observed in the PCP complex from *Ac*. The quantum mechanical approach has allowed to determine the principal values and the orientation of the hyperfine tensors with respect of the ZFS frame of peridinin triplet state. As the orientation of the water molecule is well defined, the hyperfine tensors characterizing the interaction of the water protons (deuterons) with the peridinin triplet state are also well-defined. These results have been employed for the numerical simulation of the quotient 3p-ESEEM traces of the peridinin triplet state, corresponding to D_2O-exchanged conditions, with a surprisingly agreement of the computed with the experimental data. It has been demonstrated that the water molecule, at the interface between the photoprotective pigments, primarily contributes to the ESEEM traces, in complete analogy with the results obtained for PCP from *Ac*.

These results strongly reinforce the hypothesis that this water molecule acts as a conserved and active player in the photoprotective mechanism of the water-soluble PCP antenna complex, confirming the absolute requirement of considering solvent molecules or amino acids at the interface between the two partners when dealing with electron transfer and/or TTET processes.

Further work is in progress on reconstituted PCP complexes in which chlorophyll *a* has been replaced with different pigments, for example bacteriochlorophyll. In this case the refolding process has not prevented the interfacing of the water molecule in the photoprotective site in the presence of different pigments, as demonstrated by x-ray structural determination. If similar results as for natural PCP proteins will be obtained, the evidence that this water molecule is an active component in the photoprotective mechanism operating in the PCP antenna complexes will strengthen even more.

CHAPTER 5

THE PHOTOEXCITED PORPHYRIN TRIPLET STATE AS A NOVEL SPIN LABEL FOR DEER SPECTROSCOPY: A COMPARATIVE INVESTIGATION ON PEPTIDE-BASED MODEL COMPOUNDS

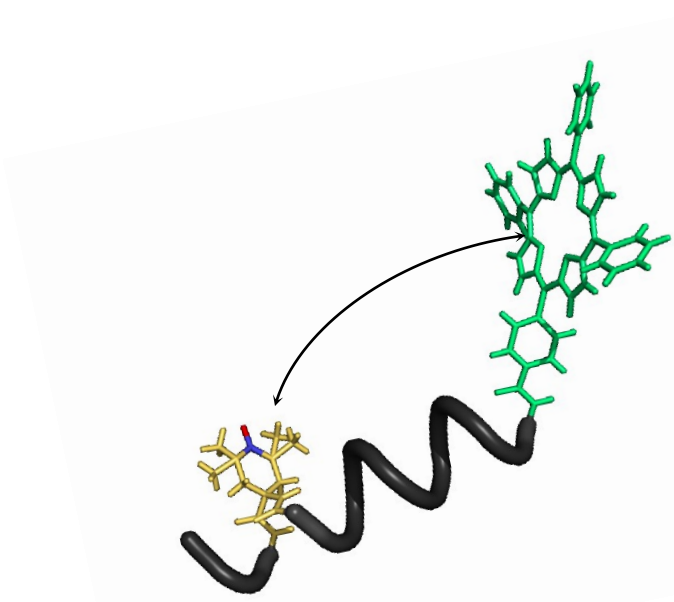

The measurement of intra- and inter-molecular distances in biomolecules for structural investigation has ever been a great challenge. Enzyme activity is often related to sized pockets which allow the enzyme to discriminate different substrates, or to some kind of flexibility in the peptide chain which allows the protein to act as a molecular machines in driving reactions towards the products. The introduction of X-ray crystallography in the early 1900s and its first application to myoglobin in the late 1950s by Kendrew and coworkers [102] has opened an era characterized by the intriguing opportunity of taking pictures of large biomolecules at atomic resolution. Since then the structure of more than 85000 biomolecules has been solved by X-ray crystallography and more than 9000 employing NMR spectroscopy, which allows to solve the structure of relatively small peptides (less than 70 kDa) in solution phase.

Notwithstanding the huge potential of these techniques, they are both affected by great drawbacks mainly regarding the limited size of the macromolecule for the NMR spectroscopy and the essential requirement of obtaining crystals of the molecule for X-ray analysis. Membrane proteins for example often pose great challenges to X-ray crystallography since large amounts of detergents are required to isolate them and this frequently interferes with the crystallization process.

In the last decades the pulse EPR technique Double Electron-Electron Resonance (DEER) has proved to be an effective tool to measure distances in the nanometer range between paramagnetic centers, from 1.5 to 8 nm,

both in natural and synthetic molecules, as confirmed by the astonishing increase of publications regarding DEER spectroscopy. Several dedicated papers and reviews have been recently published on the application of DEER to model compounds, material science and biochemistry [24, 26, 103]. Most commonly (especially in the biological context) DEER spectroscopy is performed between pairs of nitroxide radicals (NO•), but in the last years many efforts have been made to employ other paramagnetic centers characterized by several half-integer spin quantum numbers such as copper ions (Cu^{2+}, S=1/2), gadolinium complexes (Gd^{3+}, S=7/2), low-spin ferric heme (Fe^{3+}, S=1/2) and iron sulfur clusters with variable half-integer total spin quantum number [104-107]. Furthermore, *DeerAnalysis*, a comprehensive software package for data analysis and fitting of DEER experiment on S=1/2 systems has been released for the Matlab® environment since 2004 [108]. On the other hand, no reported data for DEER spectroscopy involving integer spins had been published before the work presented in this thesis. As it was introduced in the previous chapter, integer electron spin quantum states are of fundamental significance in biological systems, in particular in photosynthetic complexes. In this work the feasibility of exploiting photoexcited triplet states as potential probes for DEER spectroscopy will be demonstrated on a series of model compounds and then the application to a biological system, the PCP antenna complex from *Amphidinium carterae* will be discussed.

5.1 Relevant interactions in DEER spectroscopy

As previously introduced in chapter 2, DEER pulse sequence is designed to separate the electron-electron interaction between a pair of coupled electron spins located at a certain distance one from the other. A general electron-electron interaction comes from two distinct physics phenomena described in chapter 1, the classical dipolar coupling (eqq. 1.18 – 1.20) and the quantum mechanical exchange coupling (eq. 1.16, 1.17).

The distance information is usually extracted in a DEER experiment from the dipolar part of the interaction, which is characterized by a relatively simple dependence on the inverse of the third power of the distance between the interacting spins:

$$\omega_{dd} = -\frac{\mu_0 g_1 g_2 \beta_e{}^2}{4\pi\hbar}\frac{1}{r^3}(3\cos^2\vartheta - 1) = \\ = \omega_\perp(3\cos^2\vartheta - 1) \qquad (5.1)$$

in which the dependence of the dipolar coupling on the interspin distance r and the angle ϑ between the interspin vector and the external magnetic field is shown. Since the dipolar coupling falls quickly to zero at large distances, the upper limit of DEER spectroscopy is usually set to 8 nm, despite the detection of dipolar coupling in 6 nm-separated pair of spins is a great experimental challenge itself (for a list of dipolar frequency values for selected distances see table 5.1). When dealing with such distant interacting spins, sufficient resolution is obtained only acquiring at least a time trace with a $\tau_2$delay of 10µs or more [23]. Since the

DEER effect is observed as a modulation of the intensity of the inverted echo generated at time delay τ_2 from the last π pulse, relaxation phenomena (whose fanning out effect on the spin packets cannot be refocused by the π pulses) act for a time $2(\tau_1+\tau_2)$ as illustrated in figure 5.1. This effect limits the detection of very large distances only to a restricted number of systems, characterized by the slowest relaxation rates [109].

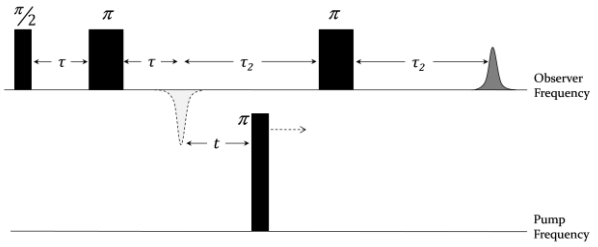

FIGURE 5.1 FOUR-PULSES DEER SEQUENCE. THE OBSERVER SEQUENCE (TOP) IS STATIC: THE τ_2 DELAY IS SET TO THE DESIRED LENGTH OF THE TIME TRACE SINCE THE PUMP π PULSE (BOTTOM) IS SWEPT ONLY BETWEEN THE TWO OBSERVER π PULSES.

The exchange coupling interaction J_o is the second main interaction giving rise to echo modulations during a DEER experiment. As described in chapter 1, its strength depends on the overlap degree of the wavefunctions of the interacting spins according to equation 5.2:

$$J_0 = -2\left\langle \phi_a(1)\phi_b(2)\left|\frac{e^2}{4\pi\varepsilon_0 r}\right|\phi_a(2)\phi_b(1)\right\rangle \quad (5.2)$$

The absolute value of J_o quickly increases as the two partners are put closer and closer together as the dependence on the distance is exponential ($J(r) = J_0 e^{-\beta r}$) and it is usually negligible at distances larger than 1.5 nm. DEER measurements on exchange coupled

system have shown that the exchange interaction alters the modulation pattern and introduces inaccuracies in the frequency data extracted from the Pake pattern if it is not taken into account appropriately [110].

TABLE 5.1 THE DEPENDENCE OF THE DIPOLAR FREQUENCY $\omega_{\perp}/2\pi$ AND OF THE ASSOCIATED MODULATION PERIOD ON THE SEPARATION BETWEEN THE TWO INTERACTING SPINS. g_1, g_2=2.005.

Interspin distance r/nm	$\lvert\omega_{\perp}/2\pi\rvert$/MHz	Associated period /ns
0.5	417	2.4
1.0	52.2	19.1
2.0	6.25	160
5.0	0.417	$2.4*10^3$
10.0	0.0522	$19*10^3$

5.2 EXPERIMENTAL CONSIDERATIONS

RESONATOR BANDWIDTH

As already stated, DEER is a double frequency technique, *i.e.* the pulses of the observer and pump sequences are centered at different microwave frequencies in order to separately excite the two interacting paramagnets. Thus from an instrumental point of view, two distinct and independent microwave sources are needed in order to perform DEER spectroscopy. A more subtle consideration regards the possibility to excite the same sample at two different frequencies with an adequate efficiency, since the resonator is usually tuned on a single frequency. Every resonator is characterized by an intrinsic bandwidth which is a measure of the resonant efficiency of the

resonator itself at different frequencies. As depicted in figure 5.2, a general resonator reaches its maximum efficiency at a precise resonant frequency while its profile can be adjusted by changing the coupling regime from the critically coupled needed in CW-EPR spectroscopy to the low-efficient but more frequency-spanned overcoupled regime for pulse EPR.

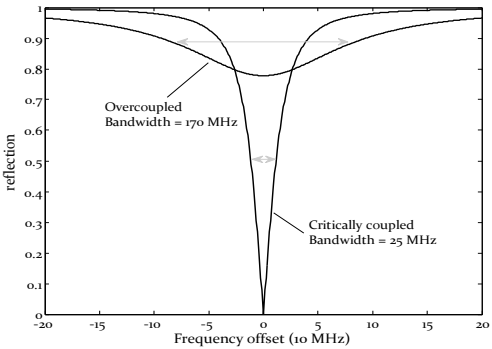

FIGURE 5.2 REFLECTED MICROWAVE POWER OF A RESONATOR IN TWO DISTINCT COUPLING REGIMES CHARACTERIZED BY 25 MHZ AND 170 MHZ BANDWIDTHS. INCREASING THE BANDWIDTH OF THE RESONATOR RESULTS IN A MORE FLAT PROFILE OVER THE FREQUENCIES, MORE POWER REFLECTED AWAY AND A LESS EFFICIENT B_1 CONVERSION. RESONATOR PROFILES OBTAINED WITH THE EASYSPIN PACKAGE [111].

When dealing with DEER spectroscopy of nitroxide probes, the bandwidth of the resonator is usually a minor problem since in that case the required frequency separation of pump and observer is around 65 MHz. The bandwidth associated to the overcoupled typical Bruker dielectric resonator for pulse EPR (ER4118X-MD5) is far larger (more than a hundred MHz) and then an effective B_1 conversion is achieved inside the resonator for both the pump and observer frequencies. In the case of larger

frequency separation between pump and observer, as that described in this chapter, the so-called "bandwidth chain" will be interrupted at the resonator level by the narrow bandwidth of the dielectric resonator. To overcome the problem a split-ring resonator specifically designed for DEER spectroscopy (ER4118X-MS3) can be employed, with a bandwidth of several hundreds of MHz.

Temperature and deuteration

Another trouble that must be taken into account is the already cited transverse relaxation of the paramagnetic centers which limits the total length of the DEER trace because of echo decay. Deuteration of the buffer and possibly of the entire system under investigation and the choice of a suitable temperature which is well balanced between the reduction of T_2 and an acceptable repetition rate (around 40 – 60 K for nitroxides) can help in this sense to reduce relaxation and to acquire longer traces with a better S/N ratio for a reliable measure of long interspin distances as already demonstrated [24, 112, 113].

Pulse parameters

As DEER spectroscopy consists in irradiating the sample with two distinct microwave pulse sequences, some considerations must be posed regarding what are the best pulse parameters to obtain the maximum sensitivity.

The pump sequence, which consists of only one π pulse, has the effect of suddenly invert the spin state of one of the paramagnetic centers. In order to achieve the maximum inversion efficiency λ thus, the pulse should

cover the largest area of the EPR spectrum of the paramagnetic centers selected as the pump spin. To obtain this result, the largest pulse bandwidth must be chosen, i.e. the π pump pulse has to be as short and strong as possible (see fig. 5.3). When the two interacting paramagnetic centers are characterized by different EPR spectra, the choice for the pump species should be invariably addressed to that with the narrower spectrum so that a larger inversion efficiency is obtained, as is the case of DEER spectroscopy between nitroxides and metal centers [114].

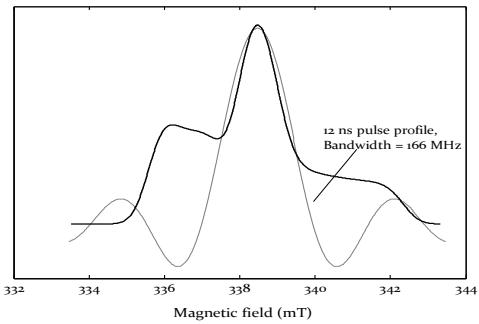

FIGURE 5.3 CALCULATED POWDER EPR SPECTRUM OF A NITROXIDE (SOLID LINE) AND EXCITATION PROFILE OF A 12 $\boldsymbol{ns}$ SQUARE PUMP PULSE CENTERED AT THE MAXIMUM OF THE EPR SIGNAL (BROKEN LINE). $\boldsymbol{g_x = 2.0091,\ g_y = 2.0061,\ g_z = 2.0023,\ A_x = 6.2\ G, A_y = 6.3\ G, A_z = 33.2\ G}$.

The observer sequence too should be set as strong as possible to increase the fraction of spin pairs contributing to the dipolar modulation, but in this case a *caveat* has to be posed. Since stronger pulses means larger associated bandwidth, there is the possibility of large spectral overlap between pump and observer pulses, especially when their frequency separation is

quite small like in nitroxide-nitroxide DEER (about 65 MHz). Spectral overlap of pump and observer pulses causes ESEEM effect to take place and artifacts to appear in the time trace due to the strong ESEEM modulations of deuterium and nitrogen. This problem can be partially overcame by conveniently sweeping the τ_1 value during the acquisition of the DEER trace over the entire modulation period of the nucleus responsible for the modulation [115].

5.3 THE TPP-NO$^{\bullet}$-*X* MODEL COMPOUNDS

In the work here described DEER spectroscopy is successfully applied to a series of model compounds composed by a tetraphenylporphyrin (TPP) moiety and a nitroxide radical connected by a synthetic peptide linker, generally known as TPP-NO-*x*, where *x* is a number indicating how many amino acids separate the TPP from the nitroxide. The peptide linker is constituted by an alternating series of L-alanine (Ala) and α-aminoisobutyrric acid (Aib) in which at the *x*-esim position the 4-amino-1-oxyl-2,2,6,6-tetramethyl-piperidine-4-carboxylic acid (TOAC) is inserted. TOAC is an artificial amino acid bearing a nitroxide group in its side chain and whose peculiarity is the spiro linkage of the six-member nitroxide ring to the C^{α} atom, which causes a very narrow spatial distribution of the -NO$^{\bullet}$ group. TOAC is also known as a strong helicogenic amino acid because of its virtually unflexible side group. The chemical structures of the building blocks of the

model compounds are summed up in figure 5.4 together with the structure of the TPP-NO-10 compound.

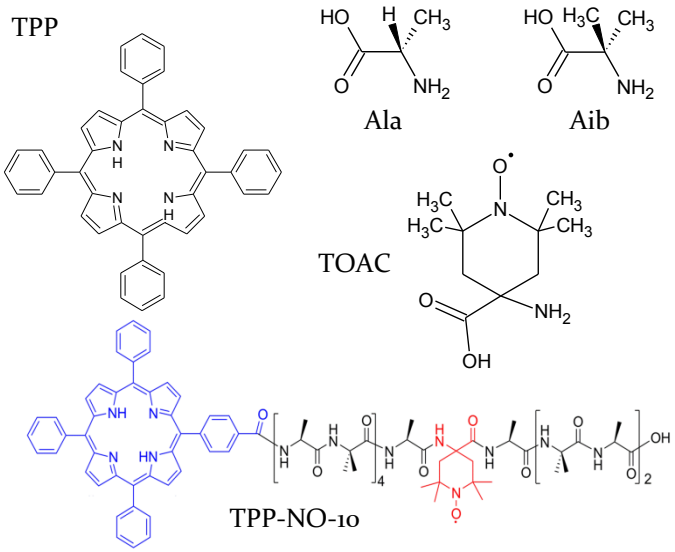

Figure 5.4 Chemical structure of the TPP, Ala, Aib and TOAC building blocks and of the bis-labeled TPP-NO-10 model compound.

Synthesis of the various TOAC containing $(Ala\text{-}Aib)_n$ sequences was performed by Enrico Zurlo in the lab of prof. Marina Gobbo (University of Padua, Chemical Sciences dept.) by means of standard solid-phase synthesis, following a protocol previously optimized for spin label-containing peptides[116] while the TPP moiety was covalently linked to the N-terminus of the peptide still attached to the solid support, as better described in Appendix A.1. The alternating L-alanine (Ala) and α-aminoisobutyrricacid (Aib) peptide bridge is known to

promote the α-helix conformation and consequently a well-defined geometry in terms of distance, relative orientation and restricted conformational flexibility is expected for the model systems TPP-NO-*x* [117]. Circular dichroism (CD) was used to assess that in methanol, the solvent used for the EPR measurements, the bis-labeled peptide retains the α-helical structure of the parent peptide. From CD, self-aggregation was also excluded.

5.4 DEER SPECTROSCOPY ON THE TPP-NO-10 COMPOUND

The investigation began with the demonstration of the feasibility of exploiting the photoexcited triplet state of TPP as a potential probe for DEER spectroscopy. TPP-NO-10 was chosen as the best system to start with, since the interspin distance of approximately 22 Å obtained from a structural model based on data reported in [118, 119] is suitable for DEER spectroscopy as reported in figure 5.5.

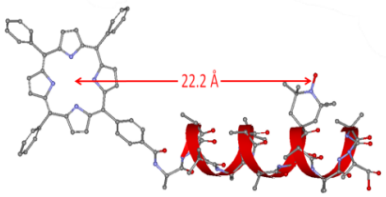

FIGURE 5.5 STRUCTURAL MODEL (WEBLAB VIEWER PRO 3.20, MOLECULAR SIMULATIONS) OF TPP-NO-10 BASED ON STRUCTURAL DATA REPORTED IN [118, 119].

The pulsed EPR measurements were carried out at X-band with a wide-bandwidth split-ring resonator on a

glassy frozen solution (20 K) of the compound in perdeuterated methanol at a concentration of ~200 μM. A laser flash at 532 nm was used to populate the TPP triplet state and to trigger the microwave pulse sequence (experimental details are reported in Appendix A.1).

FS-ESE INVESTIGATION

The photoexcited FS-ESE investigation of the TPP-NO-10 model peptide, reported in figure 5.6, reveals a composite spectrum in which the narrow central absorption signal due to the nitroxide spin label and the broad contribution, extending between 300 and 380 mT, due to TPP triplet state are both evident. The same experiment was performed without laser excitation, leaving the nitroxide contribution to the spectrum only, in order to obtain, as a difference, the FS-ESE spectrum of the ^{3}TPP system. The triplet state spectrum of TPP displays turning points corresponding to the canonical orientations of the anisotropic ZFS tensor and a specific spin-polarization pattern composed by enhanced absorptive (A) and emissive (E) lines, as a result of a non-Boltzmann population of the triplet-state sublevels, as previously discussed in chapter 2.

The FS-ESE of TPP-NO-10 allows the correct choice for pump and observer positions for the successive DEER spectroscopy. As stated before, the pump must be set in correspondence of the narrow EPR spectrum of the nitroxide in order to optimize the pump efficiency parameter λ (see eq. 2.5) [114]. The observer sequence has been set in correspondence to the most intense

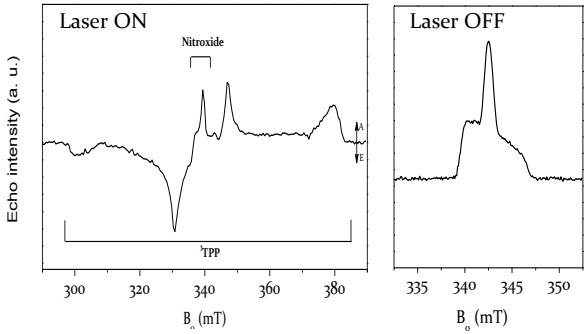

FIGURE 5.6 X-BAND FS-ESE SPECTRUM OF TPP-NO-10 (~200 ***μM***) RECORDED UNDERPHOTOEXCITATION AT 20 K (LEFT PANEL) AND THE CORRESPONDING SPECTRUM OF THE NITROXIDE LABEL IN THE ABSENCE OF LASER PHOTOEXCITATION (RIGHT PANEL). A = ENHANCED ABSORPTION, E = ENHANCED EMISSION.

emissive ZFS canonical transition of the polarized TPP triplet state spectrum, generated via pulsed laser excitation, with a pump to observer spectral separation of about 8.5 mT corresponding to 240 MHz. Since the observer pulses are softer than the pump pulse, they are characterized by a narrower bandwidth, which, combined with the huge broadening of the triplet spectrum, results in a strong orientation selection of the TPP molecule with the *Y* axis of the zero-field tensor aligned to the external magnetic field to be expected. Position and excitation profiles of the pump and observer pulses as selected are reported in figure 5.7. From the figure it is also evident that in spite of the large spectral separation between pump and observer pulses, a non-negligible pulse overlap still persists and thus the suppression of the ESEEM effect in the DEER trace is needed [115].

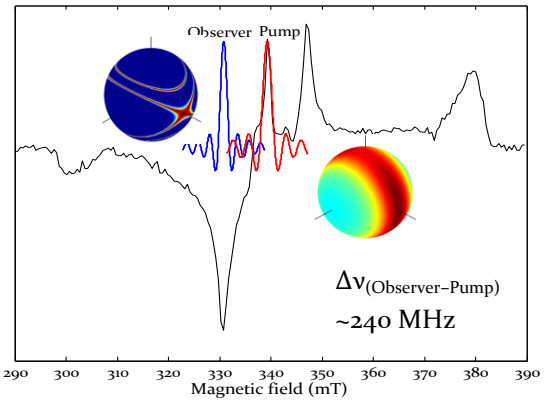

FIGURE 5.7 SPECTRAL POSITION AND EXCITATION PROFILES OF PUMP AND OBSERVER PULSES (ASSUMED TO BE SQUARE PULSES) AS SELECTED FOR DEER SPECTROSCOPY OF THE TPP-NO-10 SYSTEM. MOLECULAR ORIENTATION EXCITED BY THE PULSES ARE REPRESENTED AS COLORED SURFACES ON A UNITARY SPHERE. RED COLOR CORRESPONDS TO EXCITED ORIENTATIONS.

DEER SPECTROSCOPY ON TPP-NO-10

The DEER time trace obtained employing the previously described instrumental settings, reported in figure 5.8,reveals a well-resolved and pronounced dipolar modulation and a weak damping, such that up to at least five complete periods are clearly observable. The slow damping of the modulation suggests that the dipolar coupling regards pairs of spins with a single dominating distance. This behavior is characteristic of restricted conformational flexibility of the spin probes [120]. After removal of the background decay from the envelope modulation, Fourier transform of the signal provides the

frequency spectrum also reported in figure 5.8, in which the maximum intensity is observed at the dipolar frequency ν_{DD}= 4.8 MHz, corresponding to an interspin distance of 22.4 Å derived from eq. 5.1. Equation 5.1 is still valid for the dipolar interaction between a radical and a triplet state in the high-field approximation and neglecting any contribution from the exchange interaction at this large distance between the spin systems [121]. However small deviations from this value might derive from the ZFS contribution to the spin Hamiltonian [105, 122, 123].

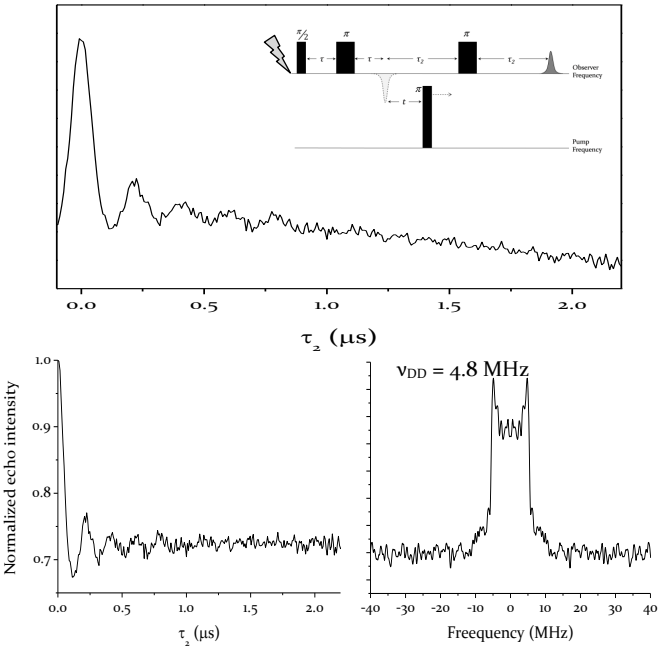

FIGURE 5.8 TOP PANEL: X-BAND FOUR-PULSE DEER TRACE OF TPP-NO-10 RECORDED UNDER PHOTOEXCITATION AT 20 K. BOTTOM PANELS: DEER TIME TRACE AFTER BACKGROUND REMOVAL (LEFT) AND AFTER FOURIER TRANSFORM TO OBTAIN THE CORRESPONDING PAKE PATTERN (RIGHT).

Despite these limits, the estimated distance is consistent with the one obtained in the point-dipole approximation from the structural model of TPP-NO-10, considering the spin label positions with the center of the porphyrin macrocycle and the midpoint of the nitroxide N–O bond as reference points in the calculation as reported in figure 5.5.

To verify that the detected modulation originates from electron–electron dipole interaction between the S = 1/2 and S = 1 partners, control PELDOR experiments with different settings of the pump and observer frequency have been performed. Indeed, by choosing both the pump field and the observer field within the nitroxide or the porphyrin spectrum, we observed no modulation at all but only an exponential decay corresponding to the homogeneous distribution of peptides in the glassy frozen solution.

Besides the demonstration of the feasibility of using a photoexcited triplet state as a potential probe for DEER spectroscopy, the time trace reported in figure 5.8 holds another key feature of employing photoinduced paramagnetic centers. Optimization of the time trace in terms of signal-to-noise ratio was achieved by reducing by 100 times the number of scans compared to typical measurements in nitroxide–nitroxide DEER experiments (the DEER trace presented in figure 5.8 has been obtained with 50 shots per point and a single scan). The significantly increased sensitivity is addressed to the intrinsic spin polarization of photoexcited triplet states, which is only partially lost in the broad features of the triplet-state spectrum.

Another point to be noted is the absence of strong orientation selection features in the time and frequency traces of figure 5.8. Orientation selection is known to introduce distortions, particularly evident in the Pake pattern rather than in the time trace, owing to missing orientation. The Pake pattern obtained for the TPP-NO-10 compound from the Fourier transform of the time trace does not show any sign of missing orientation, appearing as a typical Pake pattern as that reported in figure 2.9. This is because at the observer position almost all the possible molecular orientations with the tetrapyrrole plane parallel to the magnetic field are detected. The orientation selection is further compromised by the lack of collinearity between the ZFS principal axes and the spin–spin distance vector, according to the structural model, and to a lesser extent by the small degree of rotational freedom of the para-substituted benzoyl group with respect to the C1phenyl–CO and the C4 phenyl–tetrapyrrole ring bonds.

DEER SPECTROSCOPY ON CU(TPP)-NO-10

In order to strengthen the validity of the whole methodology, the same model compound has been synthesized with a Cu^{2+} ion coordinated by the tetrapyrrole ring of TPP. Cu(TPP)-NO-10 has been demonstrated to retain the same geometry and the same relative arrangement of the two interacting paramagnetic centers by means of DFT calculations, so it represent a suitable system to investigate the TPP-NO-10 compound with the well-developed methodology for S =

½ - S = ½ DEER spectroscopy. The potentiality of DEER spectroscopy involving Cu^{2+} ions coupled to nitroxide radicals has already been systematically investigated both on model compounds and in biological systems [114, 124]. Copper (II) is characterized by a half integer spin quantum number S = ½ which makes it suitable for the analysis of distance and distance distribution by the *DeerAnalysis* software even if the strong orientation selection due to the large *g* and *A* tensors broadening of the EPR spectrum of copper (II) ion make the analysis of Cu^{2+} DEER traces a non-trivial task.

DEER trace obtained for the S = ½ - S = ½ system Cu(TPP)-NO-10 is reported in figure 5.9 superposed to the trace relative to the photoexcited DEER on the TPP-NO-10 parent compound. The modulation pattern and the damping appear very similar in the two compounds as a demonstration of the reliability of the DEER trace obtained between the nitroxide and the S = 1 photoexcited triplet state of TPP.

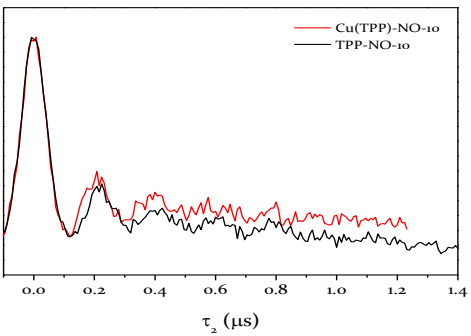

FIGURE 5.9 COMPARISON BETWEEN DEER TRACES OF PHOTOEXCITED TPP-NO-10 (BLACK TRACE) AND CU(TPP)-NO-10 (RED TRACE) PARENT COMPOUNDS OBTAINED AT 20 K.

As already introduced, equation 5.1 is still applicable in the case of S = ½ - S = 1 Pake patterns to obtain the dipolar frequency and the comparison between the traces in figure 5.9 confirm this assumption as do the traces reported in figure 5.10 in which the background corrected time trace, the corresponding Pake pattern and the distance distribution as reliably obtained with *DeerAnalysis* are reported for the Cu(TPP)-NO-10 compound.

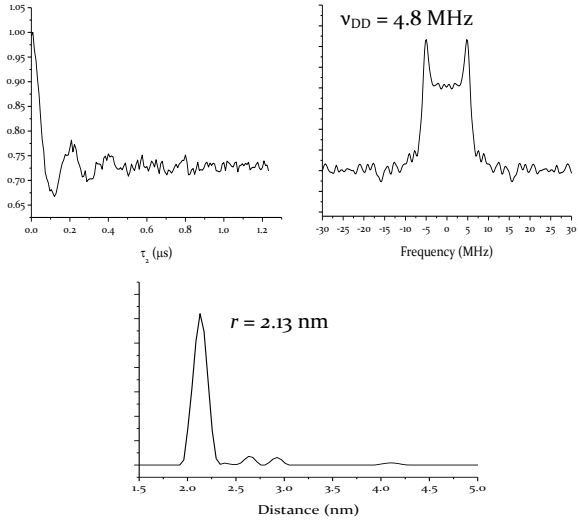

FIGURE 5.10 DEER TIME TRACE OF CU(TPP)-NO-10 COMPOUND AFTER BACKGROUND REMOVAL (TOP, LEFT) AND AFTER FOURIER TRANSFORM TO OBTAIN THE CORRESPONDING PAKE PATTERN (TOP, RIGHT). THE DISTANCE DISTRIBUTION OBTAINED VIA *DEERANALYSIS* IS REPORTED IN THE BOTTOM PANEL.

Again it should be noted the complete matching with data obtained for the TPP-NO-10 trace reported in figure 5.8. Exactly the same dipolar frequency is measured exploiting the internal peaks of the Pake pattern corresponding to the perpendicular orientation of the

vector connecting the paramagnetic centers and the external magnetic field.

The DEER trace of Cu(TPP)-NO-10 was optimized in terms of signal-to-noise ratio by performing a 14 hours collected trace at a shot repetition time of 3 ms, corresponding to a 64000 shots per point, a huge value if compared to the 50 shots per point needed for the photoexcited DEER of TPP-NO-10.

5.5 DEER SPECTROSCOPY ON A SERIES OF TPP-NO MODEL COMPOUNDS

After demonstrating the feasibility of exploiting the transient photoexcited triplet state of TPP as a probe for DEER spectroscopy with great advantages in term of sensitivity, we focused on a series of parent compounds characterized by a variable length of the peptide spacer between the two paramagnetic centers listed in table 5.2. A systematic investigation, reported in figure 5.11, has been performed on this ruler compounds with an astonishing agreement between spectral data. While the two paramagnetic centers are set far and far from each other, the period of the strong modulation in the refocused echo, mark of the dipolar interaction, becomes larger and larger and the corresponding frequency in the Pake pattern spectra drops. The damping effect appears similar in all the time traces collected, demonstrating the limited conformational flexibility among the series of model compounds.

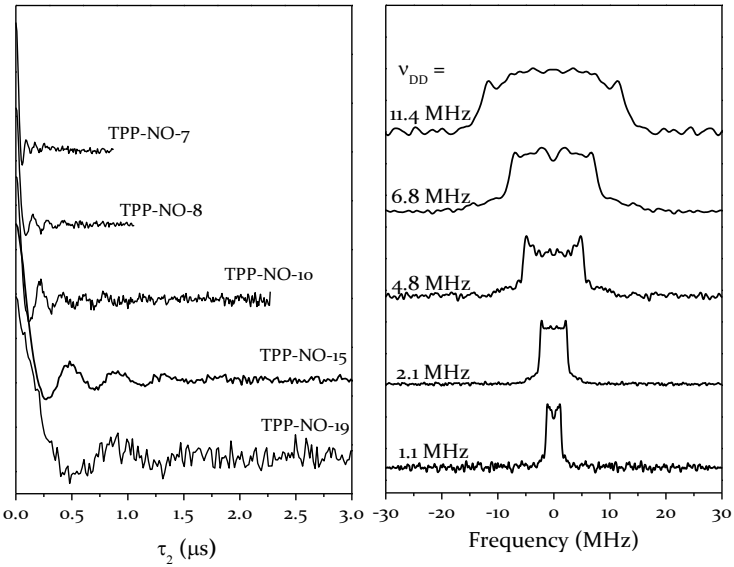

FIGURE 5.11 LEFT PANEL: DEER TIME TRACES AFTER BACKGROUND REMOVAL RECORDED FOR THE FIVE TPP-NO RELATED COMPOUNDS. TRACES HAVE BEEN VERTICALLY DISPLACED FOR THE SAKE OF CLARITY. RIGHT PANEL: FOURIER TRANSFORM OF THE CORRESPONDING TIME DOMAIN TRACES. DIPOLAR COUPLING FREQUENCIES AS OBTAINED FROM *PAKE PATTERNS* ARE REPORTED TOO.

TABLE 5.2 AMINO ACID SEQUENCE OF THE INVESTIGATED TPP-NO RELATED COMPOUNDS. TPP AND TOAC ARE HIGHLIGHTED IN BOLD.

	Formula
TPP-NO-7	**TPP**-(Ala-Aib)$_2$-Ala-Ala-**TOAC**-Ala-(Aib-Ala)$_4$-OH
TPP-NO-8	**TPP**-(Ala-Aib)$_3$-Ala-**TOAC**-Ala-(Aib-Ala)$_3$-OH
TPP-NO-10	**TPP**-(Ala-Aib)$_4$-Ala-**TOAC**-Ala-(Aib-Ala)$_2$-OH
TPP-NO-15	**TPP**-(Ala-Aib)$_4$-Ala-Ala-(Aib-Ala)$_2$-**TOAC**-Ala-Aib-Ala-OH
TPP-NO-19	**TPP**-(Ala-Aib)$_4$-Ala-Ala--(Aib-Ala)$_4$-**TOAC**-Ala-Aib-Ala-OH

The investigation of the entire series of model compounds reveals that dipolar frequencies in the range of 1 to 12 MHz are easily measured with DEER employing the TPP photoexcited triplet state as one of the interacting centers. Again optimization of the signal-to-noise ratio is achieved with a number of shots per point at least two orders of magnitude smaller than that reported for pairs of interacting nitroxides.

5.6 Simulation of TPP-NO DEER traces

More information about the spin system under investigation besides the dipolar coupling frequency can be obtained by spectral simulation. Several routines for the simulation of both the time and frequency domain DEER traces have been released, the already introduced *DeerAnalysis* being the most diffuse one. This comprehensive package for DEER spectral simulation suffers two main drawbacks: the unfeasibility of taking into account orientation selection and the limitation of being developed only for S = ½ - S = ½ systems even if in some cases the routine can be applied to the simulation of DEER spectra in higher order half-integer spin systems with minor approximations.

In order to obtain reliable simulations of the frequency DEER traces of TPP-NO presented in figure 5.11, a completely novel simulation routine has been developed in our group whose details are reported in [125]. The software takes into account both the fact that one of the spin probe is the innovative photoexcited triplet state of

TPP and the orientation selection regime in which the experiments are performed, according to the large Zero Field Interaction characterizing the triplet state of TPP. To set up a comprehensive simulation routine the full theoretical background of the DEER experiment involving a polarized triplet state interacting with a S = ½ radical has been developed in our group via density matrix formalism [125]. The results are quite surprising since a simple trigonometric dependence of the echo modulation on the dipolar coupling completely similar to that reported for the S = ½ - S = ½ case [12] has been observed:

$$V(t) = A\cos(\omega_{DD}\, t) \qquad (5.3)$$

A less trivial approach to the dipolar coupling dependence on the distance and orientation with respect to that reported in equation 5.1 is required for the systems under investigation even if the distance dependence has been demonstrated to be the same of the S = ½ - S = ½ case. Tetraphenylporphyrin is characterized by a large delocalization of the triplet state on the highly conjugated tetrapyrrole macrocyclic ring which prevents the point-dipole approximation to be safely applied. For this reason a more complete formula specific for the spin density delocalization, reported in equation 5.4, must be used:

$$\omega_{N,P} = -\frac{\mu_0 {\beta_e}^2}{4\pi\hbar}\, g_N g_P \sum_j \left(\rho_P^j \cdot \frac{3\cos^2\vartheta_{N,P_j} - 1}{{r^3}_{N,P_j}}\right) (5.4)$$

Here, for a given orientation of the system with respect to the external magnetic field, the dipolar coupling between the triplet state of TPP and the nitroxide radical

is calculated as a sum of the partial dipolar frequencies between every single atom j in the conjugated macrocycle bearing a significant triplet spin density ρ^j_P and the localized radical spin density on the nitroxide N, all of which is weighted for the spin density itself ρ^j_P.

To properly apply equation 5.4 on our systems, reliable structures and spin density distribution of the TPP-NO-x model compounds are required. The geometry optimized structures of all the members of the molecular ruler have been obtained via a DFT-ONIOM approach in collaboration with dr. Laura Orian, Padua University. At the same time the spin density distribution for both the spin probes, the tetraphenylporphyrin triplet state and the nitroxide radical, have been calculated and major results are reported in figure 5.12. With these data it has been possible to apply equation 5.4 and to calculate the dipolar coupling for a particular orientation of the molecule in the external magnetic field. The same procedure was then repeated for every possible orientation according to the frozen solution state of the sample under investigation. In this sense a probability weighting factor $\sec\vartheta$, as reported in [126], has been introduced in order to take into account the larger probability of finding molecules characterized by a perpendicular orientation of the principal direction of the dipolar tensor with respect to the external magnetic field due to the axial symmetry of the tensor. The results of the calculation of the dipolar spectra of the systems under investigation are reported in figure 5.13 and in table 5.3 together with the previously introduced experimental results (see fig. 5.11).

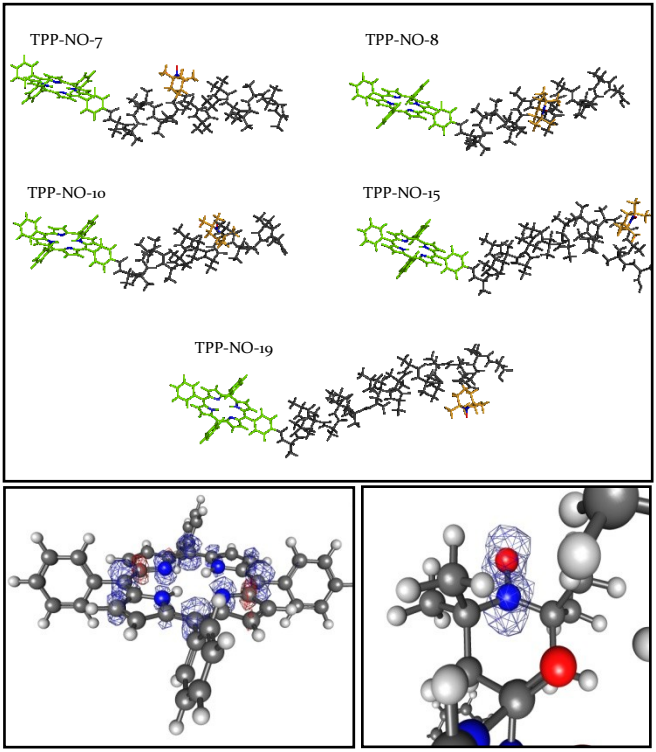

Figure 5.12 Top panel: DFT optimized structures of the bis-labeled model compounds investigated. The peptide backbone is colored in grey, the tetraphenylporphyrin is in green and the TOAC moiety in orange. Bottom panels: mesh visualization of the calculated spin densities for the triplet state of TPP (left) and for the nitroxide radical in the TOAC moiety (right).

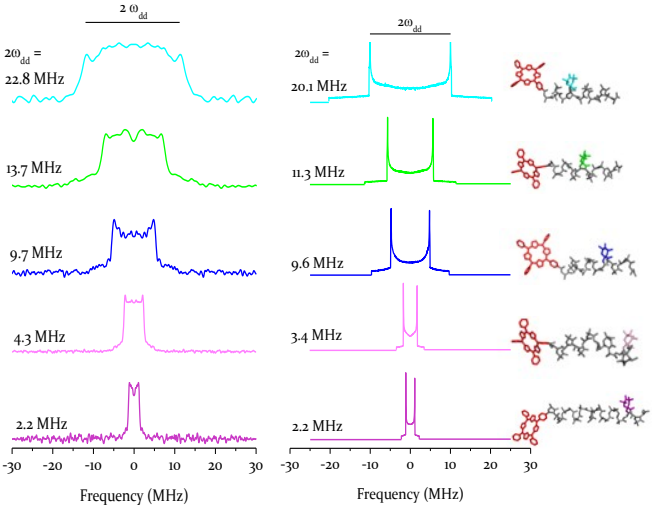

FIGURE 5.13 LEFT PANEL: EXPERIMENTAL PAKE PATTERNS RECORDED FOR THE FIVE TPP-TOAC-*X* SYSTEMS INVESTIGATED AS ALREADY REPORTED IN FIGURE 5.11. RIGHT PANEL: SIMULATED PAKE PATTERNS FOR THE SAME MOLECULES OBTAINED AFTER DFT GEOMETRY OPTIMIZATION. IN RED THE TPP MOIETY, COLORED THE TOAC POSITION, IN GREY THE (ALA-AIB) HELICAL SPACER. VALUES REPORTED CORRESPOND TO TWICE THE DIPOLAR INTERACTION AS CALCULATED FROM THE SPECTRA. COLOR CODE AS REPORTED IN TABLE 5.3.

TABLE 5.3 COMPARISON OF THE EXPERIMENTAL AND CALCULATED DIPOLAR COUPLINGS FOR THE FIVE TPP-TOAC-*X* SYSTEMS INVESTIGATED

Ruler compound	Color code	Experimental dipolar coupling (MHz)	Calculated dipolar coupling (MHz)
TPP-NO-7	Cyan	11.40	10.05
TPP-NO-8	Green	6.85	5.65
TPP-NO-10	Blue	4.85	4.80
TPP-NO-15	Pink	2.15	1.70
TPP-NO-19	Magenta	1.10	1.10

1

The calculated dipolar spectra appear in complete agreement with the experimental data with minor deviations regarding the measured dipolar coupling as is summed up in table 5.3. The shape of the dipolar spectra is well reproduced too by our simulation routine even if in this case some major differences are attributed to the inadequate background subtraction from the experimental data which has been performed by means of the *DeerAnalysis* package. The dipolar frequencies obtained from the experimental and simulated spectra allow to calculate a fictitious interspin distance in the point-dipole approximation which can be compared to the distance measured in the geometry optimized structures between the center of the tetrapyrrole ring and the center of the N-O bond of the TOAC moiety. As already stated, the point-dipole approximation in no longer valid for the systems under investigation since the triplet state delocalization is on the same order of the distance between the paramagnetic centers, but it still can be useful to test the validity of both the geometry optimization process and the simulation routine. The comparison is reported in table 5.4 in which three different distances are reported for every member of the TPP-NO peptide ruler: a distance calculated from the experimental dipolar coupling, a distance obtained from the simulated dipolar coupling and the center-to-center distance from the geometry optimized structures.

The results are in good agreement with the distances measured on the geometry optimized structures with a general slight underestimation of the distance obtained from the dipolar coupling which underlines the

unfeasibility of correctly employing the point-dipole approximation on these highly delocalized systems.

TABLE 5.4 COMPARISON BETWEEN INTERSPIN DISTANCES OBTAINED IN THE POINT-DIPOLE APPROXIMATION FROM THE EXPERIMENTAL AND SIMULATED SPECTRA AND THE CENTER-TO-CENTER DISTANCE FROM THE GEOMETRY OPTIMIZED STRUCTURES.

Ruler compound	Experimental distance (Å)	Simulated distance (Å)	Optimized distance (Å)
TPP-NO-7	16.6	17.3	17.8
TPP-NO-8	19.6	21.0	21.7
TPP-NO-10	22.1	22.1	22.9
TPP-NO-15	28.9	31.2	32.5
TPP-NO-19	36.2	36.2	36.2

5.7 APPLICATION TO THE PCP ANTENNA COMPLEX

As demonstrated in the previous sections the photoexcited triplet state is an effective spin probe for nanometer distance measurement by means of DEER spectroscopy. Several biological systems, especially that involved in the photosynthetic processes, possess their home-built potential photoexcited spin probes like the tetraphenylporphyrin employed in the systematic investigation such as chlorophylls, bacteriochlorophylls and carotenoids. The possibility of efficiently employing these endogenous spin probes for DEER spectroscopy can advance the structure investigation of biomolecules like antenna complexes which often lacks the crystal structure.

The PCP antenna complex has been already introduced in chapter 4 in which its photoprotective mechanism has

been deeply investigated by means of the ESEEM technique applied to the paramagnetic center constituted by the triplet state of the photoprotective peridinin molecule. The univocal identification of the photoprotective pair CLA601(602)-PID614(624) inside PCP antenna complex by means of EPR spectroscopy [82] has been recently strengthened by a computational *ab initio* investigation [127], thus making the PCP a well-suited playground to test the validity of the novel spin label approach based on the photoexcited triplet state for DEER spectroscopy.

As one of the paramagnetic partners involved in the dipolar interaction could be the long-living peridinin triplet state, a suitable mutant of the PCP antenna complex has been prepared in which an alanine residue has been inserted at the beginning of the primary sequence and successively mutated into a cysteine, giving the AoC PCP mutant. Using the methanethiosulfonate nitroxide spin label (MTSL) on the cysteine a single nitroxide labeled PCP antenna complex was obtained, thus making PCP appropriate to be investigated by means of DEER spectroscopy as reported in figure 5.14. The estimated interspin distance between the nitroxide radical and the center of the triplet state distribution on the photoprotective peridinins have been obtained by properly appending the spin label at the crystal structure of the PCP antenna complex (PDB entry code: 1PPR [84]). It results that two distinct distances in the order of 20 Å and 50 Å should be obtained from the analysis of the DEER trace of AoC labeled PCPC protein. Spin label mobility is expected to affect the traces.

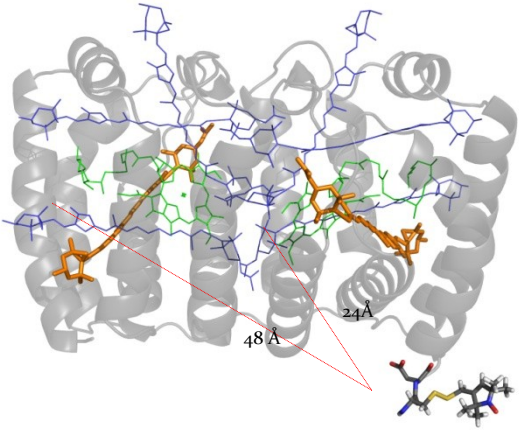

FIGURE 5.14 STRUCTURE OF THE AOC MUTANT OF THE PCP ANTENNA COMPLEX CONDENSED WITH THE MTSL SPIN LABEL. THE TWO SYMMETRY RELATED PERIDININ MOLECULES BEARING THE TRIPLET STATE AFTER THE PHOTOPROTECTION ARE HIGHLIGHTED IN ORANGE STICKS. CENTER-TO-CENTER INTERSPIN DISTANCES ARE REPORTED.

The photoexcited FS-ESE spectrum of the AoC mutant is reported in figure 5.15. It appears very similar to that obtained for the TPP-NO-10 model compound reported in figure 5.6, left panel, as it consists of two distinct superimposed spectra, the broad and polarized FS-ESE spectrum of the peridinin triplet state as also reported in chapter 4, and the narrow nitroxide moiety located in the central region of the spectrum.

Photoexcited DEER spectroscopy has been performed, analogously to the TPP-TOAC-*x* compounds, setting the pump pulse in correspondence of the maximum absorption of the nitroxide radical and the observer sequence in correspondence to the largest emissive

feature of the polarized triplet spectrum and its reported in figure 5.16. The resulting frequency offset between the two pulse sequences was a very wide 500 MHz.

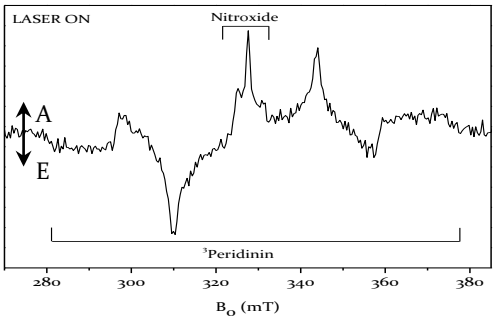

FIGURE 5.15 X-BAND FS-ESE SPECTRUM OF THE NITROXIDE LABELED A0C MUTANT OF PCP ANTENNA COMPLEX RECORDED UNDER LASER PHOTOEXCITATION AT 20 K. A = ENHANCED ABSORPTION, E = ENHANCED EMISSION.

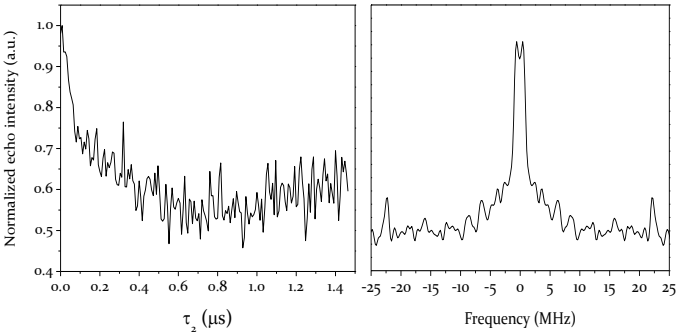

FIGURE 5.16 LOW-TEMPERATURE X-BAND DEER TIME TRACE (LEFT PANEL) AND CORRESPONDING PAKE PATTERN (RIGHT PANEL) OBTAINED FOR THE A0C LABELED MUTANT OF THE PCP ANTENNA COMPLEX FROM *AMPHIDINIUM CARTERAE*.

The DEER time trace so obtained appears less resolved than that obtained for the TPP-NO model compounds and modulations of the time trace are only poorly

noticeable. This effect is mainly due to the simultaneous presence of multiple rotamers in the frozen sample caused by spin label mobility which introduce a broad interspin distance distribution with the consequent presence of multiple interfering dipolar coupling contributing to the total modulation of the time trace. The Pake pattern trace shows the same effect of absence of well defined distances but a deeper analysis results in only two main dipolar coupling frequencies to contribute to the dipolar spectrum, 0.3 MHz and 2.5 MHz. As already discussed for the TPP-NO case the derivation of the interspin distance from the dipolar coupling is not straightforward when dealing with widely delocalized triplet states as is the case of tetraphenylporphyrin and peridinin triplet states. However as reported in table 5.4 minor deviations from the distances obtained from the exact simulation of the trace and from the computational approach are obtained by simply applying equation 5.1 to the system. Considering the two main dipolar frequency components observed in the dipolar spectrum of the labeled AoC mutant of PCP interspin distances respectively of 27 Å and 55 Å are obtained, in good agreement with the preliminary data extracted from the modified crystal structure reported in figure 5.14, thus demonstrating the feasibility of applying the photoexcited triplet state approach to DEER spectroscopy of biologically interesting systems.

5.8 Conclusions and future perspectives

This wide investigation on the opportunity of employing the photoexcited triplet state as a spin probe for nanometer distance measurement by DEER spectroscopy proved not only the feasibility of the new technique but also that these paramagnetic centers possess some unique and particularly encouraging features. The photoexcited triplet state appears to be an effective spin probe for DEER spectroscopy, revealing a huge gain in sensitivity of the technique, mainly due to the spin polarization characterizing the paramagnetic center. The wide spectral distribution of these systems in terms of magnetic fields due to the large values of the zero-field interaction allows to perform the DEER spectroscopy in the orientation selection regime, thus providing an effective tool for an accurate geometry investigation of the paramagnetic system.

The theoretical background of DEER spectroscopy of radical-triplet interacting pairs has been developed, posing the bases for the design of an effective simulation routine which takes into account the wide triplet state delocalization, the strong orientation selection and the triplet state spin polarization. The simulation routine has been tested on a series of biomimetic model compounds synthesized in our labs resulting in very promising outcomes.

Then the novel spin probe approach has been applied to a biological system bearing an endogenous triplet state probe, the photoexcited PCP antenna complex. Very

promising results have been obtained on this system characterized by a large degree of mobility of the nitroxide radical in contrast to the rigid TPP-NO biomimetic compound employed to test the feasibility of the approach.

In conclusion this work poses the theoretical and experimental background for the use of the triplet state as a spin probe for distance and orientation measurements in artificial and biological samples. The characteristic of orthogonality of the photoexcited triplet state with respect of many reported spin probes makes this approach very useful for disentangling complex situations, allowing the simultaneous measurement of multiple interspin distances and orientations and thus making this approach very promising for structure investigation in biological samples.

CHAPTER 6

CONCLUSIONS AND FURTHER WORK

This thesis has examined the application of pulse EPR to the structural investigation of different biological and biomimetic systems. Three different pulse techniques have been mainly employed, namely the electron spin echo envelope modulation (ESEEM), the hyperfine sublevel correlation (HYSCORE) and the double electron electron resonance (DEER). The techniques have been introduced in chapter 1 and 2, while their application to structure investigation has been discussed in the three experimental chapters 3, 4 and 5 where the main results of the research project followed during the three years of my Ph.D. have been presented.

Remarkable structural results have been achieved regarding both biological systems such as iron sulfur proteins and photosynthetic antenna complexes, and biomimetic model compounds. In particular HYSCORE and ESEEM techniques have been employed to investigate the nuclear surrounding of biologically interesting paramagnetic centers. The coordination environment of the [4Fe4S] cluster involved in the maturation pathway of the [Fe-Fe]-hydrogenase enzyme have been cleared up in two different organisms, revealing key similarities and differences that contribute to the fine tuning of the catalytic activity of the enzyme. Several spectroscopic efforts are now in progress in order to better elucidate the role of the GTP-asic domain of the HydF protein in order to map the significant motions of the domain and to understand how protein flexibility influence the catalytic activity. Talking about photosynthetic antenna complexes, a conserved water molecule has been identified in three different peridinin-chlorophyll a-proteins (PCP) as an active player in the

photoprotective mechanism, promoting the fast scavenge of the dangerous chlorophyll triplet state. Finally DEER spectroscopy has been employed to investigate a series of biomimetic model compounds constituting a molecular ruler exploiting a completely novel spin probe approach based on the intrinsic photoexcited triplet state. New biomimetic model compounds of the same TPP-NO-*x* type are now being synthesized in order to test the limits and the reliability of the technique. Then, from the promising results obtained on model compounds the investigation moved to a biological sample, the same PCP antenna complex already cited. Here the intrinsic carotenoid triplet state populated by the photoprotection pathway has been exploited for a preliminary structural investigation which seems to confirm previous conclusions obtained by time-resolved EPR. In this case the triplet state spin probe approach for DEER spectroscopy proved to be a very valuable tool also for protein investigation thus opening the possibilities to explore biological systems exploiting the endogenous triplet state spin probe.

The results obtained give new insights into energy transfer and conversion mechanisms in biological systems at molecular level and clear up how the fine tuning of the nuclear and protein surrounding is crucial for the correct function of a protein active center. These information regarding the surrounding of the paramagnetic centers involved in energy transfer and conversion are in turn central for the design and the assembly of artificial biomimetic and bioinspired molecular devices capable of energy conversion with extremely high efficiencies. The sustainable and

effective bio-production of fuel is nowadays one of the most important targets to be achieved from the economic, politic, environmental and social points of view and the deep understanding of how nature deals with energy conversion, transfer and storage from hundreds of millions of years represents the most reasonable way of achieving this goal.

APPENDIX A.1

MATERIALS AND METHODS

THE COORDINATION ENVIRONMENT OF THE [4FE4S] CLUSTER IN THE HYDF PROTEIN AS PROBED BY ESEEM AND HYSCORE SPECTROSCOPIES

HETEROLOGOUS EXPRESSION AND PURIFICATION OF $HYDF_{TN}$ AND $HYDF_{CA}$

The *T. neapolitana* HydF gene was isolated from purified genomic DNA by PCR amplification following standard protocols and subcloned in frame with a 6 his-tag sequence at the N-terminus in a pET-15b vector (from Novagen®)suitable for T7 driven co-expression in *E. coli*.Rosetta(DE3)pLysS cells were transformed with *the pET-15b/hydF$_{T.n.}$* recombinant plasmid and positive clones selected by antibiotic resistance. The anaerobic expression of the 6his-tagged HydF$_{T.n.}$ protein, either wild type or mutant (see below), was induced by adding 1 mM isopropyl-β-thiogalactopyranoside (IPTG), and purified to homogeneity by combining a nickel affinity (HIS-Select® Nickel Affinity Gel, from Sigma-Aldrich) a gel filtration chromatography performed with a Superdex 200HR 10/30(from GE Healthcare). All of the purification steps were performed under anaerobic conditions in a glove box (MBRAUN MB 200B) with O2-free solutions. Purified proteins were quantified by using a Micro BCA Protein Assay kit (from Thermo Scientific Pierce Protein Research)and analyzed by 12% SDS-PAGE. Following gel electrophoresis, proteins were electro-blotted onto a poly(vinyldifluoridene)membrane. For immunoblotting analysis, the membrane was probed with an anti-6his-tag monoclonal antibody (from Sigma-Aldrich) and with a horseradish peroxidase-conjugated

goat anti-mouse IgG (from Kirkegaard& Perry Laboratories). Labeled proteins were then visualized with an ECL Western blotting detection kit (from Thermo Scientific Pierce Protein Research).

Site-directed mutagenesis of $HydF_{TN}$ and $HydF_{CA}$ genes

Site-directed mutagenesis of the *hydF* genes from *T. neapolitana* and *C. acetobutylicum* was performed with the QuickChange® II Site-Directed Mutagenesis Kit (from Stratagene). Oligonucleotides were designed according to the manufacturer's guidelines and the mutant constructs analyzed by DNA sequencing.

Hydrogen evolution assay

Hydrogenase activity of whole extracts obtained from cells co-expressing a StrepII-tagged-$HydA_{C.a}$ with 6his-$HydF_{C.a.}$ (wild type and mutant proteins), $HydE_{C.a}$, and $HydG_{C.a}$ proteins were measured *in vitro* as the evolution of H_2 gas from reduced methyl viologen using nitrogen-flushed 13.5-ml sealed serum vials and a gas chromatograph (Hewlett Packard Series II 5890), fitted with a Restek 5 Å Molecular Sieve 80/100 6' 1/8" column and a thermal conductivity detector. All steps were performed anaerobically. The recombinant *pETDuet-1/strepII-hydA*$_{C.a.}$*/hydE*$_{C.a.}$ and *pRSFDuet-1/hydF*$_{C.a.}$*/hydG*$_{C.a.}$expression vectors were kindly provided by Dr. Matthew C. Posewitz (from the Department of Chemistry and Geochemistry, Colorado School of Mine, Golden, Colorado). The *pRSFDuet-1/hydF*$_{C.a.}$*/hydG*$_{C.a.}$ plasmid was used as template for *hydF*$_{C.a.}$ site-directed mutagenesis. The expression of StrepII-$HydA_{C.a.}$ and 6his-$HydF_{C.a.}$ proteins was analysed

by SDS-PAGE and Western blotting analysis, using anti-6 his-tag and anti StrepII-tag monoclonal antibodies (the latter from IBA GmbH) respectively.

D_2O EXCHANGE

D_2O exchange was performed by three successive cycles of dilution (1:10) and concentration in D_2O of 1 ml of the already purified protein. Before the last concentration step the protein was incubated in D_2O under anaerobiotic conditions for a night to complete the exchange process.

CONTINUOUS WAVE EPR SPECTROSCOPY

For EPR measurements samples concentration ranged from 50µM to 300µM. EPR tubes of as-isolated wild type and mutant $HydF_{Ca}$ $HydF_{Tn}$ proteins were prepared in an anaerobic box and frozen in liquid nitrogen. Reduced wild type and mutant HydF samples were made by supplementing the proteins with 20mM sodium dithionite, by adding a few microliters of a concentrated solution in an anaerobic buffer, and incubated for 10 min before freezing. All samples were stored in liquid nitrogen until spectral acquisition. Low-temperature CW-EPR spectra were recorded using a Bruker Elexsys E580-X-band spectrometer equipped with a ER4102ST cavity and a helium flow cryostat (ESR 900 Oxford Instruments).Acquisition parameters were the following: temperature=10K; microwave frequency=9.38 GHz; modulation frequency=100 kHz; modulation amplitude=1.0 mT, microwave power=2.0 mW; time constant=163.84 ms; conversion time=81.92 ms; number of data points=4096 (scan range=700 mT) or 1024 (scan range=100 mT). Simulations of the CW-EPR spectra were

performed using the Easyspin package running in Matlab® environment [18]; *g* values were estimated by calibration with a strong-pitch sample.

HYSCORE SPECTROSCOPY

HYSCORE experiments were carried out using the same spectrometer equipped with a dielectric ring resonator (ER4118X-MD5)and a helium flow cryostat (Oxford CF935). The HYSCORE measurements were performed at a temperature of 10K. A conventional two-dimensional (2D) four-pulse sequence (π/2–τ–π/2–t1–π–t2–π/2–τ–echo) was applied with a τ delay of 192 ns or 256 ns for the untreated and 2H2O-exchanged sample respectively for both suppression of the free Larmor proton modulation and enhancement of the deuterium modulation; a 8 ns detector gate was applied, centered at the maximum of the echo signal. The nominal duration of both the π/2 and π pulses was 16 ns. The echo intensity was measured as a function of t1 and t_2,incremented in steps of8or 12 ns from the initial value of 20 ns. HYSCORE data were collected in the form of 2D time-domain patterns as a 256x256 matrix at a repetition rate of 1200 Hz. A 4-step phase cycling procedure was used to remove unwanted echoes. Spectral processing was performed using a home-written Matlab® routine. The 2D time domain data were corrected for the unmodulated relaxation decay by a third-order polynomial background in both dimensions. Traces were apodized using a Hamming window function, zero-filled to 1024 points and Fourier transformed in both dimensions. Frequency map was symmetrised before plotting as contour plot in logarithmic scale of intensity.

3P-ESEEM SPECTROSCOPY

The three pulse ESEEM measurements were performed applying a stimulated echo sequence (π/2–τ–π/2–T–π/2–τ–echo) with a τ value of 192 ns and a 16 ns detector gate centered at the maximum of the echo signal. The length of the π/2 pulse was set to 16 ns. Echo intensity was monitored as a function of T, incremented in steps of 8 ns from the initial value of 20 ns. A total of 512 points were collected at a 1200 Hz repetition rate. A four-step phase cycle was applied to remove unwanted echoes. The final 10 points of the time trace were acquired with the integration window positioned 400 ns off the echo to define the background. The ESEEM data were processed for analysis both in the time and in the frequency domain with a home written program in MATLAB® following the ratio method introduced by Mims et al. [68]. The envelope obtained for the $^{2}H_{2}O$-exchanged sample was divided by the envelope obtained for the untreated sample after normalization of both the envelopes. The quotient time trace was then dead-time reconstructed according to the procedure described by Mims [68]. The trace was then apodized with a Hamming window function, zero-filled to 2048 data points and subjected to cosine Fourier transformation to obtain the frequency domain spectra.

SIMULATION OF ESEEM AND HYSCORE SPECTRA

Simulation of both the time and frequency domain of three-pulse ESEEM data were performed with a home-written FORTRAN routine which computes the modulation of the time domain due to the single electron spin manifolds, V^{α} and V^{β}, for any active nucleus considered. The modulations are then

assembled according to the exact product rule for three-pulse ESEEM with a home-written MATLAB program to obtain the full modulation pattern. Frequency domain spectra were obtained by cosine Fourier transformation of the time traces. The input parameters for the simulation are the external magnetic field value, the number of the nuclei, the principal values of the hyperfine tensor (A_{xx}, A_{yy}, A_{zz}), the quadrupolar interaction parameters e^2qQ and η. Spherical averaging of the interaction tensors was applied to obtain reliable simulation of the experimental data. Hyperfine parameters were chosen to obtain the best simulation while the quadrupolar parameters were slightly adjusted (e^2qQ=0.20 MHz and η=0) starting from the reported data for Ice II [128].

Simulation of HYSCORE was performed on the frequency domain data using a home-written MATLAB® program based on the *saffron* routine of the *Easyspin* package [129]. Simulation needs all the same input parameters described previously for the three-pulse ESEEM. The 2D spectrum histogram obtained is then presented as a contour plot in logarithmic scale of intensity.

Sample preparation

PCP proteins, extracted and purified, were kindly supplied by R. G. Hiller. The sample concentration was ~1.4 mg/ml. H/D exchange was achieved through dialysis with a deuterated buffer (50mM tricine, 20mM KCl, pD~7.5) at 4°C in N_2 atmosphere. A volume of about 1 ml of protein in protonated buffer was inserted into dialysis tubing (>12 kDa cut-off), which was then immerged into 40 ml of deuterated buffer. The deuterated buffer was exchanged twice. A part of the D_2O-exchanged protein solution was removed after 1.5 h of dialysis and the rest was left in the deuterated buffer up to an overall exchange time of about 20 h. Oxygen was removed from the samples by flushing argon in the EPR tube before freezing and sealing, residual oxygen was removed using glucose/glucose oxidase/peroxidase.

Pulse EPR spectroscopy

Pulsed EPR experiments were performed on the same Bruker Elexsys E580 EPR spectrometer previously described operating at X-band and equipped with a dielectric ring resonator (ER4118X-MD5). The samples were excited with an Nd: YAG laser (Quantel Brilliant) at 532 nm with about 10 mJ per pulse and a repetition rate of 10 Hz. The measurements were performed at 20 K and the temperature was controlled with a helium cryostat

(Oxford CF935) driven by a temperature controller (Oxford ITC503).

Field-swept echo-detected spectra were recorded using a 2-pulse electron spin echo sequence (flash–DAF–π/2–τ–π–τ–echo) with a delay after the laser flash (DAF) of 50 ns. The length of the π/2 pulse was set to 16 ns and the delay τ was set at 180 ns. A 60 ns *approx.* detector gate centered at the maximum of the echo signal and covering the entire echo was employed.

Three-pulse ESEEM experiments were performed with the stimulated echo sequence flash–DAF–π/2–τ–π/2–T–π/2–τ–echo by incrementing T. The delay time τ was selected in order to maximize the deuterium contribution while suppressing that due to protons. The initial value of T was set to 20 ns and varied in 12 ns increments. A total of 512 data points was recorded. The ESEEM was measured at three different magnetic field positions, corresponding to the following zero field splitting (ZFS) canonical transitions of the peridinin triplet state: Z^- (305 mT), Y^+ (314 mT) and X^+ (326.5 mT) at 9.71 GHz. The measurements were performed with DAF of 50 ns (13 μs for traces measured in correspondence of the Y^+ transition) between the laser pulse and the pulse sequence. Data were accumulated for 4–14 hours, depending on the magnetic field position. A four-step phase cycles was employed to remove unwanted echoes. The final 10 points of each time domain data set were acquired with the integration window positioned 400 ns off the echo to define the background. The ESEEM data were processed for analysis both in the time and in the frequency domain

with a home written program in MATLAB® following the ratio method introduced by Mims et al. [68]. The envelope obtained for the $^{2}H_{2}O$-exchanged sample was divided by the envelope obtained for the untreated sample after normalization of both the envelopes. The quotient time trace was then dead-time reconstructed according to the procedure described by Mims [68]. The trace was then apodized with a Hamming window function, zero-filled to 2048 data points and subjected to cosine Fourier transformation to obtain the frequency domain spectra.

Simulation of FS-ESE spectra

Field-Swept electron spin echo spectra were calculated for the computed geometries of the photoprotective site by exploiting the spin conservation of the TTET mechanism in the high field approximation [130-135], and compared with the experimental field-swept ESE-detected spectra.

Powder EPR spectra for the peridinin triplet state were simulated using Easyspin[18], which is based on full diagonalization of the triplet state spin Hamiltonian, comprehensive of the Zeeman and the ZFS interactions. The EPR parameters used in the calculation are the ZFS parameters D and E and the relative zero-field population probabilities of the three triplet sublevels.

The ZFS parameters D and E of the peridinin triplet state in PCP were taken from results of previous studies (D= -1348 MHz, E= -131.6 MHz) [136]. The ordering of the triplet state sublevels is |Z|>|Y|>|X|. The relative population probabilities were calculated with a home-written program in Matlab® based on the concept of spin

conservation during triplet-triplet energy transfer according to [137]:

$$P_k^A = \sum_h \cos^2 \theta_{hk} P_h^D$$

The population probabilities depend on the donor sublevel populations P_h^D, derived by simulation of the donor's in vitro EPR spectrum (Chlorophyll *a* in Me-THF glass [133]), and on the relative orientations of the ZFS axes of the triplet state pigments through the factor $\cos^2 \theta_{hk}$, determined for all computed geometries.

The ZFS axes of chlorophyll were taken as defined in the literature [138, 139] and the ZFS axes of peridinin were derived by applying the procedure of principal components analysis using the Matlab® function *princomp* to the spatial coordinates of the peridinin molecules taken from the optimized geometry [137]. The method is based on the solution of the covariance matrix of the data, in which the eigenvalues represent the amount of variance attributed to each eigenvector. The resulting eigenvectors are a good approximation of the ZFS axes as determined in previous EPR investigations on a single crystal of β-carotene [140]. The solution vector with the greatest eigenvalue lies along the main axis (*Z*) of the peridinin molecule, the vector with the intermediate eigenvalue lies along the C-H bonds (*X*) and the vector with the smallest eigenvalue is perpendicular to the molecular plane.

Simulation of ESEEM spectra

Simulations of both the time and frequency domain ESEEM data were performed with home-written programs in MATLAB® based on the saffron routine of Easyspin which computes the modulation frequencies and the amplitudes of the corresponding peaks and constructs a spectrum histogram [129]. The time domain signal is obtained by inverse Fourier transform. Orientation and transition selection in systems with anisotropic electron spin Hamiltonians, as in the case of triplet states, are accounted for by pre-computing the orientations contributing to the ESEEM spectrum for a certain microwave field and pulse excitation width based on the parameters of the spin Hamiltonian, e.g., the ZFS tensor in triplet state systems. The ESEEM signal is then computed only for these orientations and summed with the appropriate weights. The input parameters for the simulation are:

i) coefficients D and E, defining the ZFS interaction,

ii) principal values of the dipolar hyperfine interaction tensor A_{xx}, A_{yy} and A_{zz} and the isotropic hyperfine interaction constant aiso,

iii) $e^2qQ\hbar^{-1}$ and η defining the nuclear quadrupole interaction, and iv) Euler angles defining the orientation of the interaction tensors with respect to the molecular frame.

The ZFS parameters D and E were taken from literature[81] and the orientation of the ZFS tensor was determined by principal component analysis[80], as described in the previous section. Initial simulation

parameters for the hyperfine interaction tensor for the hydrogen/deuterium atoms of the interfaced water molecules were obtained from DFT calculations (see next section) and were optimized for the best agreement with experimental time- and frequency-domain data. The nuclear quadrupole interaction parameters of e^2qQ and η used were those reported in a nuclear quadrupole resonance study on isotopically enriched Ice II (e^2qQ = 0.25 MHz, η =0)[128]. The principal axis of the nuclear quadrupole tensor of deuterium in deuterated water was assumed to be directed along the O-^{2}H bond and the Euler angles with respect to the molecular frame were calculated accordingly. ESEEM simulations for the deuterons on the peridinin molecule were performed using the hyperfine values obtained from DFT calculations. The contributions of matrix deuterons to the ESEEM traces were estimated by calculating the dipolar hyperfine interaction with the point-dipole approximation for a series of "test protons" at positions defined by a three-dimensional grid surrounding peridinin on the X-ray structure. Since the spin density in peridinin is distributed along the whole conjugated chain, the dipolar interaction has to be calculated as a weighted sum of point-dipolar interactions between the nucleus and the various atoms over which the spin density is distributed, *i.e.* $A_{total} = {}^1/_4 \sum_i \rho_i A_i$ where A_i is the dipolar tensor calculated for the interaction of the nucleus with the normalized spin density ρ_i on the atom *i*. The dipolar hyperfine tensor components of the "test protons" located at each intersection point of the defined grid were evaluated and hyperfine isosurfaces based on the intermediate component of the hyperfine

tensor, A_{mid}, were computed with a numerical method proposed in references [141, 142]. The isosurfaces were used to evaluate the number of exchangeable protons at different distances from peridinin using the coordinates of the exchangeable protein backbone protons and free water molecules from the X-ray structure. Their contribution to the ESEEM traces was computed by assuming an axial hyperfine tensor with the principal values [A_{mid}, A_{mid}, $-2A_{mid}$] for each isosurface and by summing the contributions of the different nuclei according to the product rule. The overall procedure was implemented in a home-written MATLAB® program.

COMPUTATIONAL DETAILS

The geometry of the molecular cluster involved in the photoprotective mechanism in the two different PCP complexes investigated were optimized at DFT as well as ONIOM[143, 144] level of theory as implemented in Gaussian[145]. Calculations were kindly done by dr. Claudia Tait, Oxford University, following the same procedure described in the paper which describes the first investigation of this type on the PCP antenna complex from *Amphidinium carterae* [135], here summarized.

Initially a DFT ground state optimization with no constraints of a system constituted by the photoprotective peridinin, the related chlorophyll *a* without phytol chain, the sidechain of the water-coordinating histidine and the interposed water molecule coordinated to the Mg2+ ion of chlorophyll *a*, were performed at B3LYP/6-31G(d) [146, 147]level of

theory. The input coordinates were taken from the X-ray structure.

The structures obtained with full optimization were not a satisfactory models of the photoprotective site due to the excessive curvature of the peridinin molecule, the variation of the relative orientation of the PID-CLA pair and the rearrangement of the unconstrained histidine residue, moving away from the chlorophyll ring and changing the position of the hydrogen-bonded water molecule accordingly. Therefore, a series of constrained geometry optimizations, including additional residues, were performed with better results. This provided strong evidence in favor of the importance of the surrounding matrix and prompted us to perform ONIOM calculations, with the aim of obtaining a reliable geometry without imposing artificial constraints.

In an ONIOM B3LYP/6-31G(d):UFF full optimization the higher(inner) layer, *i.e.* the same system used in the full geometry optimization, was described at B3LYP/6-31G(d) level; the lower (outer) layer, treated at molecular mechanics level, was defined by including all the residues of the protein surroundings located at a distance of 4 Å from the atoms of the peridinin and the chlorophyll ring. This geometry is in very good agreement with the X-ray structure and has been used for subsequent calculations unless stated otherwise in the text.

The spin densities of the triplet states were computed *in vacuo* at the B3LYP/6-311G(d,p) level of theory on the Chlorophyll *a*–Peridinin–Water system extracted from the ONIOM optimized geometries of the two

investigated systems. The hyperfine coupling parameters of the H atoms of the interposed water molecules were calculated with B3LYP and the purposely tailored EPRII basis set for H, C, N and O nuclei and the 6-311G(d,p) basis set for Mg. Environmental effects on the spin density and the hyperfine coupling parameters have been included by employing the Polarizable Continuum Method with a dielectric constant of 3.0.

PEPTIDE SYNTHESIS

All chemicals were commercial products of the best grade available and, unless otherwise indicated they were used directly without further purification. 5-(4-Carboxyphenyl)-10,15,20-triphenylporphyrin (TPP-OH) and 9-Fluorenylmethoxycarbonyl(Fmoc)-4-amino-1-oxyl-2,2,6,6,-tetramethylpiperidine-4-carboxylic acid (Fmoc-TOAC) were prepared according to literature procedures. 1,2Fmoc-amino acids and all other chemicals for the solid phase synthesis were supplied by Sigma-Aldrich. H-Ala-2-Chlorotrityl resin was purchased from Novabiochem (Merck Biosciences). Analytical HPLC separations were carried out on a Dionex Summit Dual-Gradient HPLC, equipped with a four-channel UV-Vis detector, using a Vydac 218TP54 C18 or Phenomenex Jupiter C4 column (250 x 4.6 mm, 5 μm, flow rate at 1.5 mL/min). The mobile phase A (aqueous 0.1% trifluoroacetic acid (TFA)) and B (90% aqueous acetonitrile containing 0.1% TFA) were used for preparing binary gradients. All crude peptides were purified to 95% or more homogeneity for analytical and other experimental purposes. Semi-preparative HPLC was carried out on a Shimadzu series LC-6A chromatographer, equipped with two independent pump units, an UV-Vis detector, and a Vydac 218TP1022 column (250 x 22 mm, 10 μm, flow rate at 15 mL/min) or Phenomenex Jupiter C4 column (250 x 10 mm, 10 μm,

flow rate at 5 mL/min). Elutions were carried out by the same mobile phases described above, without TFA as modifier. Mass spectral analyses were performed on a Mariner API-TOF Workstation (PerSeptiveBiosystemsInc), operating with ESI techniques in positive mode. UV-Vis spectra were recorded at room temperature on a Shimadzu UV-2501PC spectrophotometer or on a Lambda 5 spectrophotometer (Perkin-Elmer), in 1 cm quartz cells. CD measurements were carried out on a Jasco-715 spectropolarimeter, using a quartz cell of 0.02 or 0.1 cm path length. The spectra were recorded at 298 K and were the average of a series of six scans made at 0.1 nm intervals in the 190-250 nm and 350-550 nm regions. Sample concentrations in methanol were in the range 0.1-0.01 mM. Ellipticity is reported as mean residue ellipticity $[\theta]_R$ (deg x cm^2 x $dmol^{-1}$) or differential molar circular dichroic extinction coefficient $\Delta\varepsilon = \varepsilon_L - \varepsilon_R$ (cm^2 $dmol^{-1}$). Solution FT-IR spectra were recorded at 293 K using a Perkin-Elmer model 1720X FT-IR spectrophotometer, nitrogen flushed, equipped with a sample-shuttle device, at 2 cm^{-1} nominal resolution, averaging 100 scans. Solvent (baseline) spectra were recorded under the same conditions. For spectral elaboration the software SpectraCalc provided by Galactic (Salem, MA) was employed. Cells with path lengths of 1.0 and 10 mm (with CaF_2 windows) were used. Spectrograde deuterated chloroform (99.8%, d_2) was purchased from Merck.

The peptide sequences were assembled on an automated Advanced Chemtech348Ω Peptide Synthesizer, on 0.05 mmol scale, starting from H-Ala-2-Chlorotrityl resin

(substitution 0.77 mmol/g resin). Fmoc deprotection was achieved with 20% piperidine in DMF (5 + 15 min). Couplings were performed in the presence of O-(7-azabenzotriazol-1-yl)N,N,N',N'-tetramethyluroniumhexafluorophosphate/N,N-diisopropylethylamine (DIPEA) (reaction time 45-60 min), using an excess of 4 equivalents of the carboxyl component. After the coupling of the last amino acid and removal of the Fmoc group, the resin was washed with DMF and CH_2Cl_2 and then dried under vacuum. The peptide-resin was split in two: one portion was acetylated by reaction with 0.5 M acetic anhydride/ 0.12 M DIPEA in DMF for 45min. The remaining H-peptide-resin(0.025 mmol) was reacted with the porphyrin(0.05 mmol in DMF-CH_2Cl_2, 1:1 v/v)in the presence of diisopropylcarbodiimide/1-hydroxybenzotriazole as coupling reagents. The reaction mixture was shaken overnight and the resin was repeatedly washed with DMF and CH_2Cl_2, until the filtrate was colorless.

The peptides were cleaved from the resin upon 3-4 treatments with 30% 1,1,1,3,3,3-hexafluoropropan-2-ol (HFIP) in DCM for 30 min. The filtrates were combined and evaporated to dryness providing the crude peptides, both presenting the intact nitroxylic radical. The crude peptides were purified by semi-preparative HPLC to afford the desired products with a purity ≥95% as determined by analytical HPLC.

EPR SPECTROSCOPY

The bis-labeled model peptides TPP-NO were dissolved in a mixture of 98% deuterated methanol (Sigma Aldrich) and 2% D_2O (Cambridge Isotopes) to reach a final concentration of approximately 200 μM. The

sample was inserted into a quartz EPR tube, which was sealed after several freeze-thaw cycles. Removal of oxygen assures long-term stability of the porphyrin label under photoexcitation.

Pulsed EPR was performed on a Bruker Elexsys E580 pulse EPR spectrometer equipped with a Bruker split-ring resonator ER4118X-MS3 (microwave frequency = 9.55 GHz) and an Oxford CF935 cryostat. The measurements were performed at a temperature of 20 K. The TPP-NO samples were photoexcited with the second harmonic of a pulsed Nd:YAG laser (532 nm) with an average power of 5 mW and a repetition rate of 10 Hz. No photoexcitation was required for the Cu(TPP)-NO sample.

For the electron spin-echo experiments a standard Hahn echo sequence (laser flash – DAF – $\pi/2$ – τ – π – τ – echo) was employed with a nominal length of 16 ns for the $\pi/2$ pulse, a delay after the laser flash (DAF) value of 50 ns (only for photoexcited experiments) and a τ value of 300 ns.

For the DEER experiments a standard four pulse sequence (laser flash – DAF – $\pi/2$ – τ – π – τ_1 – π_{pump}– τ_2 – π – τ_2 – echo) was applied at a DAF of 50 ns; the microwave power was adjusted to obtain an observer sequence of 16/32/32 ns and a pump pulse of 12 ns. The difference between the pump (nitroxide) and observer (porphyrin triplet-state) frequency was set to 240 MHz. A two-step phase cycle was applied for base-line correction while deuterium nuclear modulations were suppressed using an 8 step τ cycle from a 180 ns starting value with 56 ns increment steps. Measurement time was approximately 7 hours at a repetition frequency of 10

Hz. For the Cu(TPP)-NO sample the DEER sequence was not preceded by the laser flash and consequently the shot repetition time was shortened to 3 ms. Measurement in this case takes approximately 14 hours.

DEER time traces as obtained from the spectrometer were treated using the *DeerAnalysis2013* routine [108]. A phase correction was performed prior to correct the traces for the background decay. Fourier Transform was then applied to obtain the *Pake pattern* motif. Only in the case of Cu(TPP)-NO the distance distribution was computed with the same software.

DFT GEOMETRY OPTIMIZATION OF TPP-NO SYSTEMS

The initial structures for the calculations were prepared starting from the crystallographic coordinates of the tetraphenylporphyrin and an α-helix dodecapeptide of alternating Ala-Aib residues, from the Cambridge Crystallographic Data Center (CCDC). Each ruler was made adding the proper number of Ala-Aib residues to the dodecapeptide, substituting the right amino acid along the chain with the TOAC spin probe and attaching a tetraphenylporphyrin, with a para-carboxilic group in one of the phenyl rings at the beginning of the chain.

The geometry optimization of the shorter rulers (TPP-NO-7, TPP-NO-8, TPP-NO-10) in the doublet state were made using the Density functional Theory (DFT) method, *in vacuo*, at PBE1PBE/6-31G(d) level of theory as implemented in the software package Gaussian[145]. A QM/QM approach was set up for the geometry optimization of the longer rulers (TPP-NO-15 and TPP-NO-19), using the ONIOM approach implemented in

Gaussian. The inner layer, constituted by the tetraphenylporphyrin and the TOAC moieties, has been described using DFT at the PBE1PBE/6-31G(d) level of theory, while the PM3 Hamiltonian has been employed for the remaining outer layer. The triplet state spin density has always been computed at the same level of theory.

A similar approach has been used for the geometry optimization of the Cu(TPP)-NO-10 system; a PBE1PBE/6-31G(d) functional describes the organic part of the molecule while for the Cu^{2+} ion the Stuttgart RSC 1997 ECP functional has been chosen.

DEER TRACE SIMULATION

The simulation of the DEER dipolar spectra have been performed by an home-written routine developed in the Matlab environment. The details of the routine are exposed somewhere else [125].

Basically the routine takes as input the optimized geometry of the system, the zero-field splitting (ZFS) axis system of the tetraphenylporphyrin and the computed triplet state spin densities. It explores a set of orientations of the external field $B_0(\theta,\varphi)$, homogeneously distributed on a sphere centered in the ZFS frame of the tetraphenylporphyrin and for each position the dipolar frequency, according to equation 5.4, is computed. It should be noted that this method is equivalent, but does not correspond to the experimental conditions, in which the external magnetic field is fixed along a direction while the molecules are randomly distributed in a frozen solution matrix. A probability weighting factor $\sec\vartheta$, as reported in [126], has been introduced in order to take

into account the larger probability of finding molecules characterized by a perpendicular orientation of the principal direction of the dipolar tensor with respect to the external magnetic field due to the axial symmetry of the tensor. The routine has been appropriately implemented to perform calculations in the orientation selection regime by means of the *EasySpin* function *Orisel* [129].

The ambiguity in the direction of the *X* and *Y* principal axis of the ZFS tensor of tetraphenylporphyrin has been taken into account. The relative orientation of the two nearly equivalent axis is defined, in TPP, by the position of the symmetry-breaking protonated (aminic) pyrrolic nitrogens, which lower the symmetry to the D_{2h} point group. Since the aminic/iminic equilibrium of the pyrrolic nitrogens is very labile, an uncertainty in the direction of the *X* and *Y* axis is produced. For this reason the dipolar spectra are simulated in the two possible tautomeric forms of the TPP moiety and then summed together with a 1:1 ratio.

DEER spectroscopy on the PCP antenna complex

For the DEER experiment on the AoC mutant of the PCP complex a standard photoexcited four pulse sequence (laser flash – DAF – $\pi/2 - \tau - \pi - \tau_1 - \pi_{pump} - \tau_2 - \pi - \tau_2$ – echo) was applied at a DAF of 50 ns; the microwave power was adjusted to obtain an observer sequence of 16/32/32 ns and a pump pulse of 12 ns. The difference between the pump (nitroxide) and observer (carotenoid triplet-state) frequency was set to 500 MHz. A two-step phase cycle was applied for base-line correction while

deuterium nuclear modulations were suppressed using an 8 step τ cycle from a 180 ns starting value with 56 ns increment steps. Measurement time was approximately 7 hours at a repetition frequency of 10 Hz and a temperature of 65 K. DEER time traces as obtained from the spectrometer were treated using the *DeerAnalysis2013* routine [108]. A phase correction was performed prior to correct the traces for the background decay. Fourier Transform was then applied to obtain the *Pake pattern* motif.

APPENDIX A.2

BIBLIOGRAPHY

1. Zeeman, P., *The Effect of Magnetisation on the Nature of Light Emitted by a Substance.* Nature, 1897. **55**(1424).
2. Zeeman, P., *Doublets and triplets in the spectrum produced by external magnetic forces.* Philosophical Magazines, 1897. **44**(266): p. 6.
3. Cogdell, R.J. and H.A. Frank, *How carotenoids function in photosynthetic bacteria.* Biochimica et Biophysica Acta (BBA)-Reviews on Bioenergetics, 1987. **895**(2): p. 63-79.
4. Dexter, D.L., *A theory of sensitized luminescence in solids.* The Journal of Chemical Physics, 1953. **21**(5): p. 836-850.
5. Imamura, T., et al., *Conservation of spin-polarization during triplet-triplet energy transfer in low-temperature matrixes.* The Journal of Physical Chemistry, 1984. **88**(18): p. 4028-4031.
6. Murai, H., et al., *Intermolecular energy transfer of the spin-polarized triplet state in a N3-cyclodextrin cavity.* Chemical physics letters, 1988. **144**(4): p. 417-420.
7. Akiyama, K., et al., *Spin polarization conservation during intramolecular triplet-triplet energy transfer studied by time-resolved EPR spectroscopy.* Journal of the American Chemical Society, 1994. **116**(12): p. 5324-5327.
8. Brenner, H., J. Brock, and C. Harris, *Energy exchange in a coherently coupled ensemble.* Chemical Physics, 1978. **31**(1): p. 137-164.
9. El-Sayed, M., D. Tinti, and E. Yee, *Conservation of spin direction and production of spin alignment in triplet-triplet energy transfer*. 1969, DTIC Document.
10. Rinard, G.A., et al., *Frequency Dependence of EPR Signal Intensity, 250 MHz to 9.1 GHz.* Journal of Magnetic Resonance, 2002. **156**(1): p. 113-121.
11. Weil, J.A.B., James R., *Electron Paramagnetic Resonance. Elementary Theory and Practical Applications.* Wiley-Interscience, 2007.
12. Schweiger, A. and G. Jeschke, *Principles of pulse electron paramagnetic resonance.* Oxford University Press, Great Clarendon Street, Oxford, OX 2 6 DP, UK, 2001., 2001: p. 1-578.

13. Rowan, L.G., E.L. Hahn, and W.B. Mims, *Electron-Spin-Echo Envelope Modulation.* Physical Review, 1965. **A137**(61).
14. Mims, W.B., *Envelope Modulation in Spin-Echo Experiments.* Physical Review, 1972. **B5**(2409).
15. Deligiannakis, Y., M. Louloudi, and N. Hadjiliadis, *Electron spin echo envelope modulation (ESEEM) spectroscopy as a tool to investigate the coordination environment of metal centers.* Coordination Chemistry Reviews, 2000. **204**: p. 1-112.
16. Dikanov, S.A. and Y.D. Tsvetkov, *Electron spin echo envelope modulation (ESEEM) spectroscopy.* CRC Press, Boca Raton, 1992.
17. Prisner, T., M. Rohrer, and F. MacMillan, *Pulsed EPR spectroscopy: Biological applications.* Annual Review of Physical Chemistry, 2001. **52**: p. 279-313.
18. Stoll, S. and A. Schweiger, *EasySpin , a comprehensive software package for spectral simulation and analysis in EPR.* Journal of Magnetic Resonance, 2006. **178**: p. 42-55.
19. Poppl, A. and L. Kevan, *A Practical Strategy for Determination of Proton Hyperfine Interaction Parameters in Paramagnetic Transition Metal Ion Complexes by Two-Dimensional HYSCORE Electron Spin Resonance Spectroscopy in Disordered Systems.* The Journal of Physical Chemistry, 1996. **100**(9): p. 3387-3394.
20. Bowers, K.D. and W.B. Mims, *Paramagnetic Relaxation in Nickel Fluosilicate.* Physical Review, 1959. **115**(2): p. 285-295.
21. Milov, A.D., K.M. Salikhov, and M.D. Shchirov, *Use of the double resonance in electron spin echo method for the study of paramagnetic center spatial distribution in solids.* Fiz. Tverd. tela, 1981. **23**: p. 975-982.
22. Milov, A.D., P. A.B., and Y.D. Tsvetkov, *Electron-electron double resonance in electron spin echo: model biradical systems and the sensitized photolysis of decalin.* Chemical physics letters, 1984. **110**: p. 67-72.
23. Jeschke, G., *Distance measurements in the nanometer range by pulse EPR.* Chemphyschem : a European journal

of chemical physics and physical chemistry, 2002. **3**(11): p. 927-32.
24. Jeschke, G. and Y. Polyhach, *Distance measurements on spin-labelled biomacromolecules by pulsed electron paramagnetic resonance.* Physical chemistry chemical physics : PCCP, 2007. **9**(16): p. 1895-910.
25. Reginsson, G.W. and O. Schiemann, *Pulsed electron-electron double resonance: beyond nanometre distance measurements on biomacromolecules.* The Biochemical journal, 2011. **434**(3): p. 353-63.
26. Jeschke, G., *DEER distance measurements on proteins.* Annual review of physical chemistry, 2012. **63**: p. 419-46.
27. Vignais, P.M., B. Billoud, and J. Meyer, *Classification and phylogeny of hydrogenases1.* FEMS microbiology reviews, 2001. **25**(4): p. 455-501.
28. Vignais, P.M. and B. Billoud, *Occurrence, classification, and biological function of hydrogenases: an overview.* Chemical reviews, 2007. **107**(10): p. 4206-4272.
29. Hatchikian, E.C., et al., *Further characterization of the [Fe]-hydrogenase from Desulfovibrio desulfuricans ATCC 7757.* European journal of biochemistry / FEBS, 1992. **209**(1): p. 357-65.
30. Ogata, H., et al., *Activation process of [NiFe] hydrogenase elucidated by high-resolution X-ray analyses: conversion of the ready to the unready state.* Structure, 2005. **13**(11): p. 1635-1642.
31. Nicolet, Y., et al., *Desulfovibrio desulfuricans iron hydrogenase: the structure shows unusual coordination to an active site Fe binuclear center.* Structure, 1999. **7**(1): p. 13-23.
32. Afting, C., et al., *Regulation of the synthesis of H2-forming methylenetetrahydromethanopterin dehydrogenase (Hmd) and of HmdII and HmdIII in Methanothermobacter marburgensis.* Archives of microbiology, 2000. **174**(4): p. 225-232.
33. Lubitz, W., et al., *Hydrogenases.* Chemical reviews, 2014. **114**(8): p. 4081-4148.

34. Posewitz, M., et al., *Identification of genes required for hydrogenase activity in Chlamydomonas reinhardtii.* Biochemical Society Transactions, 2005. **33**(1): p. 102-104.
35. Posewitz, M.C., et al., *Discovery of two novel radical S-adenosylmethionine proteins required for the assembly of an active [Fe] hydrogenase.* Journal of Biological Chemistry, 2004. **279**(24): p. 25711-25720.
36. Mulder, D.W., et al., *Insights into [FeFe]-hydrogenase structure, mechanism, and maturation.* Structure, 2011. **19**(8): p. 1038-1052.
37. Shepard, E.M., et al., *Synthesis of the 2Fe subcluster of the [FeFe]-hydrogenase H cluster on the HydF scaffold.* Proceedings of the National Academy of Sciences of the United States of America, 2010. **107**(23): p. 10448-53.
38. McGlynn, S.E., et al., *HydF as a scaffold protein in [FeFe] hydrogenase H-cluster biosynthesis.* FEBS letters, 2008. **582**(15): p. 2183-2187.
39. McGlynn, S.E., et al., *In vitro activation of [FeFe] hydrogenase: new insights into hydrogenase maturation.* JBIC Journal of Biological Inorganic Chemistry, 2007. **12**(4): p. 443-447.
40. Mulder, D.W., et al., *Activation of HydAN EFG requires a preformed [4Fe-4S] cluster.* Biochemistry, 2009. **48**(26): p. 6240-6248.
41. Cendron, L., et al., *Crystal structure of HydF scaffold protein provides insights into [FeFe]-hydrogenase maturation.* The Journal of biological chemistry, 2011: p. 1-12.
42. King, P.W., et al., *Functional studies of [FeFe] hydrogenase maturation in an Escherichia coli biosynthetic system.* Journal of bacteriology, 2006. **188**(6): p. 2163-2172.
43. Brazzolotto, X., et al., *The [Fe-Fe]-hydrogenase maturation protein HydF from Thermotoga maritima is a GTPase with an iron-sulfur cluster.* The Journal of biological chemistry, 2006. **281**(2): p. 769-74.
44. Mansy, S.S., et al., *Crystal structure and stability studies of C77S HiPIP: A serine ligated [4Fe-4S] cluster.* Biochemistry, 2002. **41**(4): p. 1195-1201.

45. Hurley, J.K., et al., *Iron-sulfur cluster cysteine-to-serine mutants of Anabaena [2Fe-2S] ferredoxin exhibit unexpected redox properties and are competent in electron transfer to ferredoxin: NADP+ reductase.* Biochemistry, 1997. **36**(49): p. 15109-15117.
46. Moulis, J.-M., et al., *The coordination sphere of iron-sulfur clusters: lessons from site-directed mutagenesis experiments.* JBIC Journal of Biological Inorganic Chemistry, 1996. **1**(1): p. 2-14.
47. Peters, J.W., *X-ray Crystal Structure of the Fe-Only Hydrogenase (CpI) from Clostridium pasteurianum to 1.8B Angstrom Resolution.* Science, 1998. **282**(5395): p. 1853-1858.
48. Volbeda, A., et al., *Crystal structure of the nickel-iron hydrogenase from Desulfovibrio gigas.* Nature, 1995. **373**(6515): p. 580.
49. Wang, W., et al., *Pyridine inhibitor binding to the 4Fe-4S protein A. aeolicus IspH (LytB): a HYSCORE Investigation.* Journal of the American Chemical Society, 2011. **133**: p. 6525-8.
50. Silakov, A., Wenk, and W. Lubitz, *14N HYSCORE investigation of the H-cluster of [FeFe] hydrogenase: evidence for a nitrigen in the dithiol bridge.* Physical chemistry chemical physics : PCCP, 2009. **11**: p. 6626-37.
51. Dikanov, S.a., et al., *A comparative, two-dimensional 14N ESEEM characterization of reduced [2Fe-2S] clusters in hyperthermophilic archaeal high- and low-potential Rieske-type proteins.* Journal of biological inorganic chemistry : JBIC : a publication of the Society of Biological Inorganic Chemistry, 2004. **9**: p. 753-67.
52. Samoilova, R.I., et al., *The interaction of the Rieske iron-sulfur protein with occupants of the Q0-site of the bc1 complex, probed by electron spin echo envelope modulation.* The Journal of biological chemistry, 2002. **277**: p. 4605-8.
53. Tyryshkin, A.M., et al., *Characterization of Bimodal Coordination Structure in Nitrosyl Heme Complexes through Hyperfine Couplings with Pyrrole and Protein Nitrogens.* Nitric Oxide, 1999: p. 3396-3406.

54. Dikanov, S.A., et al., *Orientationally-Selected Two-Dimensional ESEEM Spectroscopy of the Rieske-Type Iron-Sulfur Cluster in Burkholderia cepacia AC1100.* Biochemistry, 1996. **7863**: p. 8408-8416.
55. Chatterjee, R., et al., *High-resolution two-dimensional 1H and 14N hyperfine sublevel correlation spectroscopy of the primary quinone of photosystem II.* Biochemistry, 2011. **50**(4): p. 491-501.
56. Foerster, S., et al., *An orientation-selected ENDOR and HYSCORE study of the Ni-C active state of Desulfovibrio vulgaris Miyazaki F hydrogenase.* Journal of biological inorganic chemistry : JBIC : a publication of the Society of Biological Inorganic Chemistry, 2005. **10**(1): p. 51-62.
57. Jiang, F., J. McCracken, and J. Peisach, *11)-Diethylenetriamine-Substituted.* 1990(12): p. 9035-9044.
58. Gruner, I., et al., *Aspartate 141 Is the fourth ligand of the oxygen-sensing [4Fe-4S] 2+ cluster of Bacillus subtilis transcriptional regulator Fnr.* Journal of Biological Chemistry, 2011. **286**(3): p. 2017-2021.
59. Brereton, P.S., et al., *Effect of iron-sulfur cluster environment in modulating the thermodynamic properties and biological function of ferredoxin from Pyrococcus furiosus.* Biochemistry, 1998. **37**(20): p. 7351-7362.
60. Berto, P., et al., *The [4Fe-4S]-cluster coordination of [FeFe]-hydrogenase maturation protein HydF as revealed by EPR and HYSCORE spectroscopies.* 2012.
61. Kappl, R., et al., *Probing Electronic and Structural Properties of the Reduced [2Fe-2S] Cluster by Orientation-Selective ~ H ENDOR Spectroscopy : Adrenodoxin versus Rieske Iron-Sulfur Protein.* Applied Magnetic Resonance, 2006. **459**: p. 427-459.
62. Kappl, R., S. Ciurli, and C. Luchinat, *Probing Structural and Electronic Properties of the Oxidized [Fe4S4] 3+ Cluster of Ectothiorhodospira halophila iso-II High-Potential Iron - Sulfur Protein by ENDOR Spectroscopy.* Journal of the American Chemical Society, 1999(16): p. 1925-1935.

63. Doan, P.E., C. Fan, and B.M. Hoffman, *ENDOR and 2H-2H TRIPLE Resonance of H-Bonds and Cysteinyl P-CH2 of the*. 1994. **85**(6): p. 1033-1041.
64. Canne, C., et al., *Probing magnetic properties of the reduced [2Fe-2S] cluster of the ferredoxin from Arthrospira platensis by 1H ENDOR spectroscopy.* Journal of biological inorganic chemistry 2000. **5**(4): p. 514-26.
65. Antonkine, M.L., et al., *Synthesis and characterization of de novo designed peptides modelling the binding sites of [4Fe-4S] clusters in photosystem I.* Biochimica et biophysica acta, 2009. **1787**(8): p. 995-1008.
66. Albertini, M., et al., *The proton iron-sulfur cluster environment of the [FeFe] -hydrogenase maturation protein HydF from Thermotoga neapolitana.* International Journal of Hydrogen Energy, 2014: p. 1-9.
67. Mouesca, J.-M., et al., *Spin densities and spin coupling in iron-sulfur clusters: a new analysis of hyperfine coupling constants.* Inorganic Chemistry, 1995. **34**(17): p. 4347-4359.
68. Mims, W., J. Davis, and J. Peisach, *The accessibility of type I Cu (II) centers in laccase, azurin, and stellacyanin to exchangeable hydrogen and ambient water.* Biophysical journal, 1984. **45**(4): p. 755-766.
69. Iwema, T., et al., *Structural Basis for Delivery of the Intact Fe2S2 Cluster by Monothiol Glutaredoxin.* Biochemistry, 2009. **48**(26): p. 6041-6043.
70. Johansson, C., et al., *Reversible sequestration of active site cysteines in a 2Fe-2S-bridged dimer provides a mechanism for glutaredoxin 2 regulation in human mitochondria.* Journal of Biological Chemistry, 2007. **282**(5): p. 3077-3082.
71. Johansson, C., et al., *The crystal structure of human GLRX5: iron-sulfur cluster co-ordination, tetrameric assembly and monomer activity.* Biochemical Journal, 2011. **433**: p. 303-311.
72. Li, H.R., et al., *The Yeast Iron Regulatory Proteins Grx3/4 and Fra2 Form Heterodimeric Complexes Containing a*

2Fe-2S Cluster with Cysteinyl and Histidyl Ligation. Biochemistry, 2009. **48**(40): p. 9569-9581.
73. Rouhier, N., et al., *Functional, structural, and spectroscopic characterization of a glutathione-ligated He-2S cluster in poplar glutaredoxin C1.* Proceedings of the National Academy of Sciences of the United States of America, 2007. **104**(18): p. 7379-7384.
74. Flint, D., et al., *The role and properties of the iron-sulfur cluster in Escherichia coli dihydroxy-acid dehydratase.* Journal of Biological Chemistry, 1993. **268**(20): p. 14732-14742.
75. Telser, J., et al., *17O electron nuclear double resonance characterization of substrate binding to the [4Fe-4S] 1+ cluster of reduced active aconitase.* Journal of Biological Chemistry, 1986. **261**(11): p. 4840-4846.
76. Werst, M.M., et al., *Oxygen-17, proton, and deuterium electron nuclear double resonance characterization of solvent, substrate, and inhibitor binding to the iron-sulfur [4Fe-4S]+ cluster of aconitase.* Biochemistry, 1990. **29**(46): p. 10526-10532.
77. Wan, T., et al., *Crystal structure of a multilayer packed major light-harvesting complex: implications for grana stacking in higher plants.* Molecular plant, 2014: p. ssu005.
78. Ke, B., *Photosynthesis: an overview.* Photosynthesis: Photobiochemistry and photobiophysics, 2003: p. 1-46.
79. Hall, D. and K. Rao, *Photosynthesis (6th edn).* Studies in Biology, Cambridge, Cambridge University Press, 1999.
80. Di Valentin, M., et al., *Identification of the sites of chlorophyll triplet quenching in relation to the structure of LHC-II from higher plants. Evidence from EPR spectroscopy.* The Journal of Physical Chemistry B, 2009. **113**(39): p. 13071-13078.
81. Di Valentin, M., et al., *Pulse ENDOR and density functional theory on the peridinin triplet state involved in the photo-protective mechanism in the peridinin-chlorophyll a-protein from Amphidinium carterae.* Biochimica et biophysica acta, 2008. **1777**(3): p. 295-307.

82. Di Valentin, M., et al., *Identification by time-resolved EPR of the peridinins directly involved in chlorophyll triplet quenching in the peridinin-chlorophyll a-protein from Amphidinium carterae.* Biochimica et biophysica acta, 2008. **1777**(2): p. 186-95.
83. Levanon, H. and K. Mobius, *Advanced EPR spectroscopy on electron transfer processes in photosynthesis and biomimetic model systems.* Annual review of biophysics and biomolecular structure, 1997. **26**(1): p. 495-540.
84. Hofmann, E., et al., *Structural basis of light harvesting by carotenoids: peridinin-chlorophyll-protein from Amphidinium carterae.* Science, 1996. **272**(5269): p. 1788-1791.
85. Sharples, F.P., et al., *Two distinct forms of the peridinin-chlorophyll a-protein from Amphidinium carterae.* Biochimica et Biophysica Acta (BBA)-Bioenergetics, 1996. **1276**(2): p. 117-123.
86. Schulte, T., et al., *X-ray structure of the high-salt form of the peridinin-chlorophyll a-protein from the dinoflagellate Amphidinium carterae: Modulation of the spectral properties of pigments by the protein environment.* Biochemistry, 2009. **48**(21): p. 4466-4475.
87. Bautista, J.A., et al., *Singlet and Triplet Energy Transfer in the Peridinin-Chlorophyll a-Protein from Amphidinium c arterae.* The Journal of Physical Chemistry A, 1999. **103**(14): p. 2267-2273.
88. Tomas, P., H.R. G., and F.H. A., *Spectroscopy of the peridinin -chlorophyll -a protein : Insight into light-harvesting strategy of marine algae*. Vol. 458. 2007, Kidlington, ROYAUME-UNI: Elsevier. 10.
89. Di Valentin, M., et al., *Triplet-triplet energy transfer in Peridinin-Chlorophyll a-protein reconstituted with Chl a and Chl d as revealed by optically detected magnetic resonance and pulse EPR: comparison with the native PCP complex from Amphidinium carterae.* Biochimica et biophysica acta, 2009. **1787**(3): p. 168-75.
90. Di Valentin, M., et al., *Conservation of Spin Polarization during Triplet-Triplet Energy Transfer in Reconstituted*

Peridinin-Chlorophyll-Protein Complexes. Journal of Physical Chemistry B, 2011. **115**(45): p. 13371-13380.
91. Niklas, J., et al., *Spin-density distribution of the carotenoid triplet state in the peridinin-chlorophyll-protein antenna. A Q-band pulse electron-nuclear double resonance and density functional theory study.* Journal of the American Chemical Society, 2007. **129**(50): p. 15442-15443.
92. Di Valentin, M., et al., *Evidence for water-mediated triplet-triplet energy transfer in the photoprotective site of the peridinin-chlorophyll a-protein.* Biochimica et biophysica acta, 2014. **1837**(1): p. 85-97.
93. Schulte, T., *Structural and Functional Investigations of the Soluble Light Harvesting Complex Peridinin-Chlorophyll a-Protein from Dinoflagellates*. 2010, Doctoral dissertation. Ruhr-University, Bochum.
94. Lendzian, F., et al., *Hyperfine structure of the photoexcited triplet state P680 in plant PS II reaction centres as determined by pulse ENDOR spectroscopy.* Biochimica et Biophysica Acta (BBA)-Bioenergetics, 2003. **1605**(1): p. 35-46.
95. Vrieze, J. and A. Hoff, *The orientation of the triplet axes with respect to the optical transition moments in (bacterio) chlorophylls.* Chemical physics letters, 1995. **237**(5): p. 493-501.
96. Bock, C.W., A. Kaufman, and J.P. Glusker, *Coordination of water to magnesium cations.* Inorganic Chemistry, 1994. **33**(3): p. 419-427.
97. Mikkelsen, K.V., et al., *Electron self-exchange in azurin: calculation of the superexchange electron tunneling rate.* Proceedings of the National Academy of Sciences, 1993. **90**(12): p. 5443-5445.
98. Miyashita, O., H. Axelrod, and J. Onuchic, *Different scenarios for inter-protein electron tunneling: the effect of water-mediated pathways.* Journal of biological physics, 2002. **28**(3): p. 383-394.
99. Lin, J., I.A. Balabin, and D.N. Beratan, *The nature of aqueous tunneling pathways between electron-transfer proteins.* Science, 2005. **310**(5752): p. 1311-1313.

100. Miyashita, O., M.Y. Okamura, and J.N. Onuchic, *Interprotein electron transfer from cytochrome c2 to photosynthetic reaction center: Tunneling across an aqueous interface.* Proceedings of the National Academy of Sciences of the United States of America, 2005. **102**(10): p. 3558-3563.
101. Chakrabarti, S., et al., *Experimental Evidence for Water Mediated Electron Transfer Through Bis-Amino Acid Donorb Bridgeb Acceptor Oligomers.* Journal of the American Chemical Society, 2009. **131**(6): p. 2044-2045.
102. Kendrew, J.C., et al., *A three-dimensional model of the myoglobin molecule obtained by x-ray analysis.* Nature, 1958. **181**(4610): p. 662-6.
103. Vandermeulen, G.W.M., et al., *Structure and dynamics of self-assembled poly(ethylene glycol) based coiled-coil Nano objects.* Chemphyschem, 2004. **5**(4): p. 488-494.
104. van Amsterdam, I.M.C., et al., *Measurement of a Cu-Cu distance of 26 a by a pulsed EPR method.* Angewandte Chemie-International Edition, 2003. **42**(1): p. 62-64.
105. Raitsimring, A.M., et al., *Gd3+ complexes as potential spin labels for high field pulsed EPR distance measurements.* Journal of the American Chemical Society, 2007. **129**(46): p. 14138-9.
106. Ezhevskaya, M., et al., *Distance determination between low-spin ferric haem and nitroxide spin label using DEER: the neuroglobin case.* Molecular Physics, 2013. **111**(18-19): p. 2855-2864.
107. Lovett, J.E., et al., *Structural information from orientationally selective DEER spectroscopy.* Physical Chemistry Chemical Physics, 2009. **11**(31): p. 6840-6848.
108. Jeschke, G., et al., *DeerAnalysis2006 - a Compehensive Software Package for Analyzing Pulsed ELDOR Data.* Ap, 2006. **498**: p. 473-498.
109. Ward, R., et al., *EPR distance measurements in deuterated proteins.* Journal of Magnetic Resonance, 2010. **207**(1): p. 164-167.
110. Milov, a.D., a.G. Maryasov, and Y.D. Tsvetkov, *Pulsed electron double resonance (PELDOR) and its applications*

in free-radicals research. Applied Magnetic Resonance, 1998. **15**(1): p. 107-143.
111. Krymov, V. and G.J. Gerfen, *Analysis of the tuning and operation of reflection resonator EPR spectrometers.* Journal of Magnetic Resonance, 2003. **162**(2): p. 466-478.
112. Jeschke, G., et al., *Sensitivity enhancement in pulse EPR distance measurements.* Journal of Magnetic Resonance, 2004. **169**(1): p. 1-12.
113. Richard, W., et al., *EPR distance measurements in deuterated proteins.* Journal of Magnetic Resonance, 2010. **207**(1): p. 164-167.
114. Narr, E., A. Godt, and G. Jeschke, *Selective measurements of a nitroxide-nitroxide separation of 5 nm and a nitroxide-copper separation of 2.5 nm in a terpyridine-based copper(II) complex by pulse EPR spectroscopy.* Angewandte Chemie (International ed. in English), 2002. **41**(20): p. 3907-10.
115. Pannier, M., et al., *Dead-time free measurement of dipole-dipole interactions between electron spins.* Journal of Magnetic Resonance, 2000. **142**(2): p. 331-340.
116. Gobbo, M., et al., *Synthesis and preliminary conformational analysis of TOAC spin-labeled analogues of the medium-length peptaibiotic tylopeptin B.* Journal of Peptide Science, 2012. **18**(1): p. 37-44.
117. Arikuma, Y., et al., *Electron Hopping over 100 angstrom Along an alpha Helix.* Angewandte Chemie-International Edition, 2010. **49**(10): p. 1800-1804.
118. Benedetti, E., et al., *Helical screw sense of peptide molecules: The pentapeptide system (Aib)(4)/L-Val L-(alpha Me)Val in the crystal state.* Biopolymers, 1998. **46**(7): p. 433-443.
119. Bucher, J. and D. Dolphin, *The Porphyrins.* by D. Dolphin, Academic Press, New York, NY, 1978. **1**(Part A).
120. Di Valentin, M., et al., *Porphyrin triplet state as a potential spin label for nanometer distance measurements by PELDOR spectroscopy.* Journal of the American Chemical Society, 2014. **136**(18): p. 6582-5.
121. Borovykh, I.V., et al., *Out-of-phase stimulated electron spin-echo appearing in the evolution of spin-correlated*

photosynthetic triplet-radical pairs. Journal of Physical Chemistry B, 2002. **106**(46): p. 12066-12071.
122. Potapov, A., et al., *Distance measurements in model bis-Gd(III) complexes with flexible "bridge". Emulation of biological molecules having flexible structure with Gd(III) labels attached.* Journal of Magnetic Resonance, 2010. **205**(1): p. 38-49.
123. Yulikov, M., et al., *Distance measurements in Au nanoparticles functionalized with nitroxide radicals and Gd3+-DTPA chelate complexes.* Physical Chemistry Chemical Physics, 2012. **14**(30): p. 10732-10746.
124. Yang, Z., M. Ji, and S. Saxena, *Practical Aspects of Copper Ion-Based Double Electron Electron Resonance Distance Measurements.* Applied Magnetic Resonance, 2010. **39**(4): p. 487-500.
125. Dal Farra, M., *A theoretical study of double electron-electron resonance (DEER) spectroscopy on radical-trilet state model systems.* M.Sc. dissertation, University of Padova, 2014.
126. Larsen, R.G. and D.J. Singel, *Double electron-electron resonance spin-echo modulation spectroscopy measurement of electron spin pair separations in orientationally disordered solids.* Journal of Chemical Physics, 1993. **98**(7): p. 5134-5146.
127. You, Z.Q. and C.P. Hsu, *Ab Inito Study on Triplet Excitation Energy Transfer in Photosynthetic Light-Harvesting Complexes.* Journal of Physical Chemistry A, 2011. **115**(16): p. 4092-4100.
128. Edmonds, D., et al., *The nuclear quadrupole resonance of 2D and 17O in Ice II.* Journal of Magnetic Resonance (1969), 1976. **23**(3): p. 505-514.
129. Stoll, S. and R.D. Britt, *General and efficient simulation of pulse EPR spectra.* Physical Chemistry Chemical Physics, 2009. **11**(31): p. 6614-6625.
130. El-Sayed, M.A., D.E. Tinti, and E.M. Yee, *Conservation of Spin Direction and Production of Spin Alignment in Triplet–Triplet Energy Transfer.* Journal of Chemical Physics, 1969. **51**: p. 5721-5723.

131. Imamura, T.O., O., Murai, H.; Obi, K., *Conservation of Spin Polarization during Triplet-Triplet Energy Transfer in Low-Temperature Matrices.* Journal of Physical Chemistry, 1984. **88**: p. 4028-4031.
132. Akiyama, K., et al., *Spin Polarization Conservation During Intramolecular Triplet-Triplet Energy-Transfer Studied by Time-Resolved EPR Spectroscopy.* Journal of the American Chemical Society, 1994. **116**(12): p. 5324-5327.
133. Di Valentin, M., et al., *Identification by time-resolved EPR of the peridinins directly involved in chlorophyll triplet quenching in the peridinin-chlorophyll a-protein from Amphidinium carterae.* Biochimica Et Biophysica Acta-Bioenergetics, 2008. **1777**(2): p. 186-195.
134. Kobori, Y., M. Fuki, and H. Murai, *Electron Spin Polarization Transfer to the Charge-Separated State from Locally Excited Triplet Configuration: Theory and Its Application to Characterization of Geometry and Electronic Coupling in the Electron Donor-Acceptor System.* Journal of Physical Chemistry B, 2010. **114**: p. 14621-14630.
135. Di Valentin, M., et al., *Conservation of Spin-Polarization during Triplet-Triplet Energy Transfer in Reconstituted Peridinin-Chlorophyll a-Proteins from Amphidinium carterae.* Journal of Physical Chemistry B, 2011. **115**(45): p. 13371-13380.
136. Di Valentin, M., et al., *Pulse ENDOR and density functional theory on the peridinin triplet state involved in the photo-protective mechanism in the peridinin-chlorophyll a-protein from Amphidinium carterae.* Biochimica Et Biophysica Acta-Bioenergetics, 2008. **1777**(3): p. 295-307.
137. Di Valentin, M., et al., *Identification of the Sites of Chlorophyll Triplet Quenching in Relation to the Structure of LHC-II from Higher Plants, Evidence from EPR Spectroscopy.* Journal of Physical Chemistry B, 2009. **113**: p. 13071-13078.
138. Vrieze, J. and A.J. Hoff, *The Orientation of the Triplet Axes with Respect to the Optical-Transition Moments in*

(Bacterio)Chlorophylls. Chemical Physics Letters, 1995. **237**(5-6): p. 493-501.
139. Lendzian, F., et al., *Hyperfine structure of the photoexcited triplet state (3)P680 in plant PSII reaction centres as detennined by pulse ENDOR spectroscopy.* Biochimica Et Biophysica Acta-Bioenergetics, 2003. **1605**(1-3): p. 35-46.
140. Frick, J., et al., *1st Detection of the (Nonphosphorescent) Triplet-State in Single-Crystals of Beta-Carotene.* Molecular Crystals and Liquid Crystals, 1990. **183**: p. 269-272.
141. Force, D.A., et al., *ESEEM studies of alcohol binding to the manganese cluster of the oxygen evolving complex of Photosystem II.* Journal of the American Chemical Society, 1998. **120**(51): p. 13321-13333.
142. Randall, D.W., et al., *ESE-ENDOR and ESEEM characterization of water and methanol ligation to a dinuclear Mn(III)Mn(IV) complex.* Journal of the American Chemical Society, 1997. **119**(19): p. 4481-4491.
143. Dapprich, S., et al., *A new ONIOM implementation in Gaussian98. Part I. The calculation of energies, gradients, vibrational frequencies and electric field derivatives.* Journal of Molecular Structure-Theochem, 1999. **461**: p. 1-21.
144. Vreven, T., et al., *Combining quantum mechanics methods with molecular mechanics methods in ONIOM.* Journal of Chemical Theory and Computation, 2006. **2**(3): p. 815-826.
145. Frisch, M.J., et al., *Gaussian 09*. 2009, Gaussian, Inc.: Wallingford, CT, USA.
146. Becke, A.D., *Density functional thermochemistry III. The role of exact exchange.* Journal of Chemical Physics, 1993. **98**(7): p. 5648-5652.
147. Lee, C.T., W.T. Yang, and R.G. Parr, *Development of the Colle-Salvetti correlation energy formula into a functional of the electron-density.* Physical Review B, 1988. **37**(2): p. 785-789.

APPENDIX A.3

PUBLISHED, ACCEPTED AND SUBMITTED PAPERS

APPENDIX A.4

LIST OF ABBREVIATIONS

Ac	Amphidinium carterae
Aib	α-aminoisobutyrric acid
Ala	Alanine
ATP	Adenosine triphosphate
B3LYP	Becke, three-parameter, Lee-Yang-Parr
Ca	Clostridium acetobutylicum
CW	Continuous Wave
DAF	Dalay After Flash
DEER	Double Electron Electron Resonance
Dd	Desulfovibrio desulfuricans
DFT	Density Functional Theory
DvMF	Desulfovibrio vulgaris Miazaki F
EM	Electromagnetic
EPR	Electron Paramagnetic Resonance
ESEEM	Electron Spin Echo Envelope Modulation
FID	Free Induction Decay
FSESE	Field-Swept Electron Spin Echo
FWHM	Full Width at Half Maximum
Hp	Heterocapsa pygmaea
HSPCP	High Salt PCP
HYSCORE	HYperfine Sublevel CORrElation spectroscopy

IC	Internal Conversion
ISC	InterSystem Crossing
LHC	Light Harvesting Complex
MFPCP	Main Form PCP
Mj	Methanocaldococcus jannaschii
$NADP^+$	Nicotinamide Adenine Dinucleotide Phosphate (oxidized form)
NADPH	Nicotinamide Adenine Dinucleotide Phosphate (reduced form)
NMR	Nuclear Magnetic Resonance
ONIOM	Our N-layered Integrated molecular Orbital and molecular Mechanics
PCP	Peridinin-Chlorophyll a-Protein
PELDOR	Pulse ELectron DOuble Resonance
S/N	Signal to Noise ratio
TOAC	4-amino-1-oxyl-2,2,6,6-tetramethyl-piperidine-4-carboxylic acid
Tn	Thermotoga neapolitana
TTET	Triplet-Triplet Energy Transfer
UFF	Universal Force Field